

# APPLICATION AND DEVELOPMENT OF MECHANORESPONSIVE POLYMER STRUCTURES

## DISSERTATION

zur Erlangung des akademischen Grades

Doctor rerum naturalium

(Dr. rer. nat.)

vorgelegt

dem Bereich Mathematik und Naturwissenschaften  
der Technischen Universität Dresden

von

**M.Sc. Jens W. Neubauer**

geboren am 31.08.1988 in Kronach

eingereicht am 28. Februar 2020

verteidigt am 29. Juni 2020

begutachtet durch Prof. Dr. Andreas Fery

Prof. Dr. Alexander Eychmüller

Die Dissertation wurde von Oktober 2014 bis August 2015 an der Universität Bayreuth und  
von September 2015 bis August 2018 am Leibniz-Institut für Polymerforschung Dresden e.V.  
angefertigt.







*If I have seen further it is by standing  
on ye sholders of Giants.*

Isaac Newton in a letter to Robert Hooke, 1675.

*Thunderbolts and Lightning  
Very, very frightening me.  
Galileo*

Queen: *Bohemian Rhapsody* on *A Night at the Opera*, 1975.



# Abstract

Mechanoresponsive systems respond to mechanical triggers by changes in a certain property. This thesis covers the work conducted with two mechanoresponsive systems that respond optically to mechanical triggers. These two systems are based on polymer structures, a polymer brush and a hydrogel network. Thus, the optical response mechanism allows observing acting forces as an approach to force sensing *in situ*.

In the first part, an existing mechanoresponsive system based on a polyelectrolyte brush labeled with a fluorescent dye is engaged in application. The charges of the polyelectrolyte are able to quench the fluorescence of the dye so that local compression or tension can be distinguished from the local fluorescence intensity. The mechanoresponsive polymer brush was applied as mechanosensitive surface coating to elucidate differences in the contact stress distributions of gecko-inspired adhesive micropillar structures. The determined results and the derived detachment mechanisms of the micropillar types were in qualitative accordance with predictions from theoretical approaches.

Overcoming the geometrical limitations of a planar surface coating, the second part aims at translating the mechanoresponse principle to a three-dimensional network and developing a mechanoresponsive hydrogel as a platform for force sensing. Conceptually, a homogeneous network allows to predict mechanical properties so that localized optical mechanoresponses could enable locating and quantifying acting forces. Based on network design principles from the Flory-Rehner theory, precursors with predefined size and architecture were utilized in hydrogel preparation, aiming for a homogeneous network. Further in this regard, the mixing volume was reduced by employing droplet microfluidics. As optical response mechanism, the hydrogel network precursors were labeled with two kinds of fluorophore, featuring distance-dependent emission from Förster Resonance Energy Transfer. The functionality of the optical response mechanism was demonstrated on global level by collapsing and controlled swelling of the network, and on a localized level by defined mechanical stress, applied with Atomic Force Microscopy. Owing to its adjustability, the hydrogel platform might be employed in various applications that require intrinsic force sensing of soft matter in future.





# Kurzfassung

Mechanoresponsive Systeme antworten auf mechanische Reize mit einer Eigenschaftsänderung. Diese Dissertation umfasst die Arbeiten mit zwei mechanoresponsiven Systemen, die optisch auf mechanische Reize antworten. Sie basieren auf polymeren Strukturen, einer Polymerbürste und einem Hydrogelnetzwerk. Ihr optischer Antwortmechanismus ermöglicht die Beobachtung wirkender Kräfte als ein Ansatz zur *in situ*-Kraftmessung.

Im ersten Teil wird ein existierendes, mechanoresponsives System zur Anwendung gebracht, das auf einer mit Fluoreszenzfarbstoff markierten Polyelektrolytbürste basiert. Die Ladungen des Polyelektrolyts können die Fluoreszenz des Farbstoffs unterdrücken, sodass lokale Kompression und Zugspannung über die Fluoreszenzintensität unterschieden werden können. Die mechanoresponsive Polymerbürste wurde als mechanosensitive Oberflächenbeschichtung angewandt, um Unterschiede in der Kontaktspannungsverteilung von Gecko-inspirierten adhäsiven Mikrotempelstrukturen aufzuklären. Die erarbeiteten Ergebnisse und daraus abgeleiteten Ablösemechanismen der Mikrotempeltypen deckten sich qualitativ mit Vorhersagen aus theoretischen Ansätzen.

Aufgrund geometrischer Einschränkungen einer planaren Oberflächenbeschichtung zielt der zweite Teil darauf ab, dieses mechanoresponsive Prinzip in ein dreidimensionales Netzwerk zu überführen und ein mechanoresponsives Hydrogelnetzwerk als Plattform zur Kraftmessung zu entwickeln. Konzeptionell besitzt ein homogenes Netzwerk vorhersagbare mechanische Eigenschaften, sodass lokale optische Antworten auf mechanische Kräfte ermöglichen könnten, die wirkenden Kräfte zu lokalisieren und quantifizieren. Basierend auf einer Gestaltung nach der Flory-Rehner-Theorie wurden Präkursoren mit vordefinierter Größe und Architektur für die Hydrogelherstellung eingesetzt, um auf ein homogenes Netzwerk abzielen. Zu diesem Zweck wurde das Mischungsvolumen durch Tropfenmikrofluidik reduziert.

Für den optischen Antwortmechanismus wurden die Hydrogelnetzwerk-Präkursoren mit zwei verschiedenen Fluorophoren markiert, die sich durch abstandsabhängige Emission über Förster-Resonanzenergietransfer auszeichnen. Die Funktionalität des optischen Antwortmechanismus wurde auf globaler Ebene durch Kollabieren und kontrolliertes Quellen des Netzwerks, dann auf lokalisierter Ebene durch definierte mechanische Belastung mit Rasterkraftmikroskopie gezeigt. Durch ihre Anpassbarkeit könnte die Hydrogelplattform zukünftig verschiedenste Anwendungen im Bereich intrinsischer Kraftmessung weicher Materie bedienen.



# Contents

Abstract.....	v
Kurzfassung .....	vii
Contents .....	ix
List of Publications .....	xi
List of Abbreviations .....	xiii
I. Introduction.....	1
II. Synopsis.....	7
III. Status of the Field .....	15
III.1. Material Design – Combining Polymer Physics and Polymer Chemistry .....	16
III.1.1. Fundamentals of Polymer Physics .....	16
III.1.2. Polymer Brushes – Functional and Responsive Surface Coatings .....	19
III.1.3. Polymer Networks – Three-dimensional Functional Polymer Structures .....	25
III.2. Atomic Force Microscopy – Applying Forces and Investigating Mechanics .....	35
III.2.1. Principles of Atomic Force Microscopy .....	36
III.2.2. Force Measurements with Atomic Force Microscopy .....	37
III.2.3. Colloidal Probe Technique and Continuum Contact Models .....	41
III.3. Fluorescence Effects – Optical Responses to Changes in Environment .....	46
III.3.1. Fluorescence .....	46
III.3.2. Förster Resonance Energy Transfer .....	49
III.3.3. Origins and Developments of Confocal Microscopy .....	53
III.4. Mechanoresponsive Materials .....	58
III.4.1. Peptide- and DNA-based Single Molecule Sensors .....	58
III.4.2. Mechanochromic Materials .....	61
III.4.3. Systemic and Structural Mechanoresponse .....	63
IV. Monitoring the Contact Stress Distribution of Gecko-Inspired Adhesives Using Mechanosensitive Surface Coatings .....	69
IV.1. Introduction to Bioinspired Adhesive Microstructures .....	73
IV.2. Resolving Contact Stresses with Mechanoresponsive Polymer Brushes .....	75
IV.3. Combination of Microcontact Printing and Confocal Microscopy .....	76
IV.4. Determination of Contact Stress Distribution for Adhesive Microstructures .....	80
IV.5. Conclusions .....	88
IV.6. Experimental Section .....	89

V.	Mechanoresponsive Hydrogel Particles as a Platform for Three-Dimensional Force Sensing .....	93
V.1.	Concept for the Preparation and Characterization of Mechanoresponsive Polymer Network Structures .....	97
V.2.	Droplet Microfluidics for the Preparation of Hydrogel Particles .....	99
V.3.	FRET Response to Global Network Deformations from Swelling in Humidity .....	109
V.4.	Mechanical Characterization of the Hydrogel Network Structure .....	117
V.5.	FRET Response to Mechanical Deformations of the Hydrogel Network ....	120
V.6.	Conclusions .....	130
V.7.	Experimental Details .....	132
VI.	Outlook and Perspectives .....	137
VI.1.	Adaption of the Hydrogel Platform to an Application in Force Sensing ....	139
VI.2.	Approaches for Quantifying Stresses Acting in the Network .....	141
VI.3.	FRET for Sensing in Polymer Brushes .....	142
	Bibliography .....	145
	Danksagung .....	xv
	Versicherung und Erklärung .....	xvii

# List of Publications

1. “*Mechanoresponsive Hydrogel Particles as a Platform for Three-Dimensional Force Sensing*”  
**Jens W. Neubauer**, Nicolas Hauck, Max J. Männel, Maximilian Seuss, Andreas Fery,\* Julian Thiele\*  
*ACS Appl. Mater. Interfaces* **2019**, 11 (29), 26307–26313.
2. “*One-Step Photostructuring of Multiple Hydrogel Arrays for Compartmentalized Enzyme Reactions in Microfluidic Devices*”  
Franziska Obst, David Simon, Philipp J. Mehner, **Jens W. Neubauer**, Anthony Beck, Oleksandr Stroyuk, Andreas Richter, Brigitte Voit,\* Dietmar Appelhans\*  
*Reaction Chemistry & Engineering* **2019**, 4 (12), 2141–2155.
3. “*Systematic Evaluation of Different Types of Graphene Oxide in Respect to Variations in their In-Plane Modulus*”  
Patrick Feicht, Renée Siegel, Herbert Thurn, **Jens W. Neubauer**, Maximilian Seuss, Tamás Szabó, Alexandr V. Talyzin, Christian E. Halbig, Siegfried Eigler, Daniel A. Kunz, Andreas Fery, Georg Papastavrou, Jürgen Senker, Josef Breu\*  
*Carbon* **2017**, 114, 700–705.
4. “*Mechanically Defined Microgels by Droplet Microfluidics*”  
Thomas Heida,† **Jens W. Neubauer**,† Maximilian Seuss,† Nicolas Hauck,† Julian Thiele,\* Andreas Fery\*  
*Macromolecular Chemistry and Physics* **2017**, 218 (2), 1600418.
5. “*Monitoring the Contact Stress Distribution of Gecko-Inspired Adhesives Using Mechano-Sensitive Surface Coatings*”  
**Jens W. Neubauer**, Longjian Xue, Johann Erath, Dirk-M. Drotlef, Aránzazu del Campo,\* Andreas Fery\*  
*ACS Applied Materials & Interfaces* **2016**, 8 (28), 17870–17877.

\*Corresponding authors

† Authors contributed equally

6. “Controlled Exfoliation of Layered Silicate Heterostructures into Bilayers and their Conversion into Giant Janus Platelets”

Matthias Stöter, Sebastian Gödrich, Patrick Feicht, Sabine Rosenfeldt, Herbert Thurn, **Jens W. Neubauer**, Maximilian Seuss, Peter Lindner, Hussein Kalo, Michael Möller, Andreas Fery, Stephan Förster, Georg Papastavrou,\* Josef Breu\*  
*Angewandte Chemie* **2016**, 128 (26), 7524–7528.

# List of Abbreviations

4-arm PEG-Mal	poly(ethylene glycol) four-arm starpolymer with maleimide termini
4-arm PEG-SH	poly(ethylene glycol) four-arm starpolymer with thiol termini
A/D intensity ratio	ratio of acceptor intensity to donor intensity
AdG model	model of Alexander and de Gennes
AEMA	2-aminoethyl methacrylate hydrochloride
AFM	atomic force microscope/microscopy
AU	Airy unit
CCD	charge-coupled device
CLSM	confocal laser scanning microscope/microscopy
CP	colloidal probe
DNA	deoxyribonucleic acid
DIN	German industry standard ( <i>Deutsche Industrie Norm</i> )
DMSO	dimethyl sulfoxide
DMT model	model of Derjaguin, Müller and Toporov
ECM	extracellular matrix
EN	European standard
FEM	finite element modeling
FITC	fluorescein isothiocyanate
FLIM	fluorescence lifetime imaging microscopy
FRET	Förster resonance energy transfer
hMSC	human mesenchymal stem cell
InvOLS	inverted optical lever sensitivity
ISO	international standard (International Organization for Standardization)
JKR model	model of Johnson, Kendall and Roberts
METAC	[2-(methacryloyloxy)ethyl]trimethylammonium chloride
MF	microfluidic(s)
MPTMS	mercaptopropyltrimethoxysilane
MW	molecular weight
MWC model	model of Milner, Witten and Cates
PAAm	polyacrylamide
PALM	photoactivated localization microscopy
PBS	phosphate buffered saline
PDMS	polydimethylsiloxane
PEG	poly(ethylene glycol)
PEG-diMal	poly(ethylene glycol) with maleimide termini
PFPE	perfluoropolyether
NIPAAm	poly(N-isopropylacrylamide)
RH	relative humidity
SCP	soft colloidal probe
SEM	scanning electron microscopy
STED	stimulated emission depletion
TRITC	trirhodamine isothiocyanate
UV	ultraviolet radiation
wt. %	weight concentration





# I. Introduction

---

Sensing forces is among human's senses. Omnipresent but most of the time rather unperceived, the vestibular system in the inner ear is crucial for orienting and balancing human's motion. Rather, it might be perceived when people suffer from motion sickness which even occurs among the majority of astronauts, reporting drowsiness and nausea in a state of zero gravity.<sup>1</sup> Not uncommonly, such effective sensing mechanisms are mimicked to find their way into a technical application. From a technical perspective, the vestibular system is sensing acceleration so that motional forces can be deduced. A similar concept is realized technically in the electronic stability control of cars,<sup>2</sup> for example.

Whereas the vestibular system comprises a comparably sophisticated sensing mechanism, force sensing systems can be as simple as a balance scale (Figure I-1). It is used to determine the weight force of objects on one side by balancing the other side with known weights. The use of the balance scale dates back to the ancient Egyptians.<sup>3</sup> Much later, the pioneering work for laying the foundation of classical mechanics was achieved by Sir Isaac Newton in the 17<sup>th</sup> century. As an honor, *Newton* was chosen as eponym for the unit of force in 1948.<sup>4</sup>



**Figure I-1.** Historic balance scale for coins, exhibited in the Cabinet of Astronomy and Physics in Kassel.

Contemporary with Newton, Robert Hooke also researched in classical mechanics. Named after him, the Hookean spring has a linear relation between an acting force and its resulting deflection. Knowing this relation, Hooke's law allows to determine forces from the spring deflection, making it an ideal force sensor. However, the forces sensed with a Hookean spring are equally exerted on the measured object according to Newton's laws. In this perspective, such extrinsic force sensing bears the risk of altering or damaging the measured object owing to the additional mechanical interactions exerted during the measurement.

---

In contrast, intrinsic sensing systems are included in the force-acted body, allowing to sense forces without additional extrinsic forces. Besides the vestibular system, another example of an intrinsic force sensor is human skin. Its sensing of mechanical contact by feeling and during handling objects goes far beyond analytical force sensing. When lifting an object by hand, one is able to adjust grip forces strong enough to hold the object firmly, and soft enough to not damage the object, or the skin itself. As for the vestibular system, it is desirable to mimic the biological sensing system for technology applications, e.g. in robotics to monitor the mechanics during handling *in situ* for comparable tactility as human handling.

Also on a microscopic scale, processes are governed by forces so that accordingly sensing concepts have been adapted for application on the microscale. Atomic force microscopy (AFM) has been established within the last three decades as a microscopic force sensing method.<sup>6</sup> It enables to determine the mechanical properties of samples with micro- and nanometer resolution, but is based on a Hookean spring so that extrinsic forces are exerted on the samples during measurements.

An example for microscale processes governed by mechanics is the lineage specification of human stem cells.<sup>7</sup> It has been reported that the stem cell specification is affected by the elasticity of their surrounding matrix. With AFM, the mechanics of the cells and their matrix could be determined. At the same time, such additional extrinsic forces might influence the cells in a process governed by mechanics and, thus, actively alter the outcome of the experiments. For this reason, intrinsic force sensing is beneficial for determining the direct interactions between the cells and their matrix, and therefore, it has become a central challenge in the emerging field of mechanobiology.

Approaches for intrinsic sensing in cellular environment often utilize molecular components of the cell or molecules of similar chemistry for good biocompatibility. Further, these components are characterized in regard to their mechanics, and adapted to report mechanical deformation by an optical response. For example, such an approach was used for investigating the mechanical function of a molecular component in the focal adhesion of cells.<sup>8</sup> Integrating an optical response mechanism into the cellular functionality can preserve from influencing mechanical processes extrinsically, while allowing for observing them externally.

In contrast to such targeted investigations, more universal approaches could avoid an alteration of the cells. Aiming for the extracellular matrix, a material with defined

mechanics could be designed with integrated optical functionalities to report and read out deformations. Embedding cells in this material, their mechanical interactions with the matrix could be investigated not only for single cells, but also in cell clusters.

On the basis of polymer brushes, the foundation for such a universal force-sensing material has been achieved: It is a mechanoresponsive surface-coating with the ability to report acting stresses optically.<sup>9</sup> This material was demonstrated to reach the sensing benchmarks of human skin.

Following up on this basis, the aim of this work is the application of the mechanoresponsive surface coating to elucidate the contact mechanics of adhesive structures, and the development of a mechanoresponsive polymer network structure by transferring the concept and experiences with the two-dimensional surface coating to a three-dimensional structure.

In the first part of the thesis, the mechanoresponsive polyelectrolyte brush surface coating is utilized in a setup to determine the contact stress distributions of adhesive microstructures. In the setup, the contact stress distributions of the adhesive microstructures are mapped with micrometer scale resolution to resolve differences in the contact mechanics of differing geometries. Being limited to planar geometry in force sensing, the mechanoresponse concept is transferred to a three-dimensional mechanosensing platform in the second part of the thesis. Therefore, it first focuses on the conception and preparational realization of a three-dimensional polymer network with defined mechanics and integrated optical response functionalities as a universal, adaptable material platform. Moreover, by proving the optical response of the conceptualized material, its sensing capabilities are benchmarked and a calibration method for an application of the material is outlined.

In conclusion, a mechanoresponsive surface-coating is brought to its first application and a mechanoresponsive polymer network platform is developed, opening further force-sensing applications.

---

## II. Synopsis

---

**Outline.** The work presented in this thesis has the common topic of force sensing by utilizing polymeric mechanoresponsive systems. It covers a broad range from basic, fundamental and theoretical aspects, over material development and rational design to the application of such materials for elucidating fundamentals of a different field. The thesis is structured accordingly. After the introduction of structural and mechanical properties, and optically detectable effects in the context of mechanoresponsive concepts (Chapter III), the application of an established polymeric mechanosensor is demonstrated (Chapter IV) to showcase the possibilities, but also current limitations. Based on this, the design and development of a new kind of polymeric mechanosensor is tackled (Chapter V).

**Chapter III** covers a general overview of the materials and techniques used. The chapter outline follows Hooke's law. The spring constant in Hooke's law is a *material property*. In the first part, the material properties of the mechanoresponsive polymer structures are discussed in terms of their molecular structure and the basics of the underlying polymer physics of single polymer chains, polymer brushes, and polymer networks. Moreover, preparation aspects of polymer brushes and polymer networks are pointed out to gain a holistic view on the core pieces of this thesis. To determine *forces* with these mechanoresponsive structures, their mechanical properties need to be investigated. With Atomic Force Microscopy (AFM), a well suited technique for mechanical characterization on the microscale is introduced. While on the one hand force measurements are conducted with AFM, on the other hand the results have to be interpreted and evaluated to shed light onto the mechanical properties. On this account, an insight to the continuum contact mechanic models established in the field is given. Eventually, the *deformation* is correlated with the mechanoresponse. The presented polymer structures respond by an optical signal, mostly based on fluorescence effects. The principles of fluorescence and associated effects (e.g. Förster Resonance Energy Transfer, FRET), as well as microscopy techniques used for the localization of such, are discussed in the third part of the chapter. In the last section of the chapter, the components are joined again by discussing various examples for mechanoresponsive concepts. Among them, the mechanoresponsive polyelectrolyte brush applied in the upcoming chapter is introduced.



**Chapter IV** demonstrates the abilities of mechanoresponsive polymer structures by elucidating contact mechanics of bio-inspired adhesive microstructures. Following design principles identified from geckos and insects, bio-inspired microstructures were developed mostly in the form of micropillar structures with varying contact geometry. Here, most pronounced differences in adhesion performance were found for two contact geometries, cylindrical flat punches and T-shaped pillars, i.e. cylindrical pillars with an annular overhang (Figure II-1). In literature, differing detachment mechanisms were postulated for these geometries from analytical contact mechanic models.

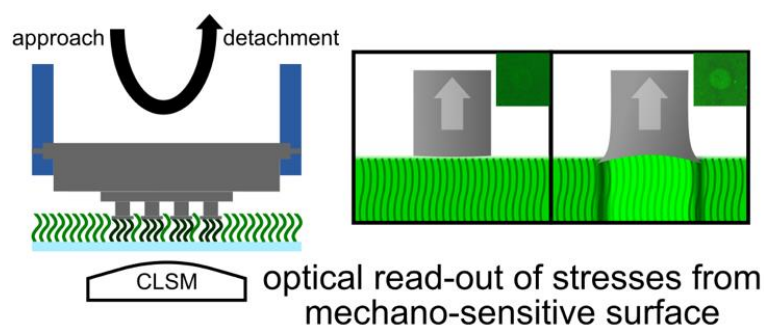


**Figure II-1.** Graphical presentation of the content in Chapter IV. Reprinted with permission from Neubauer et al.<sup>10</sup> Copyright American Chemical Society 2016.

By the application of a mechanoresponsive polyelectrolyte brush, the underlying contact mechanics could be elucidated and proven. The polyelectrolyte brush is labeled with a fluorophore which can be quenched by the charges of the polyelectrolyte. Therefore, its fluorescence critically depends on the conformation of the polymer brush structure. Previous work has shown that the mechanical compression decreases the fluorescence intensity by increased quenching, whereas tensile stress on the polymer brushes increases fluorescence intensity vice versa. Therefore, it is one *property* of this mechanoresponsive polymer brush to signal its local *deformation* via fluorescence intensity to distinguish compressive and tensile *forces*. Reading out the local fluorescence with the optical resolution of Confocal Laser Scanning Microscopy (CLSM, Section III.3.3) rendered this polymer structure a mechanosensor for mapping compressive and tensile stress.

For the first time, this allowed to map the stress distributions under flat punch and T-shaped micropillars. In the scope of this work, the preparation procedure for these bio-inspired micropillar structures was adapted to mount them to a micro-contact printing device for a controlled contact formation to and retraction from the mechanosensing polyelectrolyte brush. In a combined setup with CLSM, the local stresses during contact and detachment

---

could be observed *in situ*. Investigating the detachment of flat punch and T-shaped micropillars, two differing detachment mechanisms could be derived in conformity with the postulations of others.

During the detachment of T-shaped micropillars, tensile stress concentrated to the center of the contact area prior to pull-off. Proving other's predictions from analytical models, the according detachment mechanism describes crack nucleation in the center followed by crack propagation to the edges, and adhesion failure. In contrast, tensile stress is predicted to concentrate to the edges of flat punches causing crack nucleation and quick propagation toward the center. In full accordance, the detachment from the mechanosensing polyelectrolyte brush was quick, and tensile stresses could not be resolved.

Demonstrating the abilities of polymeric mechanosensing surface coatings, this application as well reveals the limitation of sensing in planar geometries only. Therefore, the sensing mechanism is translated to a three-dimensional structure in the next chapter.

**Chapter V** comprises the development of a three-dimensional polymeric mechanosensing platform to overcome the geometrical limitations of the mechanoresponsive polyelectrolyte brush. To advance the established mechanoresponse principle from polymer brushes to polymer networks, a hydrogel network was designed. Its blueprint was sketched following the physical fundamentals of networks to reach homogeneity in architecture, and in mechanical properties consequently. For the response mechanism, the hydrogel network was labeled with fluorophore pairs to signal local network deformation as optical signal (FRET, Section III.3.2). As outlined by the example of Hooke's law, *forces* acting locally in the network are to be determined from the *mechanical properties* of the network and the local *deformation* signaled optically from the characteristic FRET shift (Figure II-2). Being able to control mechanical homogeneity and sense local deformations, the hydrogel network would be able to allow mechanosensing in three-dimensional environments. Therefore, the development was divided into two parts, the preparation of hydrogel networks with homogeneous *mechanical properties* and the characterization of the network response to *deformation* at defined *forces*.

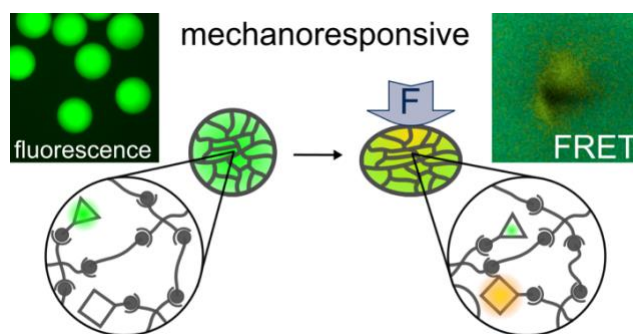


**Figure II-2.** Graphical presentation of the mechanoresponse concept discussed in Chapter V. Reprinted with permission from Neubauer et al.<sup>11</sup> Copyright American Chemical Society 2019.

For homogeneity in the network structure, the hydrogel was prepared from precursor molecules with predefined size in a polymer-analogous crosslinking reaction. The efficiency of the crosslinking reaction usually comes with the challenge of high reactivity. Hence, while on the one hand high reactivity promotes homogeneity in network formation, quick crosslinking can hamper sufficient mixing in a way that unreacted precursors are not able to crosslink. This aspect, on the other hand, can simultaneously induce network heterogeneities. Utilizing droplet microfluidics, the reaction volume of the hydrogel precursors was reduced to microscale for efficient mixing (Section III.1.3). As reactivity and mixing both influence the hydrogel formation, advances in the hydrogel preparation went hand in hand with the refinement of the microfluidic channel structure. In exploring the parameter space, not only a more detailed understanding of the network formation could be gained, but also hydrogel particles could be yielded.

Besides gaining control over network formation, an essential feature was the labeling with fluorophores to localize deformations by a FRET shift. To incorporate this parameter in the development process, Atomic Force Microscopy (AFM, Section III.2) was utilized in a combined setup with CLSM (Section III.3.3) to monitor the fluorescence response of the labeled network to deformation. Both global and local network deformations were investigated. A global collapse of the network by drying lead to the expected optical response by FRET. In controlled humidity, the network globally expanded successively, responding by reverting the optical response. For localized deformations with defined forces, the Colloidal Probe (CP) technique in AFM was used. Using a spherical AFM probe to deform the hydrogel particles, established contact mechanics models were applied (Section III.2.3) to determine elastic properties of the hydrogel particles. Monitoring the fluorescence response during indentation of the CP, the conceptualized fluorescence response could be localized to regions deformed under the CP load. The contact mechanics

---

models allowed to estimate the stress resolution of the mechanoresponsive hydrogel particles to the lower kPa range. Indenting an AFM tip, the spatial resolution of the mechanoresponse could be determined to the micrometer scale.

Having established preparation and characterization procedures for mechanoresponsive hydrogel networks, the large parameter space opens the possibilities to further adjust the sensitivity and resolution of the hydrogel for force sensing. This hydrogel platform could pave a way for three-dimensional polymeric force sensors.

**Chapter VI** ultimately offers perspectives on how the mechanoresponsive hydrogel particle platform could be further developed for application, in regard to customized sensitivity and mechanical properties. Moreover, certain aspects influencing the response mechanism could benefit from further elucidation, for example, modeling the network deformation and stresses acting inside. Therefore, further research projects might ensue from this thesis. Furthermore, a concept is sketched briefly which combines both mechanoresponsive materials utilized in this thesis.

**Personal contributions.** As the results from the Chapters IV and V, and an overview to recent trends in mechanically defined microgels by droplet microfluidics (cf. Section III.1.3) were published in journal articles as a collaboration of multiple scientists, I would like to highlight and elaborate my contributions to the presented and published work.

Chapter IV is published in ACS Applied Materials & Interfaces under the title “**Monitoring the Contact Stress Distribution of Gecko-Inspired Adhesives Using Mechano-Sensitive Surface Coatings**” authored by Jens W. Neubauer, Longjian Xue, Johann Erath, Dirk-M. Drotlef, Aránzazu del Campo, and Andreas Fery.

**JWN** performed all of the experiments and evaluation, and prepared the mechanoresponsive polyelectrolyte brushes and the adhesive microstructures for the experiments. Further, **JWN** wrote the manuscript with close support of all other authors. **LX** and **JWN** collaborated in adapting the microstructure preparation for the final experiment design. **JE** and **DMD** performed preliminary experiments and developed the first experiment design forming the basis for the project. **AdC** and **AF** supervised the project and guided it with in-depth discussions of the results.

Results from Chapter V are published in ACS Applied Materials & Interfaces under the title “**Mechanoresponsive Hydrogel Particles as a Platform for Three-Dimensional Force Sensing**” authored by Jens W. Neubauer, Nicolas Hauck, Max J. Männel, Maximilian Seuss, Andreas Fery, and Julian Thiele.

**JWN** performed most of the experiments, including hydrogel particle preparation, characterization with AFM and optical microscopy, and determination and evaluation of the network response. **JWN** mainly wrote the manuscript with close support of JT and AF. NH supported in the microfluidic preparation and prepared some hydrogel particle batches. MJM drafted and refined the design of the microfluidics structure, and supported in the preparation of the microfluidic structures. MS performed and evaluated humidity swelling experiments in the revision period. AF and JT supervised the project, guided it with many in-depth discussions of the results and gave valuable feedback to improve and revise the manuscript.

A trend article covering a similar topic as discussed in Section III.1.3 was published in Macromolecular Chemistry and Physics under the title “**Mechanically Defined Microgels by Droplet Microfluidics**” authored by Thomas Heida, Jens W. Neubauer, Maximilian Seuss, Nicolas Hauck, Julian Thiele, and Andreas Fery.

TH, **JWN**, MS, and NH wrote the manuscript collectively. JT and AF supervised the project and closely supported the writing process with valuable remarks and discussions.

---

# III. Status of the Field

Parts of this chapter were adapted from the manuscript of the trend article

“Mechanically Defined Microgels by Droplet Microfluidics”

by Thomas Heida, Jens W. Neubauer, Maximilian Seuss, Nicolas Hauck, Julian Thiele, and Andreas Fery. *Macromol. Chem. Phys.* **2017**, *218*, 1600418.

It is reprinted with permission, whereas the copyright remains with WILEY 2016. The text and the published figures were adapted to be integrated into this thesis.

---

## III.1. Material Design – Combining Polymer Physics and Polymer Chemistry

The design of mechanoresponsive polymer structures is based on the understanding of the components it is constructed from. This chapter serves as an overview of the polymer physics from single chains to polymer brushes and networks, and the preparation methods to yield defined polymer brushes and hydrogel networks.

### III.1.1. Fundamentals of Polymer Physics

Polymers are chain molecules built up from monomers. Over decades, various models have been derived to describe the physics of polymers. They are widely explained in literature.<sup>12,13</sup>

A simple description for a single chain is a random walk. This means, each step is independent and can head in any direction, but with a constant step length. The step length  $l$  is a matter of definition. It may be the length of a monomer. Hence, the number of steps  $N$  equals the degree of polymerization. In the ideal chain model, only the step length is fixed, the direction after each step does not have constrictions (freely jointed segments). One way to describe the dimension of a chain is the end-to-end distance (Figure III-1A). By treating each step in the random walk as a vector between two junction points, the end-to-end distance of the ideal chain  $R_0$  can be calculated (equation (1)).<sup>12</sup>

$$R_0 = l \cdot N^{\frac{1}{2}} \quad (1)$$

Besides a defined monomer length and freely jointed segments in the ideal chain model, further constrictions can be considered, such as the bond angle between segments and preferred conformations depending on the monomers. Whereas the ideal chain can serve as a scaling model to describe polymers in so-called  $\theta$ -conditions, e.g. in bulk, excluded volume interactions of the chains are neglected.<sup>12</sup>



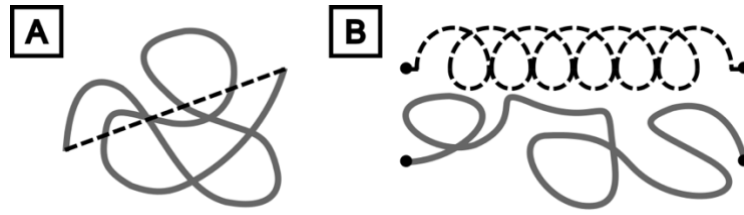


**Figure III-1.** (A) Coiled polymer chain (gray) with indicated end-to-end distance (dashed black line). (B) Scheme to depict the concept of a polymer entropic spring. Increasing the end-to-end distance of the chain (gray), entropic forces are arising in opposite direction, comparable to elastic forces of a spring (dashed black line).

Mentioned excluded volume interactions arise from the finite volume of the segments and their solvation. In good solvents, polymers are swollen so that their excluded volume needs to be taken into account. If so, the end-to-end distance is increased with identical  $N$  and  $l$ , being called the Flory radius  $R_F$  (equation (2)).<sup>13</sup>

$$R_F = l \cdot N^{\frac{3}{5}} \quad (2)$$

Commonly, the radius of gyration of a chain is used to depict its dimensions. Rotating around an axis at the radius of gyration, the moment of inertia is equivalent for the chain and a single point of the same mass. As excluded volume interactions expand the chain, the radius of gyration scales accordingly (equation (3)).<sup>13</sup>

$$R_g \propto N^\gamma \quad \text{with } \gamma = \begin{cases} \frac{1}{2} & \text{for } \theta\text{-conditions} \\ \frac{3}{5} & \text{in good solvents} \end{cases} \quad (3)$$

On the level of a single chain segment, its excluded volume is given by  $\nu_{\text{excl.}} \cdot l^3$  so that the geometrical volume is factored by the dimensionless excluded volume parameter  $\nu_{\text{excl.}}$  (equation (4)).<sup>13</sup>

$$\nu_{\text{excl.}} = 1 - 2\chi \quad (4)$$

The Flory-Huggins parameter  $\chi$  is a measure for interactions between the segments and the solvent. In  $\theta$ -conditions,  $\chi = 0.5$  so that the excluded volume is zero. In good solvents,

---

solvent interactions lead to swelling of the chain ( $0 < \chi < 0.5$ ). Poor solvents lead to collapse of the polymer ( $\chi > 0.5$ ) so that attractive interactions between segments are preferred.<sup>12,13</sup> Solvent interactions are able to stretch polymer chains. Often, the stretching by solvation is counteracted by chain elasticity. The Rouse model expresses this elasticity, depicting polymer chains as entropic springs (Figure III-1B). When an individual chain is stretched, the number of conformational states is reduced with increasing stretching. Accordingly, the decreased entropy is stored as elastic energy. The relation for the force  $f_{\text{chain}}$  needed to stretch a chain or chain segment is a function of the end-to-end distance  $\Delta r$  similar to Hooke's law (equation (5)).<sup>12</sup>

$$\begin{aligned} f_{\text{chain}} &= b \Delta r \\ \text{with } b &= \frac{3 k_B T}{\langle \Delta r^2 \rangle} \end{aligned} \quad (5)$$

The spring constant  $b$  increases with the thermal energy  $k_B T$  as entropy increases with temperature. Further,  $b$  is reciprocally dependent on the mean squared end-to-end distance  $\langle \Delta r^2 \rangle$ . The shorter the chain, the lesser the conformational states which are further restricted upon stretching.

Without explicitly being given in the expression, the solvation conditions of the polymer can also affect  $b$ . As shown above,  $\langle \Delta r^2 \rangle$  changes with solvent quality. A chain collapsed in a poor solvent has a shorter mean squared end-to-end distance than in a good solvent. Thus,  $b$  is expected to be comparably higher in a poor solvent.

As polymer chains are the basic components of the polymer structures introduced in the following, these very fundamental considerations on individual chains are the basis of models for polymer brushes and networks.

### III.1.2. Polymer Brushes – Functional and Responsive Surface Coatings

Polymer brushes are structures in which the polymer chains are tethered to a surface at one end. This boundary condition restricts their conformation and leads to directed interactions, differing from those of bulk polymers.

The formation of a brush structure is determined mainly by the grafting density of the chains and the solvent quality  $\chi$ . In a poor solvent, the polymer is collapsed on the surface. If the distance  $s$  between the chains is sufficiently large, the polymer tends to coil resulting in a certain radius of gyration. If  $s$  is smaller than the radius of gyration, interactions between neighboring chains constrain the conformation of the tethered chains. Consequently, the preferable conformation is oriented away from the surface (Figure III-2). A "true polymer brush" is formed if the brush thickness  $L$  is much greater than the polymer chain's radius of gyration.<sup>14,15</sup>

In general, two approaches are used for the generation of polymer brushes. Either the polymer is synthesized beforehand for *grafting to* a surface, or polymerized *grafting from* a surface.<sup>15</sup> By *grafting to* a surface, it might be challenging to generate a true brush because the polymer might be attached in coiled conformation (mushroom regime). However, before providing a deeper insight into the preparation methods and the functionality of responsive brush structures, the interactions controlling brush conformations are elucidated in the following.

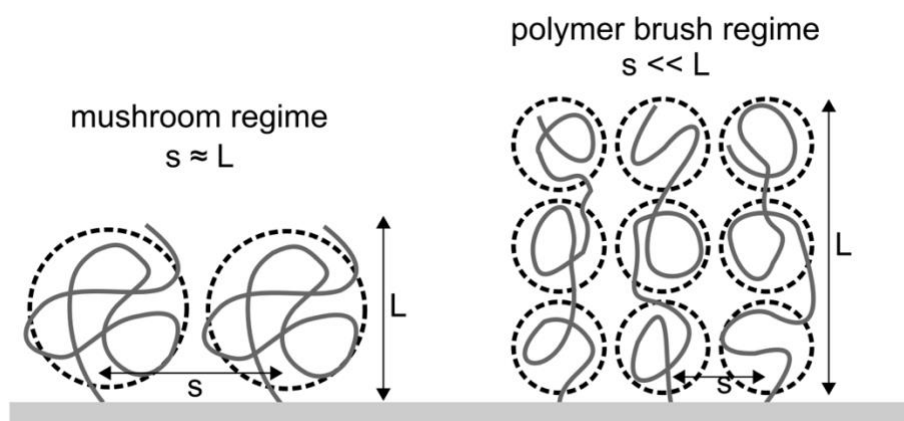


**Figure III-2.** Schematic depiction of the mushroom regime (left) and the polymer brush regime (right), related to grafting distance  $s$  and brush thickness  $L$ . In the mushroom regime, the polymer is coiled at the surface, whereas the polymer brush is depicted subdivided into "blobs".

---

### *Models of Polymer Brushes*

The polymer brush conformation is a result of the counteraction of excluded volume interactions and the entropic restoring forces of the chains. This was first described by Alexander<sup>16</sup> and de Gennes<sup>17</sup> (AdG). With increasing grafting density  $\sigma_g = s^{-2}$  (chains per unit area), the distance  $s$  between tethered chains becomes smaller than their Flory radius. Dominated by excluded volume interactions, the chains are orientated preferably normal to the surface. However, the chains can be subdivided into "blobs" with a diameter equal to the distance  $s$  between the tethering points (Figure III-2). The number of monomers per blob is  $g_D$  so that the scaling law of Flory (cf. equation (2)) is maintained in each blob (equation (6)).

$$s \propto l \cdot g_D^{\frac{3}{5}} \quad (6)$$

Accordingly, the AdG model depicts a polymer brush as a combination of Flory chains stacked normal to the surface. Its brush thickness  $L_{AdG}$  scales with the grafting density  $\sigma_g$  and the number of monomers  $N$  (equation (7)).<sup>17</sup>

$$L_{AdG} \propto N \cdot \sigma_g^{\frac{1}{3}} \quad (7)$$

Using a self-consistent field theory, Milner, Witten and Cates (MWC)<sup>18</sup> treated the interactions in polymer brushes as an interplay of excluded volume interactions and stretching energy. In these mean-fields, the forces acting on every monomer of the structure are assumed as a constant external field, neglecting local fluctuations. Hence, they depend on the local concentration of the monomer.

While AdG assumed a constant concentration over the brush thickness (step profile), MWC found a parabolic concentration profile more suitable, particularly for long chains.<sup>18,19</sup> Nevertheless, the brush thickness in equilibrium turned out to follow a similar scaling like in the AdG model.<sup>19</sup>

### *Polyelectrolyte Brushes*

The mentioned theories have been deduced for neutral polymer brushes. Polymers with charged functional groups along the chain are polyelectrolytes. These charges contribute to interactions of the polyelectrolyte brush.

Generally, there is a distinction between strong and weak polyelectrolytes. Strong polyelectrolytes possess permanently charged groups. The charges in weak polyelectrolytes are pH-sensitive. Polyelectrolyte brushes differ from neutral polymer brushes in the magnitude of the forces which are extending the structure. The conformation of the chains is mainly dependent on the osmotic pressure of counter-ions trapped in the polyelectrolyte brush. This effect is stronger than excluded volume interactions and leads to a swelling of a polyelectrolyte brush in aqueous media. Similarly, the counteracting force is the chain entropy which is coiling the chains.

Strong polyelectrolytes have a stretched conformation in aqueous solutions at low ionic strength. Besides trapped counter-ions, the concentration of mobile ions in the polymer brush is minor resulting in high electrostatic repulsion between the charged chains (osmotic brush regime). Remarkably, the resulting brush thickness of a strong polyelectrolyte brush is independent of the ionic strength and the grafting density  $\sigma_g$ .<sup>20</sup>

The overall charge of weak polyelectrolyte brushes is not permanent. It depends on the dynamic equilibrium of proton association and dissociation of their functional groups. The concentration of charged groups at a certain pH value depends on their dissociation and can be calculated with the Henderson-Hasselbalch equation.<sup>21,22</sup>

In weak polyelectrolyte brushes, the loss in entropy due to the tethering is compensated by a more coiled conformation. This is induced by shifting the dissociation equilibrium to the uncharged species.

In the osmotic brush regime, the addition of salt leads to a swelling of the polymer brush. With increasing concentration of salt in solution, mobile ions migrate into the polymer brush. These additional charges influence the dissociation equilibrium charged groups so that an increasing repulsion between the chains can arise. The brush thickness increases with salt concentration  $c_s$  (equation (8)).<sup>20,23</sup>

$$L \propto c_s^{\frac{1}{3}} \quad (8)$$

For both strong and weak polyelectrolyte brushes, the conformation changes when the ionic strength in solution exceeds the charge concentration of the polyelectrolyte. The charges along the chains are screened by the added salt. This enables an entropically favored, more coiled conformation (salted brush regime). Consequently, the brush thickness decreases with the concentration of salt in solution  $c_s$  (Figure III-3).<sup>20</sup>

$$L \propto c_s^{-\frac{1}{3}} \quad (9)$$

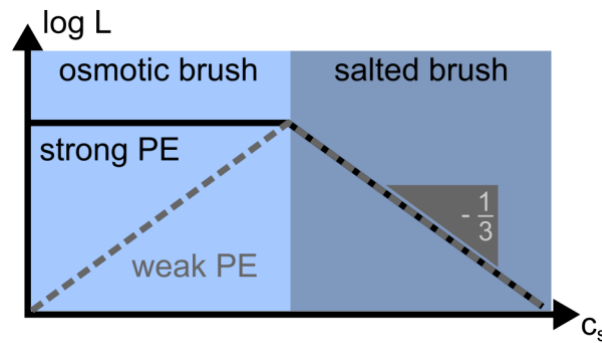


**Figure III-3.** Brush thickness  $L$  in logarithmic scale as a function of salt concentration  $c_s$  for strong (black solid line) and weak polyelectrolyte brushes (dashed gray line), divided in osmotic brush and salted brush regime.

Taking the grafting density and the salt concentration into account, Zhulina and Borisov predicted already a variety of regimes.<sup>20,24</sup> In addition to these two parameters, weak polyelectrolytes are also strongly responsive to pH. Although the polymer physics of brush structures discussed here give only a basic insight, it is to showcase already the crucial influence of few parameters to prepare and design responsive surface coatings.

### *Preparation Strategies and Responsiveness of Polymer Brushes*

Already from discussing their physical behavior, it can be derived that polymer brushes and polyelectrolyte brushes are highly responsive to external triggers, as for instance the surrounding solvent.<sup>25</sup> Attached to colloidal particles, the polymer brush were utilized to prevent colloidal flocculation.<sup>26</sup> Responsive to changes in their surrounding (e.g. solvent, salt, pH, temperature), switchable behavior is reported for various properties, for example, mechanics,<sup>27</sup> wettability,<sup>28,29</sup> friction in immersed<sup>30</sup> and dry state,<sup>31</sup> and adhesion.<sup>32,33</sup>

For designing polymer brushes as functional materials, the architecture and combination of the polymers used play a central role.<sup>34</sup> In this context, the combination of theory and

practice in synergistic simulation and preparation techniques can lead to a more fundamental understanding.<sup>35</sup> In principle, the preparation of polymer brushes can be achieved by two approaches, *grafting to* and *grafting from* the surface (Figure III-4A). Developments have led to brush structures in varying architectures and composition.

*Grafting to* the surface, the polymer is synthesized beforehand and covalently bond or physisorbed onto the surface. For a covalent bonding, functional groups of the polymer and the surface are required to match for coupling. Alternatively, parts of the polymer chain can be physisorbed on the surface so that the polymer is partially collapsed on the surface, and partially immersed in brush conformation.<sup>36</sup>

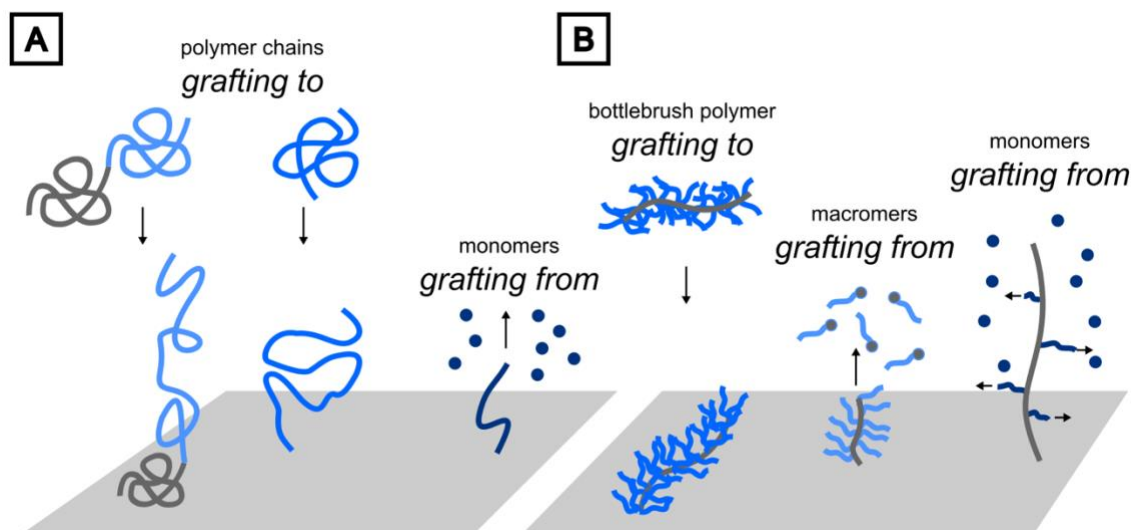


**Figure III-4.** (A) Scheme of *grafting to* and *grafting from* processes to form polymer brushes. (B) *Grafting to* and *grafting from* processes involving bottlebrush structures.

While entropic effects owing to steric interactions might prevent dense surface attachments in the *grafting to* approach, the structure can be polymerized *grafting from* the surface.<sup>15</sup> Commonly, an initiator is covalently attached to the surface for a subsequent surface polymerization. The grafting density is controllable with the concentration of initiator on the surface. Consequently, a grafting density higher than in the *grafting to* approach is possible with chains being able to grow in direct proximity. By lowering the initiator concentration, the mushroom regime can be achieved as well. In contrast, the *grafting to* approach has been demonstrated to render functional polymer brushes, overcoming the stigma of low grafting density and utilizing the possibilities of bulk polymerization.<sup>37</sup>

Therefore, a strict classification can only serve for explanatory reasons. Depending on the desired architecture and composition of the polymer brushes, the combination of surface

---

and bulk polymerization, and grafting approaches bears benefits in versatility. This is depicted exemplarily in the motif of the bottle brush.

Bottle brushes are polymer chains with side chains forming a brush structure around the backbone chain. This kind of structure further broadens the possibilities for polymer brush surface coatings (Figure III-4B).

Having polymerized bottle brushes in solution, they can be adsorbed on a surface so that the side chains are stretched away from the surface, forming a polymer brush. This was conducted by Pettersson et al.<sup>38</sup> to study the lubrication properties of these coatings under variation of side chain density and charge of the bottle brush backbone. Instead of solution polymerization, the bottle brush backbone can be prepared in a surface polymerization of macromers. Synytska et al.<sup>32</sup> prepared such surface grafted bottle brush structures with thermoresponsiveness for comparing their thermoswitchable adhesion with a model thermoresponsive polymer brush. Alternatively, a polymer brush is generated on a surface and side chains are grafted from the polymer brush chains subsequently to form surface tethered bottle brush. Gunkel et al.<sup>39</sup> utilized this method to vary the side chain architecture for studying the effect on antibiofouling properties of the surface coatings.

Besides versatility in polymer brush architecture,<sup>15</sup> patterning and gradients<sup>40</sup> were realized with varying composition,<sup>41</sup> grafting density,<sup>42</sup> or brush thickness.<sup>43,44</sup> These strategies have been proven to allow control over certain properties, e.g. wettability,<sup>45</sup> friction,<sup>38,46</sup> or adhesion.<sup>32</sup>

In this perspective, the developments in the preparation and theoretical understanding of polymer brushes pave the way for their further utilization as a material base for mechanosensitive surfaces.<sup>9,47</sup> Their defined conformational structure allows a predictable response to mechanical stress. Moreover, the possibilities in preparation offer a broad range of adjusting the responsiveness of these structures.



### III.1.3. Polymer Networks – Three-dimensional Functional Polymer Structures‡

As described in the previous paragraphs, polymer brushes are a class of surface coatings with well-defined interactions normal to the surface. At the same time, this can limit their dimensionality. Polymer brushes grafted on the surface of rigid particles represent an option to advance to the third dimension. When aiming for a three-dimensional mechanosensitive polymeric material, however, a three-dimensional polymer structure with isotropic mechanical properties is preferred as base. Ideally, the mechanical properties are scalable with the structure from the molecular level to the whole material.

#### *Polymer Network Models*

Polymer networks consist of interconnected chains. Their elasticity originates from the chain entropy in the network (cf. Rouse model, Section III.1.1), as described in the theory of Paul Flory and John Rehner.<sup>49,50</sup>

The crosslinks in polymer networks lead to transmission of acting stress and results in deformation of the network. Upon mechanical stress, the chain segments between the junction points are deformed. In a complementary idealized view, the network structure can be simplified to tetrahedral cells, each depicting one junction point surrounded by four others. The movement of the central junction point is restricted by the elasticity of the chains connecting to the corners (Figure III-5A). Hence, the chain elasticity of the connecting chains makes a displacement of the junction point far from the center less probable. Upon external stress, the idealized tetrahedral cell is deformed and the displacement of the central junction point is further restricted by the elongation of the connecting chains.<sup>49</sup>

Considering the structural entropy for the whole network from these tetrahedral cells, it becomes apparent that only segments connected at both ends contribute to the network elasticity, whereas network imperfections, such as dangling ends and loops cannot (Figure III-5B).<sup>49,51</sup>

‡ The topics of the second and third subsection have a thematic overlap with the trend article “Mechanically Defined Microgels by Droplet Microfluidics” by Heida, Neubauer et al.<sup>48</sup> Fragments of the text and selected figures in these sections were reprinted and adapted with permission, whereas the copyright remains with WILEY 2016.

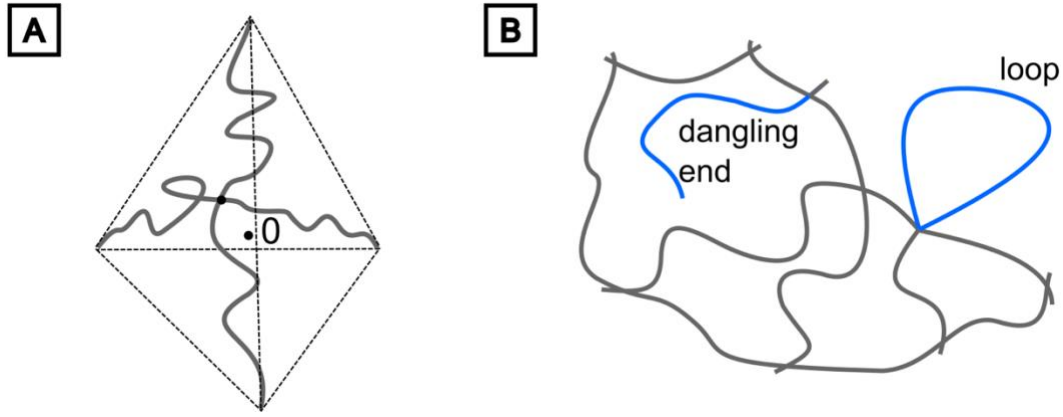


**Figure III-5.** (A) Flory's concept of a polymer network junction point represented as a tetrahedral cell. (B) Schematic illustration of network defects (blue).

So far, only the network elasticity has been mentioned. For instance, in hydrogel polymer networks, additionally solvent interactions come into effect. During the swelling of polymer networks, the polymer is solvated. An osmotic pressure leads to expansion of the network meshes. Simultaneously, the network elasticity is counteracting to the osmotic pressure. As a consequence, the solvation of the chains during crosslinking has a major effect on the mesh size and, therefore, on the swellability and elasticity.<sup>50,52</sup>

For an uncharged hydrogel prepared in water, Nikolaos Peppas and Edward Merrill derived the swelling equilibrium based on the Flory-Rehner theory (equation (10)).<sup>53</sup>

$$\frac{1}{M_c} = \frac{2}{M_n} - \frac{\bar{v}_P}{V_m} \frac{[\ln(1 - v_{P,s}) + v_{P,s} + \chi v_{P,s}^2]}{v_{P,r} \left[ \left( \frac{v_{P,s}}{v_{P,r}} \right)^{1/3} - \frac{1}{2} \left( \frac{v_{P,s}}{v_{P,r}} \right) \right]} \quad (10)$$

Equation (10) gives an expression for the molecular weight of a connecting chain  $M_c$  between two junction points. It depends on the molecular weight of the crosslinked primary chains  $M_n$  at which junction points along the chain are generated during crosslinking. The solvation state is considered by the volume fraction of the polymer in swollen state and in relaxed state immediately before crosslinking  $v_{P,s}$  and  $v_{P,r}$ , respectively.  $\bar{v}_P$  is the specific volume of the polymer,  $V_m$  is the molar volume of the solvent (water).

The deformation of the tetrahedral cells in the direction of the strain is given by the ratio  $\alpha$  of the deformed length to the initial length. For hydrogels prepared in solution, it relates to the applied tensile stress  $\tau_{\text{tens.}}$  as put in equation (11).<sup>53</sup>

$$\tau_{\text{tens.}} = \frac{RT}{\bar{v}_P M_c} \left( 1 - \frac{2M_c}{M_n} \right) \left( \alpha - \frac{1}{\alpha^2} \right) \left( \frac{v_{P,s}}{v_{P,r}} \right)^{\frac{1}{3}} \quad (11)$$

$R$  is the universal gas constant,  $T$  is the absolute temperature during the experiment so that the first factor of the equation takes the thermal movement of the connecting chains into account. The second factor consists of a relation of  $M_c$  to  $M_n$ , expressing a vague measure for crosslinking density. The solvation state during crosslinking is reflected in the fourth factor. Having showcased mechanical and solvation influences, the swelling equilibrium can also be influenced by geometrical constraints<sup>54</sup> and ionic contributions from charged groups in the hydrogel.<sup>55</sup>

Bridging the scale between the molecular and macroscopic level, the elastic modulus  $G$  can be related to the number density of elastically effective chains  $\rho_{N,\text{elast}}$  (equation (12)).<sup>51,56</sup>

$$G_{\text{affine}} = \rho_{N,\text{elast.}} \cdot k_B T \quad (12)$$

$k_B$  is the Boltzmann constant. Based on the work of Kuhn and Treolar, Flory and Rehner developed an affine network model. One of its boundary conditions is that the displacement of the junctions occur in affinity with the macroscopic deformation. Further, the volume during deformation does not change.<sup>57</sup>

In contrast, James and Guth presented the phantom network model.<sup>58</sup> It bears the assumption that only junctions at the surface are fixed and in affine deformation with macroscopic strain. The junctions and chains in the bulk can fluctuate about their mean values, like “phantoms”.<sup>57</sup> Therefore, accounting for the number density of active junctions  $\rho_{N,\text{junct.}}$ , it predicts comparably lower moduli (equation (13)).<sup>56,58</sup>

$$G_{\text{phantom}} = (\rho_{N,\text{elast.}} - \rho_{N,\text{junct.}}) \cdot k_B T \quad (13)$$

These two models can be seen as limiting cases so that the transition has been investigated.<sup>56</sup> In literature, the mechanics of swollen hydrogel networks are discussed in more detail.<sup>57,59,60</sup>

---

Conceptually, these models allow insight into the network structure from macroscopically measuring elasticity. But just as well, they offer design criteria for hydrogel networks with defined mechanical properties.

One central assumption in the Flory-Rehner theory is that the network can be described with tetrahedral cells of chains with equal contour length (Figure III-5A).<sup>49</sup> Whereas this idealized model is able to describe actual networks during macroscopic deformation, heterogeneities in the network structure exist and can be resolved with techniques for deformation on the microscale.<sup>61</sup> Accordingly, the scale of the network homogeneity has to be fitted to the scale of the mechanical actor for preparing an actual network which can be described with an idealized network.

Alongside with a defined network structure from the micro- to the macroscale, its mechanical properties need to scale all over the network in the same fashion. By using the Flory-Rehner model as a blueprint for a homogeneous network, the mechanical properties on the microscale can be derived from macroscopic experiments.

Furthermore, the model suggests a perfectly crosslinked network structure. Dangling ends and loops do not contribute to elasticity,<sup>51</sup> but occupy volume. Therefore, they too embody heterogeneity which is to be avoided.

In conclusion, an ideal mechanically defined hydrogel network should consist of chain segments of the same length and perfect crosslinking for identical mechanical properties all over the network.

To manage the balancing act of controlling the network from the molecular to larger length scales, a combined approach might lead to the desired structure. Generating hydrogel particles with droplet microfluidics, the hydrogel network can be constructed with a variety of crosslinking strategies while limiting the reaction volume in a droplet, above molecular and below macroscopic scale.<sup>48</sup>

In the following, a brief introduction to droplet microfluidics and strategies for generating hydrogel particles with this technique is given.

### *Droplet Microfluidics for the Generation of Hydrogel Particles*

Microfluidics is a technique about microliter amounts of fluids in channel structures with dimensions on the order of several tens of micrometers.<sup>62</sup> Since its first applications,<sup>63</sup> microfluidics have emerged to an own field of research with various techniques and applications.<sup>62</sup> Among these, droplet microfluidics can be applied for utilizing microdroplets of defined size as reaction volumes, and for generating emulsions or particles.<sup>64,65</sup>

Commonly, microfluidic devices are produced by soft lithography.<sup>66,67</sup> In this technique, the desired microfluidic channel structures are molded with elastomers from positive structures generated with photolithography. Alternatively, droplet microfluidics can be performed in glass capillary devices, for instance.<sup>68</sup>

While soft lithography has the advantage of high reproducibility for manufacturing devices, however, optimization of the channel structures can be time-consuming. Changes in the microfluidic structure have to be incorporated in the photolithography masks so that minor changes demand the repetition of the whole production cycle. Recent developments aim toward fabrication with additive manufacturing techniques.<sup>69</sup>

In droplet microfluidics, usually two immiscible fluids are led separately to a junction where droplets of the disperse phase are formed in the continuous phase. Widely known geometries for the junction are coaxial, cross-flow, and T-junctions. Depending on the geometry, the viscosities of the fluids and their surface tension, and the flow rates of the phases, different regimes can be achieved (Figure III-6).<sup>70</sup> Typically, the dripping regime is used for the controlled formation of droplets. Furthermore, the droplet size can be controlled by proficient adjustment of the flow rates and utilization of the jetting regime.<sup>71</sup>

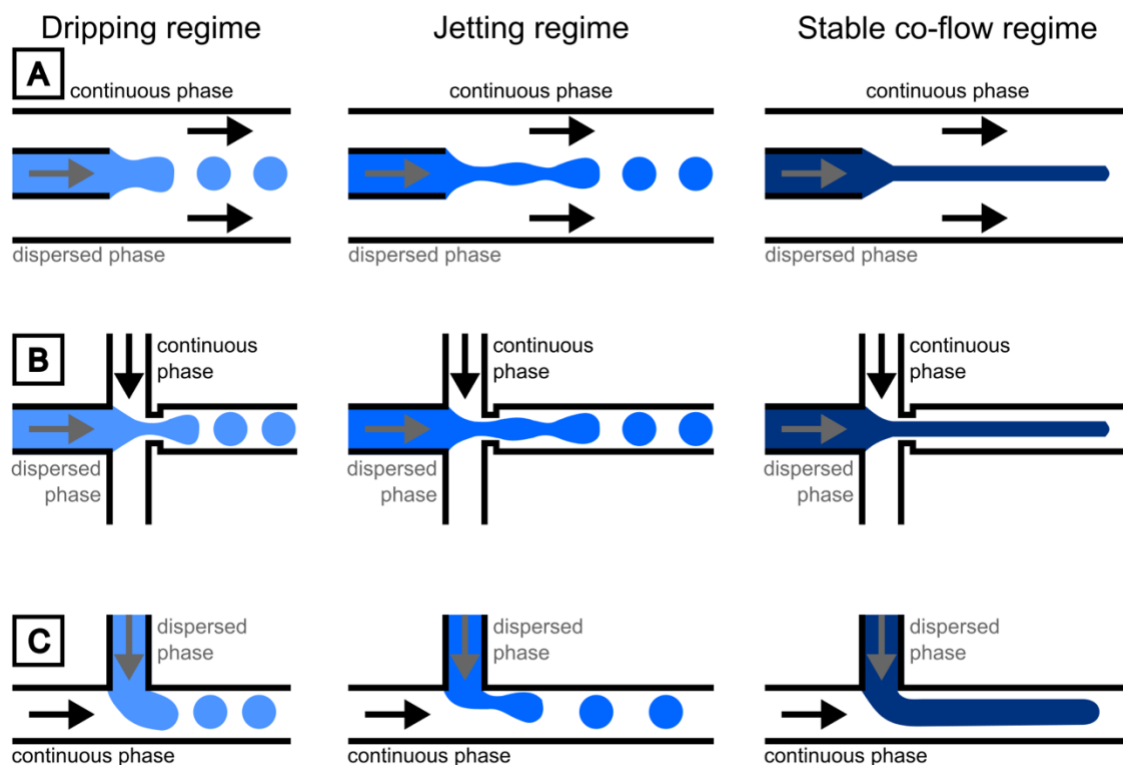


**Figure III-6.** Scheme of flow regimes of immiscible phases (dispersed and continuous phase) for a coaxial junction (A), a cross-flow junction (B), and a T-junction (C). The dripping, jetting, and stable co-flow regime are given for each junction in the respective column. Reproduced with permission and adapted from Nunes et al.<sup>70</sup> Copyright IOP Publishing 2013.

For the stabilization of the droplets against coalescence, surfactants are added to the continuous phase. When hydrogel particles are to be generated, the disperse phase is usually aqueous. Consequently, hydrocarbon<sup>72-75</sup> or fluorocarbon oils<sup>76-78</sup> are often chosen for the continuous phase. Besides the nature and composition of the droplet, the surfactant has to be chosen with respect to the oil. Often, commercially available surfactants are used in hydrocarbon oils<sup>72-75</sup> and self-synthesized surfactants based on perfluoropolyether (PFPE)<sup>79,80</sup> are used in fluorocarbon oils.<sup>76-78</sup>

The laminar flow in microfluidic channels causes a circulating flow pattern in the droplets axiosymmetrical in the flow direction so that both halves are mixed separately.<sup>81</sup> Therefore, the mixing of droplets in microfluidic structures has been studied in detail.<sup>82,83</sup> In particular, meander structures in varying geometries influence the flow profiles for enhanced mixing throughout the whole droplet (Figure III-7).<sup>84-87</sup>

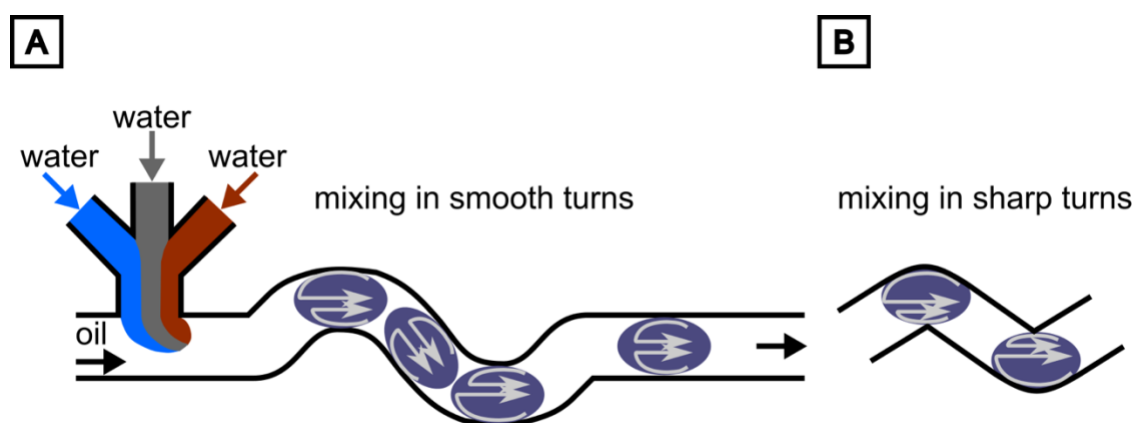


**Figure III-7.** (A) Water droplets in oil generated at a T-junction. Starting from a blue and red colored dispersed phase, the droplets appear violet from mixing. The droplet flow pattern during mixing in a smooth turning meander structure is visualized (gray arrows). Reproduced with permission and adapted from Song et al.<sup>82</sup> Copyright WILEY 2003. (B) For comparison, droplet flow patterns during mixing in a sharp turn meander structure. Reproduced with permission and adapted from Bringer et al.<sup>84</sup> Copyright The Royal Society 2004.

Microfluidic mixing and surfactant stabilization might have to be optimized depending on the hydrogel system. As various as the hydrogel systems are the gelation procedures. Typically, they are distinguished between on-chip and off-chip. For instance, it is advantageous to trigger photoinitiated gelation on-chip<sup>68</sup> because it ensures identical exposure on each droplet. Other triggers, such as temperature, might be conducted more convenient off-chip after collecting the microemulsion in a vial.<sup>88</sup>

For separating the particles from the continuous phase after reaction or gelation, the surfactant is removed and the particles are transferred to a different phase (e.g. aqueous for hydrogel particles). By addition of a poor surfactant, the emulsion breakup can be triggered to enable a phase transfer of the destabilized hydrogel particles.<sup>89,90</sup> Although this step is usually performed to extract the yielded particles from the collected continuous phase, the addition of a poor surfactant can as well induce particle coalescence at a defined position in the microfluidic setup.<sup>91</sup>

In addition to the possibilities arising from droplet microfluidics, the choice of materials, reaction and gelation for generating hydrogel particles further enhances the toolbox for designing mechanically defined hydrogel networks.

---

### *Generation of Hydrogel Particles with Control over Network Structure*

As introduced in the previous section, the precise control over microdroplet formation via microfluidics can be utilized to generate templates for hydrogel particle fabrication. Microgels are also hydrogel particles, but their terminology usually relates to dimensions in the colloidal range.<sup>92,93</sup> Therefore, the term hydrogel particle is used in this section to include all kinds of hydrogel microparticles with defined mechanics, tailored properties, and controlled structure.

Conceptually, hydrogel particles can be polymerized and crosslinked from droplets of monomers or polymer precursor solutions. This results in differently structured polymer networks and directly affect their mechanical behavior. The fundamental aspects of polymer network models are described above.

When hydrogels are generated by free radical polymerization in a microdroplet with monomer and crosslinker, the resulting network structure is heterogeneous with variations in crosslinking density.<sup>94,95</sup> In this context, Di Lorenzo et al. investigated the effect of heterogeneities on network elasticity.<sup>61</sup> By varying the amount of crosslinking moieties in linear precursor chains, heterogeneities were induced purposely in the polymer network. The effect on the mechanics of the network structure could be elucidated by probing the elasticity on different length scales.

In general, macromolecular precursors can not only be advantageous to gain control over crosslinking heterogeneities. Moreover, synthesizing the polymer precursors beforehand offers control over the chain length, the number of adjacent chains, and the position of crosslinking moieties via well-established polymer synthesis methods.

With this broad range of parameters in polymer precursor design, hydrogel particles can be adapted to their designated application, for example as platform for cell cultivation. It was shown that the elasticity of the microenvironment can influence the lineage specification of stem cells.<sup>7</sup> Offering the possibility to encapsulate cells with droplet microfluidics, the hydrogel can serve as 3D microenvironment resembling the one of the natural extracellular matrix (ECM)<sup>96</sup> with the potential to influence cell differentiation also on the particle level.<sup>76</sup> Therefore, many concepts for hydrogels with defined or tunable mechanics discussed here aim for an application in biotechnology.

As for other aspects, the crosslinking strategy is considered in accordance with the application. To avoid potentially cell-harming UV-initiated crosslinking in the presence of living cells, bio-orthogonal reaction schemes have been in the focus of recent research.<sup>97</sup>



Widely applied gelation routes are based on Michael-type additions<sup>75,76,98,99</sup> and click chemistry.<sup>73,100</sup> Alternatively, supramolecular and ionic interactions<sup>74,101-103</sup> as well as enzymatic crosslinking,<sup>78,104</sup> but also UV-initiated crosslinking are utilized.<sup>68</sup>

As important as the choice of the crosslinking strategy is the choice of the materials for hydrogel formation. In addition to mechanical demands, further requirements have to be taken into account, such as the integration of functional groups for cell adhesion for the already mentioned application in cell cultivation. On the one hand, biopolymers, as for instance gelatin or collagen, offer binding sites analog to the ECM in living tissues, but tend to be polydisperse in chain length. On the other hand, synthetic polymers can be yielded with low polydispersity, but might lack of binding sites for cells or even biocompatibility. These material demands and applications are discussed elsewhere.<sup>105-107</sup> In the following, the variety in integrating especially mechanical, but also other functionalities in hydrogel particles is showcased by individual concepts. The selection is almost exclusively limited to hydrogel particles prepared with microfluidics.

Based on the biopolymer agarose, hydrogel particles with variation in elasticity could be fabricated by utilizing microfluidics for mixing precursor solutions of two concentrations (Figure III-8).<sup>88</sup> By varying the concentration in the resulting droplets, a 35-fold variation of the shear elastic modulus was reported. Also by blending agarose with modified gelatin, tunable stiffness could be achieved.<sup>78</sup> While agarose was gelled thermally in both cases, the gelatin had been modified for peroxidase-catalyzed crosslinking. To enable photo-initiated radical crosslinking, gelatin can be functionalized with methacrylate.<sup>68</sup>

With synthetic polymers, precursors of varying length and composition can be employed to control the network formation and its resulting properties.<sup>72,99</sup> Functionalization of the synthetic precursors can, for instance, include integrins as cell binding sites,<sup>75</sup> but also peptides for enzymatic reactions.<sup>98</sup>

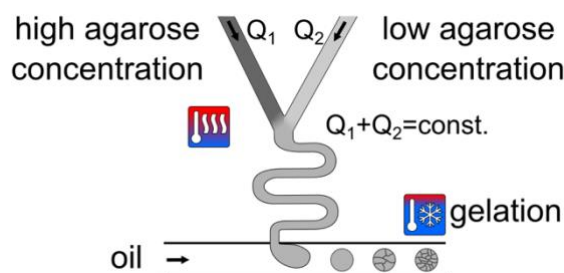


**Figure III-8.** Microfluidic structure for blending two streams with differing agarose concentration to adjust the mechanical properties of the agarose particles after gelation. Reproduced with permission and adapted from Kumachev et al.<sup>88</sup> Copyright Elsevier 2011.

Besides functionality for biochemical interactions, mechanical functionality can be integrated in hydrogel particles. By coating core hydrogel particles of the thermoresponsive poly(*N*-isopropylacrylamide) (PNIPAAm) with polyacrylamide (PAAm), core-shell particles with switchable elasticity could be generated.<sup>108</sup> The adhesion was independent of the temperature in contrast to the behavior of pure PNIPAAm. Inversing the morphology, PAAm/PNIPAAm core-shell particles were reported to enable temperature-triggered release of macromolecules.<sup>109</sup> Grafting PNIPAAm sidechains into a hydrogel network, the resulting particles were found to switch elastic moduli with temperature (Figure III-9).<sup>73</sup>

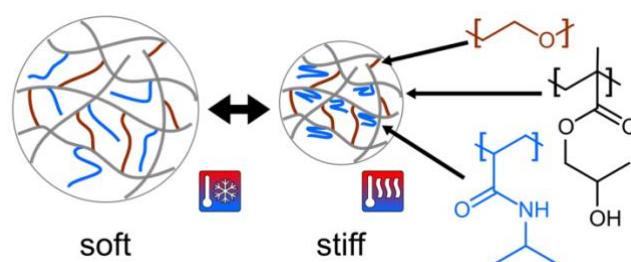


**Figure III-9.** Scheme of thermoresponsive hydrogel particles switching elasticity. The network is prepared from two precursors (red and black) with thermoresponsive PNIPAAm sidechains as dangling ends (blue). Reproduced with permission and adapted from Hackelbusch et al.<sup>73</sup> Copyright WILEY 2015.

Mechanics of a hydrogel network cannot only be switchable. Also, triggered degradation of networks is reported, for example, by disengaging ionic crosslinks in competitive complexation,<sup>74</sup> and by pH-triggered cleavage.<sup>100</sup>

Utilizing switchability of hydrogels, efforts are invested in the direction of particle-based actuators.<sup>110</sup> Photostructured hydrogels were actuating in valve applications,<sup>111</sup> as well as hydrogel particles.<sup>112</sup>

In the perspective of the design of mechanoresponsive hydrogel particles, actuation and fluorescence in hydrogels were coupled,<sup>113</sup> but also pH- and thermoresponsiveness was incorporated for fluorescence response in hydrogel particles.<sup>114</sup>

## III.2. Atomic Force Microscopy – Applying Forces and Investigating Mechanics

For the mechanical characterization of polymers, standardized methods are established to determine their specifics, such as the elastic modulus by tensile tests (e.g. DIN EN ISO 527) or bending tests (e.g. DIN EN ISO 178). Additionally, viscoelasticity in polymers causes mechanics to be dependent on temperature, time, and the rate of deformation. Also, standardized tests can be conducted to determine this behavior (e.g. DIN EN ISO 6721).

Standard measurements are usually performed with standardized specimens in the context of commercial and industrial applications to ensure comparability. These measurements are usually macroscopic approaches giving mechanical properties averaged over the whole specimen body. However, macroscopic approaches are also applied in the context of research, e.g. by tensile,<sup>115,116</sup> compression,<sup>117,118</sup> and rheology tests<sup>73,88,119</sup> on hydrogels. In contrast, microscopic approaches probe the sample on a smaller order of magnitude. Especially in the context of polymer networks, microscopic methods are able to elucidate mechanical heterogeneities.<sup>61</sup> Thus, the combination of different methods probing various length scales can assist in understanding specific properties.<sup>120</sup>

For the microscopic approaches, indentation experiments are among the most prominent examples. They can be performed both on macroscopic and microscopic samples. Whereas the size of the probe is key in indentation experiments, further methods are suitable for microscopic samples. Besides the renowned atomic force microscopy discussed in the following sections, microparticle hydrogel systems are investigated with optical tweezers,<sup>121</sup> or micropipettes.<sup>78</sup>

---

### III.2.1. Principles of Atomic Force Microscopy

Atomic Force Microscopy (AFM) is a scanning probe microscopy technique developed by Binnig et al.<sup>6</sup> The underlying principle is the detection of forces arising from long- and short-range interactions between the probe and the sample.

In AFM, the probe usually is a tip located at the end of a cantilever. For imaging a sample, the cantilever or the specimen stage are moved with piezo actuators to scan in  $x$ - and  $y$ -direction (tip scanner or sample scanner). Also in  $z$ -direction, piezo actuators approach and retract the cantilever. The interaction forces between the probe and the sample deflect the cantilever. Its deflection is determined with an optical lever by focusing a laser on the cantilever. The laser is reflected onto a 4-quadrant photodiode allowing to detect vertical and lateral cantilever deflections from the optical lever deflections as changing voltage in the photodiode. Originally, AFM was developed as an imaging technique. Capable of detecting forces on the nanoscale, it is also used for the quantification of interactions and mechanical properties.<sup>122,123</sup>

For imaging, the tip is scanned over the sample surface, recording interactions spatially resolved to generate an image. Utilizing a feedback loop between the  $z$ -piezo actuator and the photodiode, the deflection of the cantilever can be kept constant by compensating deflection changes with  $z$ -adjustments. By correlating the  $x$ - and  $y$ -position during scanning with the  $z$ -position from the feedback, a three-dimensional image can be generated (Figure III-10). Alternatively,  $z$  is not changed so that the deflection of the optical lever is recorded spatially resolved. In contrast to the former, the force during scanning is not constant as the deflection of the cantilever changes. In both modes, strong shear forces are acting on the tip and the sample during scanning.

In intermittent contact mode or TappingMode™, the cantilever is vibrating close to its resonance, resulting in intermittent contact of the tip. The shear forces are reduced, but during damping, a complex combination of forces appears.<sup>124</sup> Similarly, a three-dimensional image is generated by scanning the sample and adjusting  $z$  in a feedback loop for maintaining a predefined damped cantilever amplitude.<sup>125</sup> The phase shift during damping can change depending on the elasticity of the sample. Therefore, variations in the elasticity of the sample can be visualized in the phase image qualitatively.<sup>126</sup>

Further, the AFM has been employed as a base for spatially resolved measurements of electrical properties,<sup>127-129</sup> or infrared spectroscopy, for instance.<sup>130</sup>

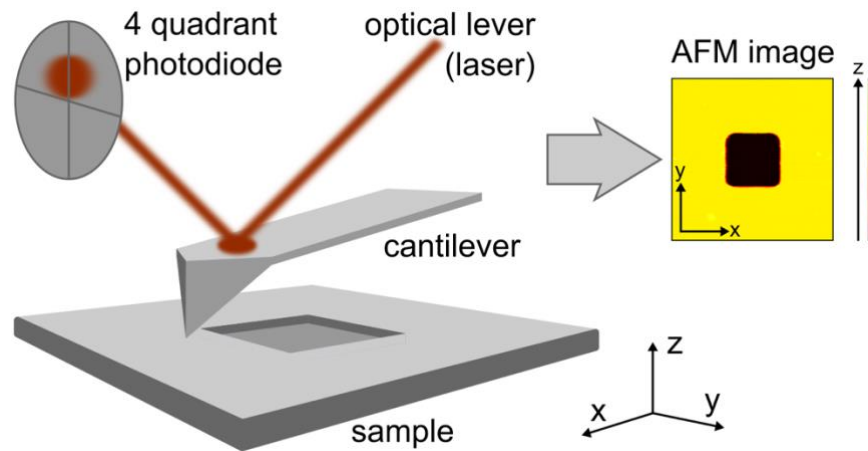


**Figure III-10.** Schematic setup of an atomic force microscope. For imaging, a tip probe at the apex of a cantilever is scanned over a surface utilizing piezo elements (not shown). Surface interactions with the probe change the deflection of the cantilever, detected via an optical lever onto a photodiode. From this data, an image can be generated.

### III.2.2. Force Measurements with Atomic Force Microscopy

AFM is based on the interactions between the probe and the sample. They are detected by the deflection of a cantilever spring over an optical lever. As a consequence, local interaction forces can be quantified in force measurements. Vice versa, defined contact forces can be applied in imaging. In the following, a brief introduction to AFM force measurements is given. Detailed information to this widely applied technique is found in the review by Butt, Capella, and Kappl.<sup>122</sup>

In force measurements, long-range, short-range, and contact interactions of the probe and a sample can be determined. For this purpose, the deflection of the cantilever and the displacement of the  $z$ -piezo actuator are recorded (Figure III-11).

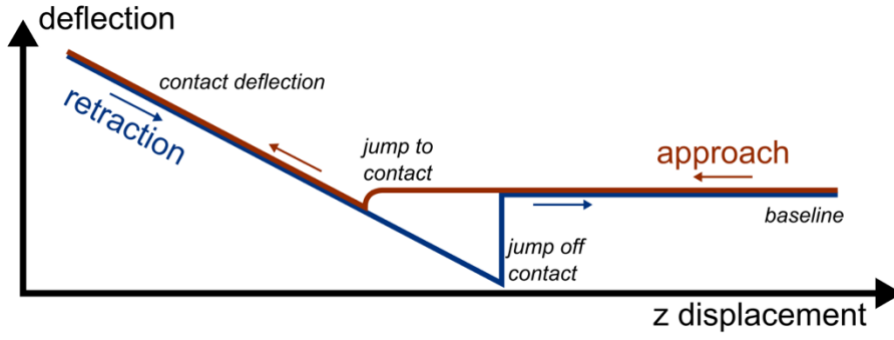


**Figure III-11.** Exemplary deflection-displacement curve of an AFM cycle, consisting of approach (dark red line) and retraction (blue line).

When a cantilever is approached to a surface, no interactions are measured at large distances (baseline). Closer to the surface, attractive and repulsive long- and short-range interactions can deflect the cantilever. If the attractive interaction exceeds the elastic energy of the cantilever, it snaps toward the surface (jump to contact). In contact with the surface, the cantilever is deflected linearly according to Hooke's law.

Upon retraction, the deflection is decreased linearly. If adhesive interactions are present, the cantilever can be deflected negatively. When the elastic energy of the cantilever exceeds the adhesion, the probe is detached from the surface (jump off contact) to the baseline deflection.

As a cantilever is a Hookean spring, the interaction forces between the probe and the sample can be quantified if the spring constant of the cantilever  $k_c$  and its deflection  $\delta$  is known (equation (14)).

$$F = k_c \cdot \delta \quad (14)$$

By deflecting the cantilever on a non-deformable substrate,  $\delta$  is in a linear relationship with the displacement of the  $z$ -piezo actuator. Simultaneously, the deflection of the optical lever is measured as photodiode signal  $U$ . Therefore, the relation between the  $z$ -piezo displacement and  $U$  can be determined from the slope of deflection-displacement curves as the optical lever sensitivity  $S_{OLS}$ . To calculate  $\delta$  from  $U$ , the inverted optical lever sensitivity ( $[S_{InvOLS}] = \text{nm/V}$ ) is used (equation (15)).

$$\delta = S_{InvOLS} \cdot U \quad (15)$$

Further, the spring constant  $k_c$  of the cantilever must be known to quantify forces. It can only be calculated, if its dimensions and its material composition are known exactly (equation (16)).<sup>131</sup>

$$k_c = \frac{E_c w_c t_c^3}{4 L_c^3} \quad (16)$$

The Young's modulus of the cantilever is denoted as  $E_c$ ;  $w_c$ ,  $L_c$ , and  $t_c$  are its width, length, and thickness. Particularly, variations in the thickness strongly influence the spring constant so that various experimental calibration methods were developed.<sup>132-134</sup> For example, Hutter and Bechhoefer showed that  $k_c$  can be determined from the thermal fluctuations of the cantilever. Undisturbed from sample interactions, the cantilever is assumed as harmonic oscillator deflected from the thermal energy  $k_B T$ . According to the equipartition theorem, the thermal energy is equal to the vibrational energy (equation (17)). Plotting the power spectra of the vibrational frequency, the mean square deflection  $\langle \Delta Z_c^2 \rangle$  of the cantilever can be fitted from the fundamental resonance peak enabling the determination of  $k_c$ .<sup>132</sup> Higher vibrational modes are taken into account by correction factors.<sup>122</sup>

$$\begin{aligned} \frac{1}{2} \cdot k_B T &= \frac{1}{2} \cdot k_c \cdot \langle \Delta Z_c^2 \rangle \\ \Rightarrow k_c &= \frac{k_B T}{\langle \Delta Z_c^2 \rangle} \end{aligned} \quad (17)$$

After the calibration of the sensitivity and the spring constant, the forces acting on the cantilever can be calculated according to equation (18).

$$F = k_c \cdot \delta = k_c \cdot S_{\text{InvOLS}} \cdot U \quad (18)$$

Depending on the experiment, the force is evaluated as a function of the separation from the sample surface  $D$  or as a function of the indentation  $d$  of the sample. In the idealistic case of no forces acting between the cantilever and the sample surface,  $D$  is identical to the  $z$  piezo-displacement  $Z_p$ . The sample and the probe come into contact at  $Z_p = 0$ .

Owing to attractive or repulsive surface interactions, the cantilever can be deflected out of contact, even in long ranges. Then, the actual separation  $D$  is a combination of the  $z$ -piezo

---

displacement and the deflection of the cantilever. Thus,  $D$  is calculated from the piezo displacement  $Z_p$  and the cantilever deflection  $\delta$  (equation (19)).<sup>122</sup>

$$D = Z_p + \delta = Z_p + \frac{F}{k_c} = Z_p + S_{\text{InvOLS}} \cdot U \quad (19)$$

If repulsive forces act on the cantilever,  $D$  becomes larger than  $Z_p$  ( $U > 0$ ); if attractive forces act on the cantilever,  $D$  becomes smaller than  $Z_p$  ( $U < 0$ ).

In contact,  $Z_p$  causes both a deflection of the cantilever  $\delta$  and an indentation  $d$  into the sample. By definition,  $Z_p$  is negative in contact. Accordingly,  $d$  can be calculated as negative separation (equation (20)).

$$d = -Z_p - \delta = -D \quad (20)$$

Applying these relations, the deflection-displacement data of the cantilever can be converted to force-deformation curves of the sample for the evaluation of mechanical properties (Figure III-12). It needs to be stressed that the conversion is crucially dependent on the absolute value the contact point is defined to. For surface interactions of infinitely hard samples, the contact point usually is determined at the intersection between the baseline and the constant compliance deflection of the cantilever. For deformable materials, the onset of a restoring force of the sample can be taken as contact point. For deformable materials with repulsive long interactions, the determination of contact can be ambiguous.<sup>122</sup>



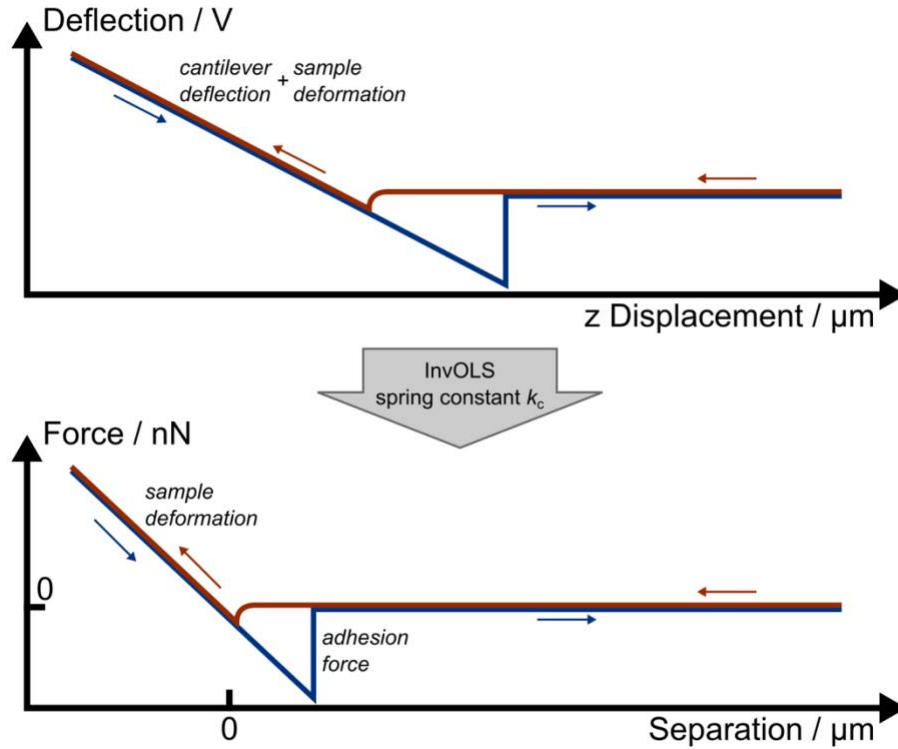


**Figure III-12.** Exemplary illustration of the conversion from a deflection-displacement curve, consisting of approach (dark red line) and retraction (blue line). The deflection-displacement curve comprises cantilever deflection and sample deformation; the force-separation curve depicts solely the interactions and contact deformation of the sample.

### III.2.3. Colloidal Probe Technique and Continuum Contact Models

The measured force depends on the distance, but also on the interaction area.<sup>122</sup> For curved surfaces, the interaction area and distance geometrically depends on the curvature of the surfaces. By the Derjaguin approximation,<sup>135</sup> the relation between the interaction energy  $w$  and the measured force  $F$  is given (equation (21)), taking the curvature of the two interacting surfaces into account with the effective radius  $R_{\text{eff}}$ .

$$F(D) = 2\pi R_{\text{eff}} \cdot w(D) \quad (21)$$

$$\text{with } \frac{1}{R_{\text{eff}}} = \frac{1}{R_1} + \frac{1}{R_2}$$

For interpreting and evaluating AFM force data, the AFM probe's radius of curvature must be known. AFM tip radii are usually in the order of 10 nm.<sup>122</sup> With dimensions below the

optical diffraction limit, it has to be determined by electron microscopy. Moreover, the tip radius is susceptible to changes due to tip wear during experiments.

These uncertainties in the experiment can be overcome by using spherical micrometer-sized particles, so-called colloidal probes (CPs).<sup>136,137</sup> Usually, silica or glass beads are attached to cantilevers.<sup>122</sup> CP-AFM has been applied to investigate not only colloidal forces,<sup>136-138</sup> but also, for instance, electrostatic interactions,<sup>139,140</sup> adhesion,<sup>141</sup> and interactions of polymer brushes.<sup>36,142,143</sup>

The contact interactions of a CP with polymer particles can be described with continuum contact mechanics.<sup>108,144-146</sup> In contrast to actual materials consisting of molecular, subordinate and superordinate structures, the continuum theory idealizes materials to be dividable into infinitesimal small units. Continuum mechanics is based on this theory to describe the behavior of matter under load and deflection. A comprehensive introduction to this field is published by Lai et al.<sup>147</sup>

Originally, Heinrich Hertz<sup>148</sup> derived the deformation  $d$  of two macroscopic elastic spheres (equation (22)).

$$F(d) = R_{\text{eff}}^{\frac{1}{2}} \cdot K \cdot d^{\frac{3}{2}} \quad (22)$$

$$\text{with } \frac{1}{K} = \frac{3}{4} \left( \frac{1 - \nu_1^2}{E_1} + \frac{1 - \nu_2^2}{E_2} \right)$$

Knowing the effective radius  $R_{\text{eff}}$  of the CP and the deformed particle, their reduced Young's modulus  $K$  can be evaluated from AFM force-deformation. It consists of the Young's moduli  $E_i$  and the Poisson ratios  $\nu_i$  of the two deformed bodies. Often, the contribution of the rigid CP to  $K$  is considered to be negligibly small when deforming polymeric particles.<sup>144</sup>

Certain assumptions are preconditions for the Hertz model, such as the deformed bodies are elastic and isotropic, the contact area is small compared to the bodies, there is no surface roughness, and the deforming pressure is exactly normal.<sup>148</sup> As a consequence, effects which are more dominating on the microscale, e.g., adhesion or friction, are neglected. This is reflected in the predicted contact area, expressed as contact radius  $a_{\text{Hertz}}$  (equation (23)).

$$a_{\text{Hertz}}^3 = \frac{R_{\text{eff}}}{K} F \quad (23)$$

The Hertzian contact area is determined solely by the geometry, elasticity, and applied force (Figure III-13A). In the model of Johnson, Kendall and Roberts (JKR), adhesion was treated as a major contribution to the contact interactions<sup>149</sup> so that hereinafter the interaction energy  $w$  is specified to the work of adhesion. The contact area results from an equilibrium of the mechanical work from the applied load, the elastic energy and the surface energy of the deformed bodies, giving  $a_{JKR}$  (equation (24)).

$$a_{JKR}^3 = \frac{R_{eff}}{K} \left( F + 3\pi R_{eff} w + \sqrt{6\pi R_{eff} w F + (3\pi R_{eff} w)^2} \right) \quad (24)$$

Besides the JKR model, also the model of Derjaguin, Müller and Toporov (DMT) considers additional interactions as significant contribution to the contact forming between two interacting spheres.<sup>150</sup> In contrast to the equilibrium consideration of JKR, the DMT model focusses on the short range interactions outside the contact area to influence the contact radius  $a_{DMT}$  (equation (25)).

$$a_{DMT}^3 = \frac{R_{eff}}{K} (F + 2\pi R_{eff} w) \quad (25)$$

Despite differing assumptions, both the JKR and the DMT model assume larger contact radii than the Hertz model owing to interactions in addition to elastic contributions (Figure III-13B).

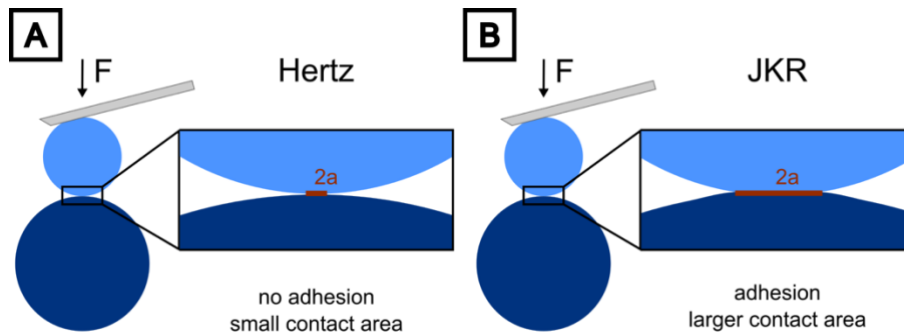


**Figure III-13.** Schematic depictions of the contact areas of two interacting spheres at a given force  $F$ , applied with AFM for the Hertz model (A) and the JKR model (B).

With the Hertz model neglecting adhesion, the contact radius of the JKR and the Hertz model is identical, if the work of adhesion  $w$  becomes zero. Utilizing interference

microscopy to monitor the contact area in the experiment, the soft colloidal probe (SCP) technique can be applied to determine  $w$ .<sup>151</sup> Employing elastomer spheres as cantilever probes, the load  $F$  is varied to investigate changes in the size of the contact area. Knowing the elastic moduli of both the sample and the SCP,  $w$  can be interpolated from the dataset of load-dependent contact radii.

Whereas an applied load results in a certain contact area, the pressure is not distributed uniformly over the contact area, but a pressure distribution under the CP is derived in all mentioned contact models. For the JKR model, an analytical description of the pressure distribution  $p(r)$  is given in equation (26).<sup>9,152</sup>

$$p(r) = p_0 \left(1 - \frac{r^2}{a^2}\right)^{\frac{1}{2}} + p_1 \left(1 - \frac{r^2}{a^2}\right)^{-\frac{1}{2}} \quad (26)$$

$$\text{with } p_0 = \frac{3Ka}{2\pi R_{\text{eff}}} \quad \text{and} \quad p_1 = -\sqrt{\frac{3Kw}{2\pi a}}$$

The local pressure  $p$  is expressed as a function of the radial distance  $r$  from the center of the contact area with radius  $a$ . Consisting of two terms,  $p_0$  is independent of the work of adhesion  $w$  and more dominant at small radii and decreasing with  $r$ , whereas the term  $p_1$  (comprising  $w$ ) becomes more dominant when  $r$  reaches  $a$ .

Visualizing the pressure distribution, it becomes more obvious that adhesion is acting rather at the edges of the contact area, observable as “negative pressure”. (Figure III-14).

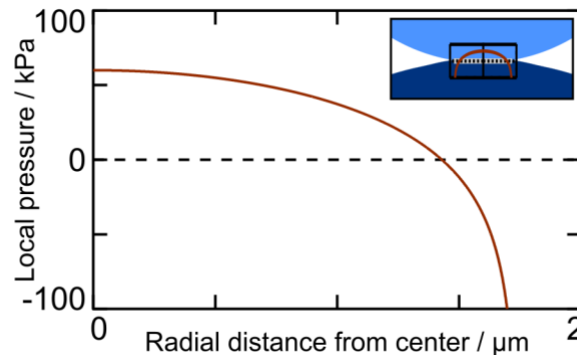


**Figure III-14.** JKR pressure profile in the contact area for two interacting spheres with  $R_{\text{eff}} = 30 \mu\text{m}$ ,  $E_1 = 2 \text{ MPa}$ ,  $E_2 = 2 \text{ GPa}$ ,  $\nu_1 = \nu_2 = 0.5$ ,  $w = 1 \text{ mJ/m}^2$ , and a load of  $F = 10 \text{ nN}$ , resulting in a contact radius of  $a = 1.75 \mu\text{m}$ . The inset schematically illustrates the position of the local pressures.

As short range interactions outside the contact area and adhesion can be present in varying ratio, Maugis managed to develop a model combining the DMT and the JKR theory as limiting cases.<sup>153</sup> Moreover, in the mechanical characterization of soft particles with AFM, differing contact models might be applicable for the contact to the substrate and the cantilever. To account for this, Glaubitz et al.<sup>154</sup> applied a mixed double contact model combining the JKR and the Hertz model.

In addition to the presented contact models and the mentioned development in this topic, a more detailed, comprehensive insight is given by Korayem and Taheri.<sup>155</sup>

---

### III.3. Fluorescence Effects – Optical Responses to Changes in Environment

#### III.3.1. Fluorescence

Fluorescence is an effect of luminescence. Explained in more detail below, it arises from the relaxation of an excited electronic state in the fluorescing molecule, the fluorophore. Therefore, fluorescence is based on the absorption and emission of light. As it is sensitive to changes in the environment of the fluorophore, fluorescence enables to optically investigate or follow processes.

Among a huge body of literature, a comprehensible access to this interdisciplinary field can be found in the textbook of Joseph R. Lakowicz,<sup>156</sup> on which the following fundamentals are based on.

Prior to fluorescence, an electronically excited state needs to be generated in the fluorophore, normally by the absorption of a photon. The resulting transition between a relaxed and an excited state happens within femtoseconds, quicker than the displacement of nuclei. Depending on the electronic and vibrational state, the probability densities of an electron varies locally. Therefore, a transition occurs only if the energy of the absorbed photon is equivalent to an allowed transition, according to the Franck-Condon principle<sup>157-159</sup> (Figure III-15, blue arrow). In the diagram, an allowed transition is depicted as a vertical step from the relaxed to an energetically higher state with probability density of an electron while maintaining the position on the ordinate of nuclei because the electronic transition is quicker than the nuclei displacement. If the energy of the photon does not match such an allowed transition, no absorption and, consequently, no change in electronic or vibrational state occurs.

If a photon is absorbed, the fluorophore is excited to the singlet states  $S_1$  or  $S_2$ , depending on the energy of the photon. Simultaneously, a higher vibrational state might be reached, e.g. from vibrational ground state in  $S_0$  to second vibrational state in  $S_1$  (as depicted in Figure III-15). Within picoseconds, the transition is followed by a relaxation to the vibrational ground state in  $S_1$  owing to internal conversion, as for instance, energy is dissipated in molecular collisions. In comparison, this relaxation is quicker than fluorescence with typical lifetimes in the order of 10 ns.<sup>156</sup>

Eventually, fluorescence occurs: a photon is emitted during the transition from the excited to the ground state, again following the Franck-Condon principle (Figure III-15, green arrow).

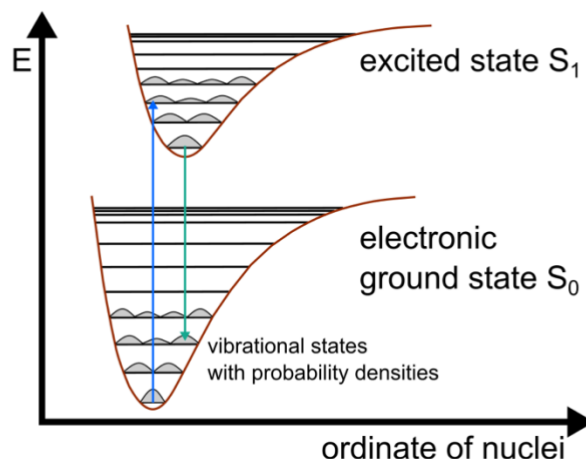


**Figure III-15.** Schematic examples of allowed transitions during absorption (blue arrow) and emission (green arrow) between two singlet states of a fluorophore according to the Franck-Condon principle.

In the diagram, the length of the arrows for absorption (blue) and emission (green) is equivalent to the energy of the photons absorbed and emitted in the process. Hence, the fluorescence spectra of fluorophores are red-shifted to their absorption spectra in general. The chosen example already gave an impression on the variety of processes able to occur. Usually, these excitation and relaxation process paths are overviewed in a Jablonski diagram (Figure III-16).

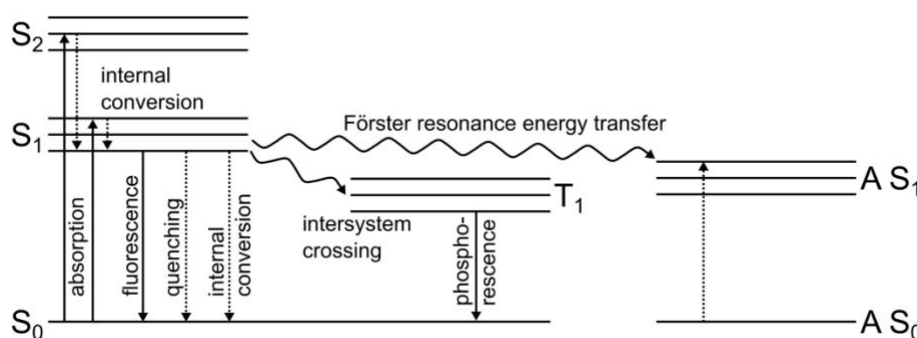


**Figure III-16.** Jablonski diagram with various excitation and deactivation processes. Solid arrows depict radiative processes, absorbing or emitting a photon, dotted arrows depict non-radiative processes, and curved arrows depict transitions from the singlet ( $S_x$ ) to another electronic state (triplet,  $T_1$ ) or another molecule (acceptor,  $A S_x$ ).

---

When a fluorophore is in the excited state, it can be deactivated in several processes under emission of a photon (radiative) or without any photon emission (non-radiative). Fluorescence is a radiative deactivation process.

Another radiative process is phosphorescence. It originates from an intersystem crossing from the singlet state  $S_1$  to the triplet state  $T_1$ . In  $T_1$ , the excited electron is in the same spin orientation as the remaining ground-state electron so that the transition to the ground state is forbidden. As a consequence, the deactivation rate is slower than for fluorescence. Phosphorescence lifetimes are typically in the order of milliseconds to seconds.<sup>156</sup>

Moreover, non-radiative deactivation processes are possible, comprising quenching, further internal conversion, photobleaching from chemical degradation (destruction of the fluorophore), and energy transfer to another molecule. The latter is non-radiative but can lead to the luminescence of the energy transfer partner, as discussed in the section below.<sup>156,160</sup>

As a measure to specify the fluorescence of a fluorophore, the quantum yield is defined as the ratio of the fluorescence rate and the sum of all radiative and non-radiative deactivation rates.<sup>156</sup>

In this regard, changes in the non-radiative deactivation rates can be determined experimentally as a change in fluorescence intensity, in particular from quenching. In general, it can be distinguished between dynamic and static quenching. Dynamic quenching is the deactivation of a fluorophore in excited state, e.g. by molecular collisions. In static quenching, the fluorescence is completely suppressed by the formation of a nonfluorescent complex between a quencher and a fluorophore in electronic ground state.<sup>156</sup>

The decrease in fluorescence from quenching is expressed in the Stern-Volmer equation (27).<sup>161,162</sup>

$$\frac{Fl_0}{Fl} = 1 + k_q \tau_0 [Q] \quad (27)$$

The fluorescence without quenching and in presence of a quencher is  $Fl_0$  and  $Fl$ , respectively. It is dependent on the quenching rate  $k_q$ , the quencher concentration  $[Q]$ , and the unquenched lifetime of the fluorophore  $\tau_0$ . Both for static and dynamic quenching, the ratio  $Fl_0 / Fl$  increases linearly with  $[Q]$ , but also intermediate states comprising both mechanisms have been reported in which  $Fl_0 / Fl$  increases nonlinearly.<sup>163</sup> Time-resolved



fluorescence measurements can help to identify the quenching mechanism by elucidating the lifetime.

Quenching effects were utilized in manifold concepts for sensing the environment of fluorophores, e.g. by employing oxygen as quencher,<sup>162</sup> and for detecting the presence of halides,<sup>164</sup> heavy metal ions,<sup>165</sup> or biomolecules.<sup>166</sup> Also, quenching effects have been utilized to monitor conformational changes in macromolecules for mechanosensing (cf. Section III.4).<sup>9,167</sup>

Quenching may not only originate from molecules in the environment of the fluorophore, but also self-quenching can appear, for example, owing to intramolecular quenchers<sup>168</sup> or the formation of non-fluorescent dimers.<sup>169</sup>

Besides quenching, also energy transfer to another molecule is a deactivation process, often exploited experimentally. It is introduced in the following section.

### III.3.2. Förster Resonance Energy Transfer

Förster resonance energy transfer (FRET) is an effect competing with fluorescence and other deactivation processes of excited fluorophores. By dipole-dipole interactions, energy can be transferred from an excited fluorophore, the donor, to an acceptor in close proximity. Essentially, the donor is absorbing light, whereas the acceptor is emitting light.

This effect is named after Theodor Förster. He described the transfer in the late 1940s,<sup>170,171</sup> further advancing models of dipolar energy transfer from Jean and Francis Perrin.<sup>172,173</sup>

The efficiency of the effect is critically dependent on the distance between the donor and the acceptor, typically in the range of 1 – 10 nm.<sup>174</sup> Therefore, it has been utilized as a “spectroscopic ruler”.<sup>175</sup> By adequate labeling, FRET is suitable for detecting molecular interactions<sup>176,177</sup> and for monitoring conformational changes.<sup>178-180</sup>

In the following, the fundamentals of FRET are described. More detailed explanations and further literature can be found in the textbook of Robert M. Clegg.<sup>160</sup>

As stated above, a fluorophore can be excited electronically by absorption of a photon according to the Franck-Condon principle. During FRET, the excited donor fluorophore is transferring energy to an acceptor fluorophore. From this transfer, the donor is deactivated

non-radiatively, whereas the acceptor ends up in electronically excited state from the transferred energy. Then, the excited acceptor is able to emit a photon.

However, there are two essential preconditions for FRET: There must be an overlap of the emission spectra of the donor and the absorption spectra of the acceptor. Further, the donor and the acceptor have to be in close proximity. The reasons for these preconditions are due to the underlying dipole-dipole interactions of the energy transfer.<sup>160</sup>

Assuming the donor in excited state as an oscillating dipole, it generates an electric field in its surrounding. Only in close proximity, an interaction with the dipole of an acceptor is possible. In case of resonance of both dipoles, energy can be transferred from the donor to the acceptor. However, the resonance condition depends that the energy for the transition between the initial and final state must match exactly for both molecules. With FRET being competitive to donor fluorescence, the energy transferrable from the donor in excited state corresponds to the donor fluorescence spectra. Vice versa, the absorption spectra of the acceptor fluorophore correspond to the energy required for electronic excitation. Accordingly, the energetic resonance condition between donor and acceptor can be depicted as spectral overlap. After FRET, the acceptor fluorophore is in excited state, enabling the emission of a photon.<sup>160</sup>

Despite the explanatory depiction of overlapping spectra, indeed no photons are generated during the actual FRET process, which conceptually would not limit the distance between the FRET donor and acceptor.

Owing to the nature of the underlying dipole-dipole interactions, however, the transfer rate  $k_t$  is critically dependent on the distance between the donor and the acceptor  $r_{DA}$  (equation 28)).<sup>160</sup>

$$k_t = \frac{1}{\tau_D} \cdot \left( \frac{R_{F\ddot{o}}}{r_{DA}} \right)^6 \quad (28)$$

Without FRET, the excited state of the donor decays at a certain rate  $\tau_D^{-1}$ , the inverse of its decay time. FRET is an additional deactivation path of the donor that competes with donor fluorescence and other non-radiative deactivation paths of the donor. Approaching an acceptor to the donor,  $k_t$  increases with decreasing  $r_{DA}$ . At the distance of one Förster radius

$R_{F0}$ , the energy transfer and the other deactivation processes of the donor occur at the same rate.

Consequently, the decay time in close proximity of an acceptor  $\tau_{DA}$  is shorter than the decay time  $\tau_D$  without an acceptor present. In accordance, the decay rates  $\tau_{DA}^{-1}$  and  $\tau_D^{-1}$  are the sum of all deactivation rates with and without an acceptor in proximity, respectively. Therefore, the transfer rate  $k_t$  can also be expressed as their difference (equation (29)).<sup>160</sup>

$$k_t = \frac{1}{\tau_{DA}} - \frac{1}{\tau_D} \quad (29)$$

Eventually, the efficiency of the transfer can be calculated from the decay times with and without the presence of an acceptor (equation (30)).<sup>160</sup>

$$\begin{aligned} \text{FRET eff.} &= \frac{\text{transfer rate } k_t}{\text{total deactivation rate}} = \frac{\frac{1}{\tau_{DA}} - \frac{1}{\tau_D}}{\frac{1}{\tau_D}} \\ &= \frac{\tau_D - \tau_{DA}}{\tau_D} \end{aligned} \quad (30)$$

Ensuing from these considerations, one can find an expression to describe the FRET efficiency as a function of the donor-acceptor distance  $r_{DA}$  (equation (31)).<sup>160</sup>

$$\text{FRET eff.} = \frac{1}{1 + \left( \frac{r_{DA}}{R_{F0}} \right)^6} \quad (31)$$

Knowing these relations, it becomes clear how FRET can be used as a spectroscopic ruler. The decay time is determined from the intensity decay of the FRET donor after an excitation pulse. Thus, advanced microscopy techniques, such as Fluorescence Lifetime Imaging (cf. Section III.3.3), even allow to measure the FRET efficiency and deduce the molecular distance of donor and acceptor fluorophores with high spatial resolution (Figure III-17).

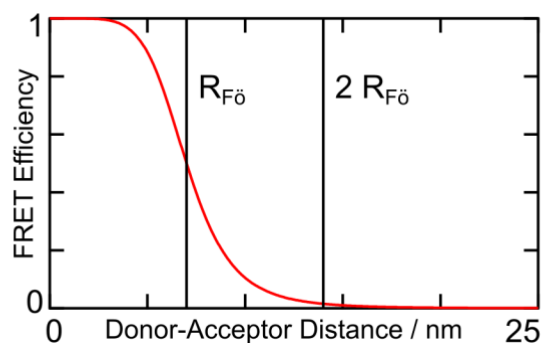


**Figure III-17.** Exemplary plot of the FRET efficiency as a function of the donor-acceptor distance, based on a Förster radius of  $R_{F0} = 7.0$  nm.

Although photobleaching is a deactivation pathway potentially interfering with FRET measurements, it can be used selectively for an intensity-based determination of the FRET efficiency.<sup>160</sup> In general, intensity-based determination of FRET might seem intuitive at first glance, but effects, as for instance spectral bleeding, can induce errors in the intensity measurements. Spectral bleeding originates from overlapping emission spectra of donor and acceptor: It is the detection of the donor emission in the acceptor channel and vice versa. Therefore, it needs to be compensated in the evaluation. Despite software plugins being available for evaluation,<sup>181</sup> it requires calibration samples of the donor and the acceptor independently, challenging the preparation procedures of the samples.

With the resolution of a “spectroscopic ruler” of FRET techniques, the variety of processes that might occur on molecular level requires sophisticated evaluation and interpretation of the data so that a variety of FRET imaging detection methods have been developed and proposed.<sup>182</sup>

### III.3.3. Origins and Developments of Confocal Microscopy

Optical microscopy can serve to localize and quantify fluorescence or FRET. For three-dimensional imaging, confocal microscopy can be utilized. Confocal microscopes exhibit an increased resolution by sectioning the focal plane.<sup>183</sup>

Their fundamental difference to conventional microscopy is the way the image is generated. Usually, a condenser is used for evenly illuminating the specimen, and an objective lens is used for generating the image of the specimen in the whole field of view. The depth of field can be large so that stray light from planes out of focus can lead to blurring.

In 1957, Marvin Minsky submitted a patent for a microscope, illuminating and imaging only a single point in the focal plane: the confocal microscope (Figure III-18A). Its light path starts with a point light source focused on a single point within the specimen. For imaging, an objective lens is focused on the very same point, guiding the light to a detector. A pinhole is mounted in the optical path aligned with an image of the specimen. Thus, only light from the focal plane can pass through – light outside the focal plane is blocked. The image is generated by scanning the specimen and detecting the intensity spatially resolved for each pixel. It is sufficient to use the same objective lens for illumination and imaging. Then, an additional dichroic mirror is required to split the illuminating and imaging path (Figure III-18B).<sup>184</sup>

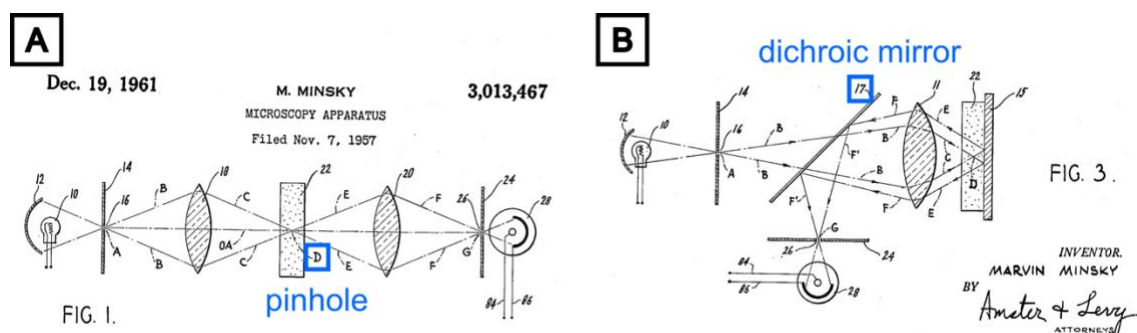


**Figure III-18.** Excerpts from the original patent of Marvin Minsky.<sup>184</sup> (A) Optical path of the confocal observation. From the left, only a confocal volume is illuminated (object D); on the right, only the confocal volume is observed. (B) Optical path for independent illumination and observation of a specimen utilizing a dichroic mirror (object 17).

The confocal principle is also beneficial for fluorescence microscopy techniques. Even if the exciting light is focused to one point in the specimen, the excitation cone is extended above and below the focal plane.<sup>185</sup> Fluorescence arising from this area out of focus can potentially blur the image. Similarly, it is blocked at the pinhole in a confocal setup.

Originally, the optical path was fixed, and the sample stage was scanned. Therefore, the optics needed to be optimized for imaging a single point solely, whereas in conventional microscopy the requirement for objective lenses is higher as they should be capable to capture the whole field of view in equal quality.<sup>186</sup> Soon, the advantages in combining scanning fluorescence microscopy with other scanning techniques, such as AFM, were exploited.<sup>187</sup> Up to now, stage scanning is still comparably slow owing to the high precision needed for translation. Further, the stage translation can raise difficulties when imaging delicate specimens or in liquid environment. For instance, in biological setups sample fixation might be unwanted, but the use of stage scanners can lead to sample movement during imaging.<sup>183</sup>

This limitation is overcome in the confocal laser scanning microscope (CLSM). It was developed by Åslund et al. in the 1980s.<sup>188</sup> For confocal setups, lasers are appealing as an illumination source because of their coherent monochromatic light and high intensity.<sup>183</sup> Scanning mirrors were integrated to the optical path.<sup>188</sup> This technique is still employed in commercially available CLSMs.<sup>189</sup> Besides mirror scanners, alternative techniques have been developed, as for instance, spinning-disk microscopes.<sup>190</sup> The key feature of spinning-disk microscopes is a disk with an arrangement of multiple pinholes that is used instead of a single pinhole. Upon disk-spinning, the imaged is generated with multiple pinholes in parallel. However, their higher imaging speed is at the cost of resolution and flexibility (fixed pinhole size).<sup>183</sup>

Ultimately, the optical resolution in confocal microscopy is limited by diffraction. Emitting fluorophores are point light sources, but the smallest feature that can be focused is of the size of an Airy disk, originating from the so-called point spread function. Therefore, the ultimate lateral resolution limit is given by the radius of the Airy disk  $r_{\text{Airy}}$  (equation (32)).<sup>183</sup>

$$r_{\text{Airy}} = 0.61 \frac{\lambda}{NA_{\text{obj}}} \quad (32)$$

The Airy radius depends on the wavelength  $\lambda$  of the point source as well as the numerical aperture  $NA_{\text{obj}}$  of the objective lens used for imaging. If the distance between two point sources is larger than the radius of the Airy disk, they can be resolved conceptually.

Practically, further optical effects are also deciding for the resolution limit, such as aberrations of the lenses used and the quality of the microscope alignment.<sup>183</sup>

Analog, the axial resolution is the minimum distance  $z_{\min}$  of two point sources along axial direction at which they are distinguishable as separate points (equation (33)).<sup>183,191</sup>

$$z_{\min} = \frac{2 \lambda \eta}{(NA_{\text{obj}})^2} \quad (33)$$

$\eta$  is the refractive index of the medium. The Airy disk and the axial resolution determine the confocal volume, but they are dependent on the wavelength. Thus, the confocal volume excited in the specimen differs from the confocal volume observed in fluorescence confocal microscopy. It can be visualized as an ellipsoid (Figure III-19).

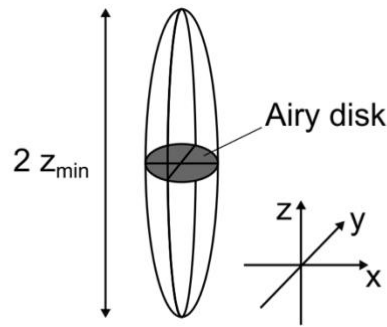


**Figure III-19.** Geometrical visualization of the confocal volume.

Although the confocal volume is usually larger owing to instrumentation, its maximum axial and lateral resolution is given in equation (34).<sup>183</sup>

$$\frac{z_{\min}}{r_{\text{Airy}}} = 3.28 \frac{\eta}{NA_{\text{obj}}} \quad (34)$$

Typical values for  $\eta/NA_{\text{obj}}$  are greater than one ( $\eta/NA_{\text{obj}} > 1$ ). It becomes apparent that physically the lateral resolution is higher than the axial resolution. As the pinhole plays an essential role for resolution, its size is usually in the order of the image of an Airy disk, corresponding to 1 Airy unit (AU). Resolution is lost when the pinhole is opened too wide.<sup>192</sup> Employed for blocking light, the pinhole limits the intensity of light inciding into

---

the detector, which is commonly a photomultiplier tube or a charge-coupled device (CCD).<sup>183</sup>

Aside from highly resolved fluorescence intensity images, spatially resolved spectral information can be advantageous particularly for systems with several fluorophores. In conventional and confocal fluorescence microscopy, the image is generated from the light intensity of the emission blocking stray light or the emission of other fluorophores by bandwidth filters. By integrating a diffraction grating between the pinhole and the detector, the incident light can be spectrally unmixed for detection.<sup>183,189</sup> The observed wavelength range is subdivided in spectral ranges so that intensity images of each spectral range are taken. In other words, emission spectra are recorded for each pixel. Displayed in the corresponding color of each spectral range, these images can be merged to a true color fluorescence image.

Moreover, this spectral detection allows imaging and distinguishing fluorophores with overlapping emission spectra. When fluorophores are detected in spectral bands over their fluorescence emission range, as conducted conventionally, emission overlaps with concurring fluorophores can lead to spectral bleeding. This can distort the actual image by multiple detection of the very same fluorophore intensity in various spectral bands - the fluorophores can “bleed” in other detection channels. By spectral unmixing, this artifact can be compensated owing to the higher spectral resolution in intensity.<sup>193</sup>

Accordingly, FRET can be visualized via spectral unmixing as the transfer leads to an increase in FRET acceptor emission and a decrease in FRET donor emission, shifting the detected fluorescence color. Alternatively, fluorescence lifetime imaging (FLIM) can serve to spatially resolve FRET as the transfer is an additional deactivation process, reducing the lifetime of the donor (see above, Section III.3.2).<sup>194</sup> In brief, the decay time of the intensity is determined for each pixel and plotted as an image of the local fluorescence lifetime. With the decay rate of fluorophores being sensitive to changes in environment, FLIM allows not only to monitor molecular interactions by FRET,<sup>195</sup> but also to spatially resolve analyte concentrations in cells, e.g. phosphate<sup>196</sup> or oxygen.<sup>197</sup>

In recent years, a groundbreaking increase in resolution below the diffraction limit has been achieved with advanced microscopy techniques.

The minimum size of the excitation volume in a confocal setup is determined by diffraction. Constraining this volume by stimulated emission depletion (STED), Stefan W. Hell and



coworkers managed to reduce the size of the resulting fluorescent spot below the diffraction limit.<sup>198</sup> Complementary, photoactivated localization microscopy (PALM)<sup>199</sup> utilizes fluorophores activated by illumination so that statistically a low number of molecules is fluorescing at a time. Their position is determined from the maxima of diffraction-limited fluorescence spots in the image.

As for recent novelties, an overwhelming development has been achieved in the field of confocal microscopy in the last decades. A deeper, more comprehensive view on many aspects can be found in literature.<sup>183,200-202</sup>

---

### III.4. Mechanoresponsive Materials

Having insights into polymer material properties and preparation, force measurements, and fluorescence effects, this chapter aims at combining these aspects to showcase materials suitable for mechanosensing and to understand the underlying principles for generating mechanoreponse at defined forces. The examples discussed here focus on optical responses, but mechanical stimuli can induce various changes.<sup>203</sup>

#### III.4.1. Peptide- and DNA-based Single Molecule Sensors

Growing interest in soft matter-based force sensing has emerged in the field of mechanobiology. Not only the mechanical influence of the cell environment on its behavior,<sup>7</sup> but also how cells exert forces on their environment has become a central topic. Therefore, concepts for mechanosensing materials were developed, focusing on biocompatibility not to influence cells' original behavior. Accordingly, many of these concepts are based on peptides or DNA.

In a study by Grashoff and coworkers,<sup>8</sup> the force-sensing molecule was based on the Vinculin protein present in the focal adhesion of cells. In between the Vinculin head and tail domains, a peptide sequence was inserted forming a polymeric entropic spring, terminated with a FRET donor and acceptor on respective ends (Figure III-20). Upon cell traction above a certain threshold force, the peptide entropic spring was elongated, signaled by a change in FRET. Thus, the mechanotransduction pathway along Vinculin could be proven. Moreover, the acting forces could be quantified by the FRET efficiency of the donor and acceptor at the termini of the entropic peptide spring, under the premise of calibrating the stretching forces separately.

Usually, such force calibration is performed with single molecule force spectroscopy, often based on AFM or optical tweezers. Recent reviews comprising this topic were published by Goktas and Blank,<sup>204</sup> and Grashoff and coworkers.<sup>205</sup> Briefly, the principle of single molecule force spectroscopy relies on attaching one end of the molecule to a substrate and the other end to a probe.

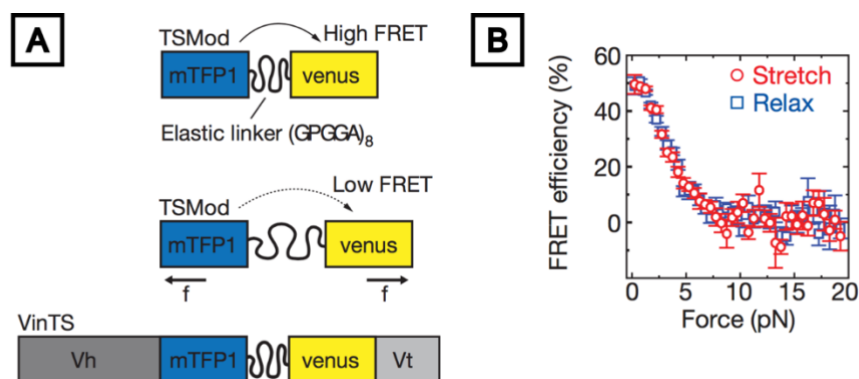


**Figure III-20.** (A) Vinculin modified with a tension-sensor module (TSMOD) for mechanosensing in the focal adhesion of cells. Integrated between the head (Vh) and tail (Vt) domain, TSMOD allows to read out the deformation state of the Vinculin tension sensor (VinTS) by FRET. (B) *Ex situ* force calibration of the TSMOD FRET response. Reprinted with permission and adapted from Grashoff et al.<sup>8</sup> Copyright Springer Nature 2010.

In case of AFM, the cantilever with the probe is approached to the substrate to allow coupling of the molecule to both sides (Figure III-21). Then, the cantilever is retracted to determine the force required to stretch the force-sensing molecule under simultaneous observation of its fluorescence and FRET. If optical tweezers are used, the procedure is similar, besides the probe is trapped and displaced optically. Therefore, the molecule to be stretched can also be attached to particles at both ends. More details to the optical tweezers technique can be found in literature.<sup>206,207</sup>

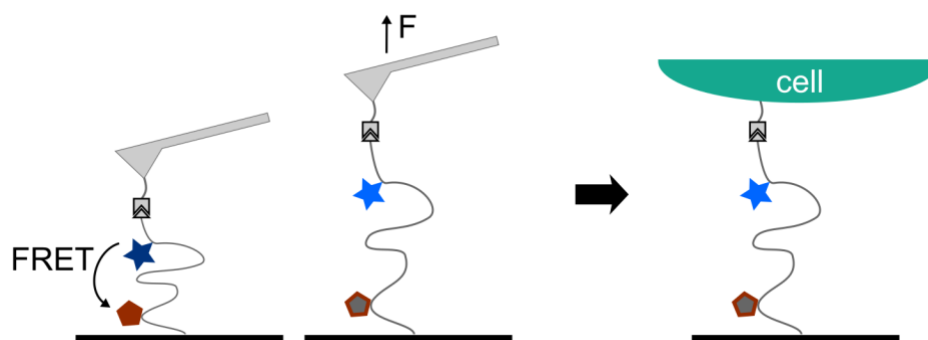


**Figure III-21.** Single Molecule Force Spectroscopy for calibration of molecular mechanosensors. In the example, the molecular force sensor is calibrated with AFM utilizing similar ligand interactions as cells (gray triangle and box). The deformation can be determined by a positioned FRET fluorophore pair (star and pentagon).

Such approaches to sense cell forces are often based on surface coatings: a protein or peptide ligand to interact with the cell, coupled to the surface with a PEG linker chain as entropic spring. With the ligand and the surface anchor being functionalized with a

fluorophore and a quencher,<sup>208-210</sup> or with a FRET pair,<sup>211</sup> fluorescence changes report stretching of the linker chain and the tension of the cell.

Similar concepts are based on DNA hairpins.<sup>167,212</sup> Hereby, the base sequence of DNA strands was constituted to form a hairpin. Upon tension, the DNA hairpin is unzipped. FRET or fluorophore/quencher pairs are coupled to the construct in such way that their distance is changed with unzipping to signal the tension. Alternatively, a DNA double strand can be employed as mechanosensitive element.<sup>213</sup> The tension required for the mechanoresponse can be adjusted by the number of DNA base pairs needed to unzip.

With DNA base sequence design, it is possible to control the folding of the structure, the so-called DNA origami. With this technique, Nickels et al.<sup>214</sup> constructed a DNA clamp with an entropic spring in between. The acting force was dependent on its length, as clamped chains exert higher entropic forces, the shorter they are. Moreover, they rendered the construct mechanosensitive by integrating a FRET pair in a so-called Holliday junction, achieving a self-reporting system that signaled the forces exerted by itself (Figure III-22).

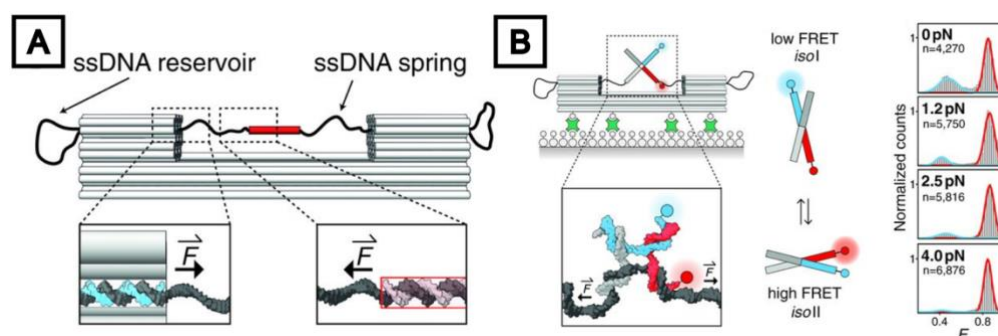


**Figure III-22.** (A) DNA-based clamp signaling the entropic forces exerted by the structure itself. (B) Integration of FRET-based force signaling by a Holliday junction. Reprinted with permission and adapted from Nickels et al.<sup>214</sup> Copyright AAAS 2016.

In protein-based systems, such concepts can further be utilized to elucidate mechanical functionality of proteins<sup>215</sup> or to monitor folding and aggregation processes of proteins.<sup>216</sup> The advantages of these strategies comprise a high specificity by using according ligands or functional proteins, and a high mechanical homogeneity. However, transfer to 3D applications or scale-up might bear challenges as these strategies are based on single molecules.

### III.4.2. Mechanochromic Materials

Mechanochromic materials are another class of materials with a mechanoresponsive effect. Usually, the effect is based on molecular units with conjugated  $\pi$ -electron systems in these materials. The underlying principle is a deformation-caused change in molecular structure. The structural change affects the conjugation state of the delocalized electrons and leads to a characteristic shift in fluorescence allowing to detect the molecular deformation.

The first report on the exploiting mechanochromism for sensing on the nanoscale is accredited to Carpick et al.,<sup>217</sup> but the material class was investigated much earlier already.<sup>218</sup> Carpick et al.<sup>217</sup> functionalized a surface by coating it with molecules containing acetylene functionalities. Upon shear stress applied with a sharp tip, the unsaturated acetylene units of the coating molecules were crosslinked irreversibly to a conjugated structure with delocalized electrons (Figure III-23). The resulting crosslinked structure revealed the contacted areas by local fluorescence.

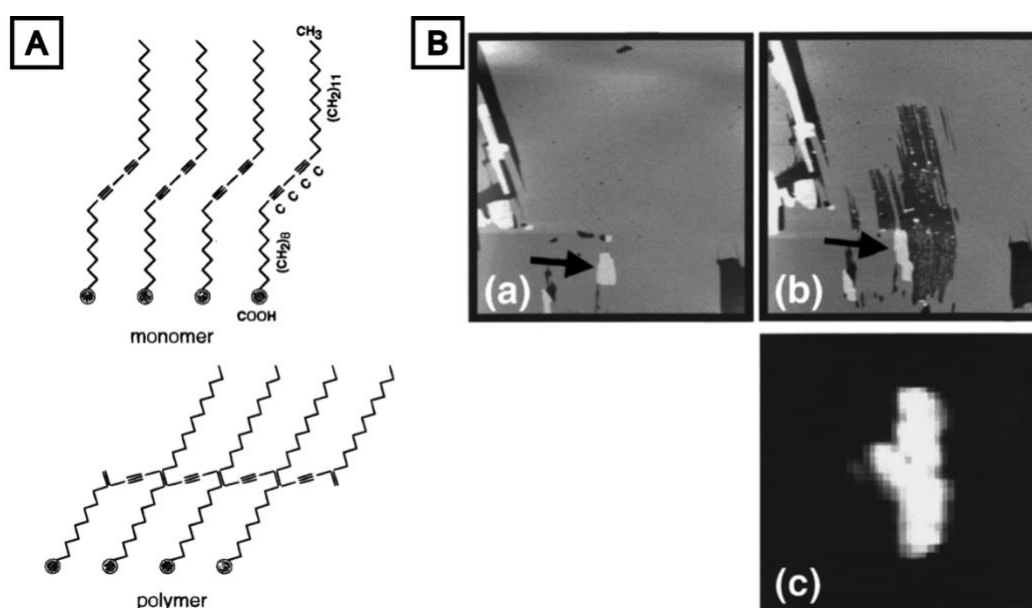


**Figure III-23.** (A) Mechanochromic surface coating signaling locally applied shear stress. Upon this stress, acetylene-units are crosslinked between the molecules causing localized fluorescence. (B) AFM scans in sizes of  $10 \times 10 \mu\text{m}^2$  depicting the initial image of a film (a) and the final image with a patterned region (b) formed by local high-load scans. (c) The fluorescence is visible in the patterned region. Reprinted with permission from Carpick et al.<sup>217</sup> Copyright American Chemical Society 2000.

In a comparable approach by Suhina et al.,<sup>219</sup> the surface coating comprised rigidochromic dyes. For this kind of dyes, excited states in solution are relaxed, e.g. via rotational modes, so that no fluorescence is observed. With such functionalities included in a surface coating,

mechanical compression of the coating with a polymer sphere could be read out by local fluorescence owing to locally hindered rotational relaxation. Suhina et al.<sup>219</sup> reported the contact signaled by fluorescence to be in accordance with the Hertz model.

Beyond fluorescently visualizing contact areas, various developments in mechanochromism are based on spiropyrans, for instance. When included in a polymer chain, tensile stress transduced along the chain can induce bond rupture in the spiropyran units, yielding the fluorescent merocyanine.<sup>220-222</sup> This mechanochromic shift allows to localize and quantify the stress, as demonstrated for rupture on the single molecule level.<sup>223</sup> Blending the mechanochromic polymers into a polymer matrix enables polymer-based stress reporting on the macroscale. Besides concepts with spiropyran units, also other mechanochromic functionalities are reported, such as dioxetanes,<sup>224</sup> cyclobutanes,<sup>225</sup> or anthracene derivatives.<sup>226</sup>

In case of polyaromatic chains, the mechanochromic effect does not originate from discrete functional units, but from the electronic configuration along the chain. Hence, conformational changes of the chain can be derived from their gradual change in fluorescence, allowing to monitor the deformation<sup>227</sup> (Figure III-24) with a force sensitivity down to the femtonewton range.<sup>180</sup>

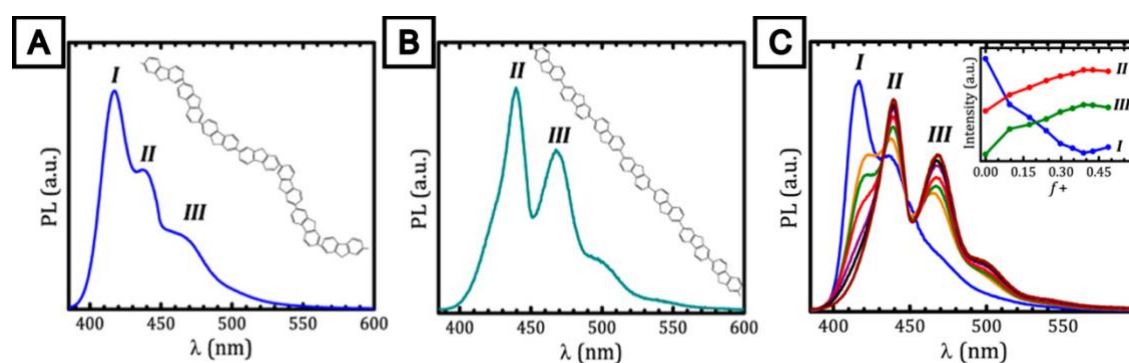


**Figure III-24.** Utilization of polyaromatic chains for mechanochromic conformation signaling. A pronounced difference in emission can be observed from kinked (A) to stretched (B) conformation, allowing the deduction of conformation in between (C). Reprinted with permission and adapted from Cingil et al.<sup>227</sup> Copyright American Chemical Society 2015.

Mechanochromic sensing concepts are available over a wide range of length scales. However, the mechanochromic functionalities need to be included to the polymer backbone so that the transduced force can trigger the mechanochromic shift. For microscopic force actors, such as cells, this requires not only preparational efforts in experimental design, but also functionalization for cell-specific interactions.

### III.4.3. Systemic and Structural Mechanoresponse

Whereas the mechanoresponse of the examples discussed above can be narrowed down to certain functionalities, examples are discussed in the following in which the response to mechanical triggers originates from the interplay within a system or a structure, as well as combinations of molecular, systemic, and structural responses.

Loading microcapsules with fluorophores, they can serve as a stress sensor releasing the fluorophore when the capsule is ruptured at a certain deformation.<sup>228</sup> Chemical reaction cascades are reported to signal the rupture of mechanically labile barriers<sup>229</sup> or labile bonds in hydrogel networks (Figure III-25).<sup>230</sup> Besides a delayed signaling owing to the reaction kinetics of the cascade, the signaling is irreversible. Though, these systems bear possibilities for scale-up.

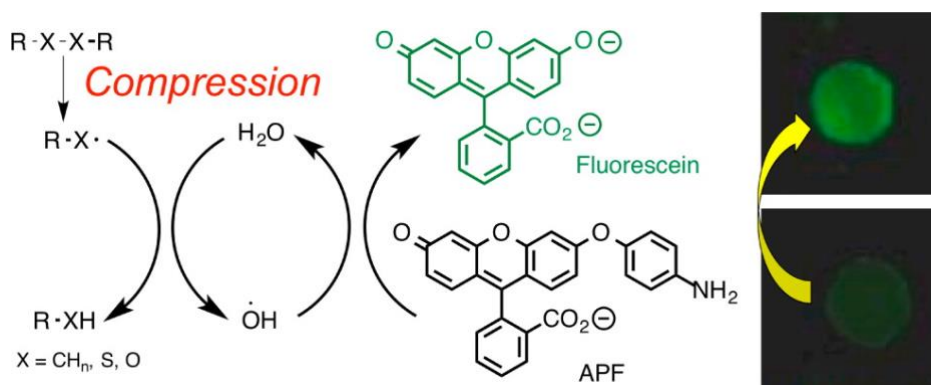


**Figure III-25.** Mechanolabile reaction cascade in hydrogels, releasing fluorescent dye upon mechanical trigger. Reprinted with permission from Fitch and Goodwin.<sup>230</sup> Copyright American Chemical Society 2014.

Upscaling is also achievable by utilizing a structural property for signaling mechanical stress. The interference of light incident into an ordered structure is sensitive to changes in the distances of spheres in photonic crystals,<sup>231</sup> intercalated layers,<sup>232</sup> or wrinkling patterns,<sup>233</sup> for example. The functionality of this effect has been demonstrated, employing hydrogels as matrices around ordered particles.<sup>234,235</sup> Also, synthetic fibers have been equipped with an ordered particle structure at their surface, changing their color upon stretching (Figure III-26).<sup>236</sup>

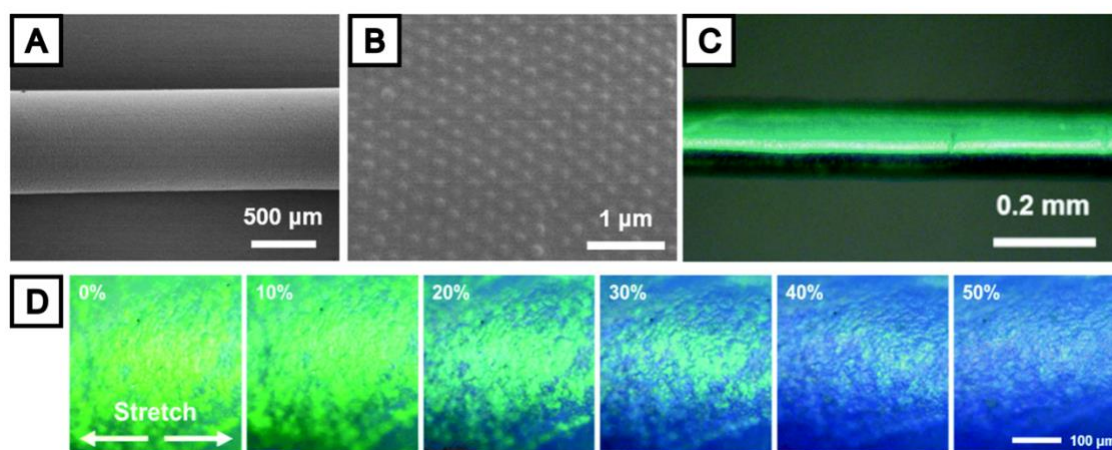


**Figure III-26.** Mechanochromic fibers functionalized with an ordered structure of microspheres. (A) Scanning electron microscopy image of the fibers with (B) close-up of the ordered structure. (C) Optical appearance of an exemplary fiber. (D) Changes in elongation are signaled by a color shift from an altered interference of the microsphere structure. Reprinted with permission and adapted from Zhang et al.<sup>236</sup> Copyright Royal Society of Chemistry 2016.

Apart from interference, other collective responses of ordered structures can also exhibit mechanoresponsive character, such as shifts of plasmonic modes<sup>237</sup> or fluorescence switching of coordinating atoms in hydrogel networks.<sup>238</sup> Although collective responses might be limited in terms of spatial resolution, their applicability in larger scale has been demonstrated.

Comparing molecular scale, systemic, and structural approaches, it seems beneficial to equip a scalable material platform with a molecular scale response mechanism.

In prior work by Bünsow et al.,<sup>9</sup> a mechanoresponsive polyelectrolyte brush has been demonstrated to be sensitive to stresses as low as 10 kPa with a spatial resolution of 1  $\mu\text{m}$ . This structure was utilized and applied within the scope of this thesis to elucidate the contact stress distributions of gecko-inspired adhesive microstructures (cf. Chapter IV). The cationic polyelectrolyte brush was polymerized *grafting from* the surface. A strong polyelectrolyte brush with permanent positive charges was generated, mainly constituting of the monomer [2-(methacryloyloxy)ethyl]trimethylammonium chloride (METAC). As a comonomer in a subordinate amount, aminoethyl methacrylate (AEMA) was used as functionality for successive labeling of 5(6)-carboxyfluorescein.

With the collapse of the brush structure, the fluorescence intensity was decreased. This is due to quenching of the fluorescein by the cationic charges of the quaternary ammonium groups, as observed similarly by Caruso et al.<sup>239</sup> Without time-resolved fluorescence measurements, the quenching mechanism cannot be revealed with certainty.<sup>163</sup>



However, fluorophore and quencher being attached to polymer chains might indicate static quenching by cationic complexation of the METAC units with fluorescein molecules rather than a dynamic quenching process (cf. Section III.3.1).

Stretching the polymers chains increased fluorescence intensity, indicating reduced quenching. Such conformational changes in the polyelectrolyte brush could be induced by mechanical stress applied with Soft Colloidal Probe AFM (SCP-AFM), and were detected with CLSM (Figure III-27).

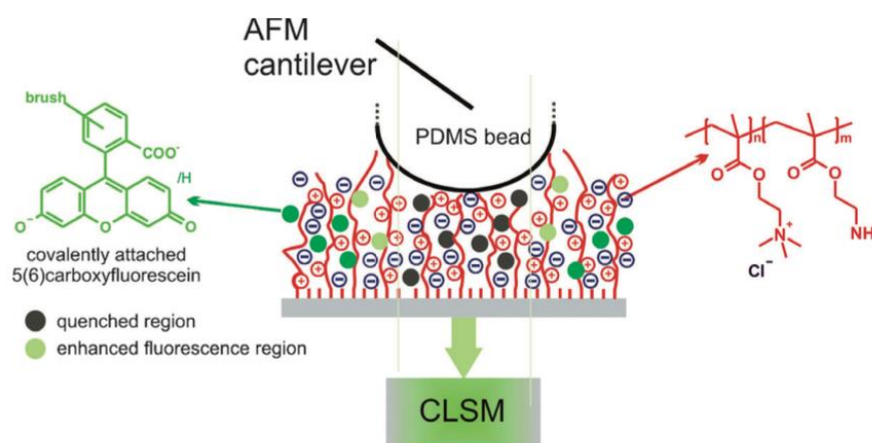


**Figure III-27.** Scheme of the mechanoresponsive polyelectrolyte brush compressed with SCP-AFM and observed with CLSM. Reprinted with permission from Bünsow et al.<sup>9</sup> Copyright WILEY 2011.

Utilizing SCP-AFM, the fluorescence response of the polyelectrolyte brush to defined stress was investigated. The local fluorescence intensity could be correlated to local stress: compressive stress in the central contact area of the SCP, causing an increase in quenching, and tensile stress from adhesion of the SCP at the edges of the contact area, causing a brighter rim from reduced quenching (Figure III-28A). With the JKR model (cf. Section III.2.3), the SCP contact mechanics<sup>151</sup> allowed to calculate the local pressure acting on the mechanoresponsive polyelectrolyte brush so that it could be compared to the local fluorescence intensity. For the compressive area, a quantitative relation between local pressure and local fluorescence was found to be independent of the load applied on the SCP (Figure III-28B). Although polyelectrolyte brushes are also responsive to changes in ionic strength (cf. Section III.1.2), similar behavior was found at various ionic strengths.<sup>9</sup>

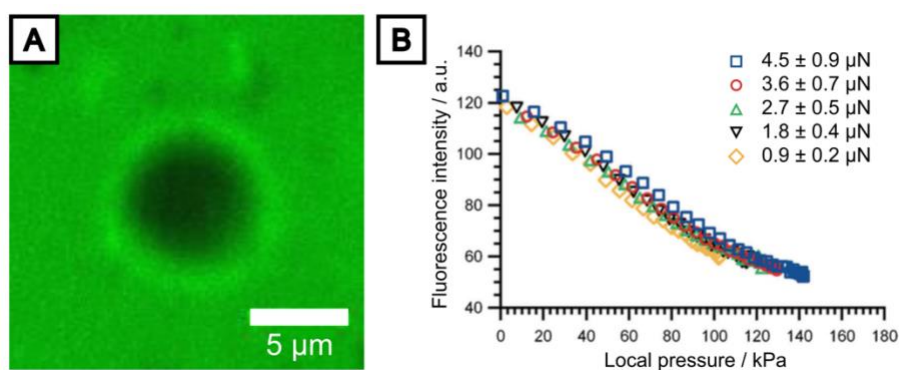


**Figure III-28.** (A) CLSM image of the mechanoresponsive polyelectrolyte brush with load applied by SCP-AFM. (B) Response curves of local fluorescence intensity to local pressure for given AFM loads. Reprinted with permission and adapted from Bünsow et al.<sup>9</sup> Copyright WILEY 2011.

Summarizing the capabilities of this mechanoresponsive polyelectrolyte brush, it is able to map compressive and tensile contact stresses qualitatively, and compressive stress even quantitatively.

Conceptually, such polymer brushes are surface coatings and, therefore, limited to two-dimensional geometry, so they offer mechanosensing abilities only in planar contact. Yet, three-dimensional structures, such as hydrogel networks, could serve as material platform to advance to the third dimension. Promising results have been reported on thermo- and pH-responsive microgels labeled with FRET pairs,<sup>114</sup> and DNA hydrogels with fluorophore-quencher pairs.<sup>240</sup>



---

# IV. Monitoring the Contact Stress Distribution of Gecko-Inspired Adhesives Using Mechanosensitive Surface Coatings

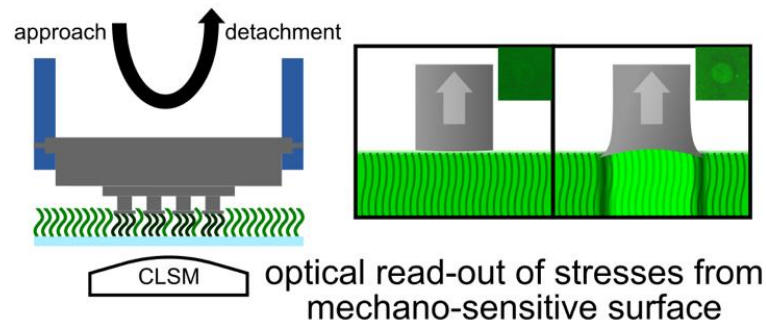
The following chapter in its entirety is based on the manuscript of the research article

“Monitoring the Contact Stress Distribution of Gecko-Inspired Adhesives Using Mechano-Sensitive Surface Coatings “

by Jens W. Neubauer, Longjian Xue, Johann Erath, Dirk-M. Drotlef, Aránzazu del Campo, and Andreas Fery. *ACS Appl. Mater. Interfaces* **2016**, 8 (28), 17870–17877.

It is reprinted with permission, whereas the copyright remains with the American Chemical Society 2016. The entire text as well as the published figures are reused, expanded by content of the Supporting Information, and adapted to be integrated into this thesis.

---



*The contact geometry of microstructured adhesive surfaces is of high relevance for adhesion enhancement. Theoretical considerations indicate that the stress distribution in the contact zone is crucial for the detachment mechanism, but direct experimental evidence had been missing so far. In this work, a method is presented that allows, for the first time, the detection of local stresses at the contact area of biomimetic adhesive microstructures during contact formation, compression and detachment. For this purpose, a mechanosensitive polymeric layer was used. It converts mechanical stresses into changes of fluorescence intensity. The biomimetic surface was brought into contact with this layer in a well-defined fashion, using a micro-contact printer, while the contact area was monitored with fluorescence microscopy in situ. Thus, changes in stress distribution across the contact area during compression and pull-off could be visualized with a lateral resolution of  $1\ \mu\text{m}$ . This method was applied to study the enhanced adhesive performance of T-shaped micropillars, compared to flat punch microstructures. Significant differences in the stress distribution of the both differing contact geometries were found during pull-off. In particular, the results are direct evidence for the suppression of crack nucleation at the edge of T-shaped pillars, which confirms theoretical models for the superior adhesive properties of these structures.*

---



## IV.1. Introduction to Bioinspired Adhesive Microstructures

Animals have evolved hierarchical structures to adhere on different kinds of smooth and rough surfaces.<sup>241,242</sup> Inspired by this performance, various artificial structures have been fabricated.<sup>243-253</sup> In recent years, generic mechanisms of these structures have been identified.

One important mechanism is the so-called contact splitting:<sup>241,254</sup> Rather than exhibiting a continuous adhesion area, the biological and biomimetic systems mentioned above typically show a large number of isolated contact zones. Thus, the contact can be adapted to the surface roughness. Further, the crack propagation is limited and, in order to fully detach, a crack must be nucleated at each individual contact zone.

Besides contact splitting, another essential feature for outstanding adhesion performance is the contact geometry of the contact zones. Different contact geometries exist in biological models, adapted to their environment and distinguished between dry adhesion<sup>255</sup> and wet adhesion.<sup>256-259</sup> Familiar examples for dry adhesion are fibrils terminated with a spatula-shaped geometry on gecko feet pads,<sup>260,261</sup> or with a thin annular plate on beetle feet and plants (T-shaped geometry).<sup>262</sup>

With lithography methods, fibrillar and pillar-based structures mimicking these geometries can be achieved.<sup>263-268</sup> Especially T-shaped pillars significantly outperform flat punches in adhesion.<sup>264,269,270</sup> For T-shaped pillars, overhangs are generated centrosymmetrically at the top of flat punch pillars.

To attain insight into their superior adhesion performance, the detachment mechanism of T-shaped pillars was investigated explicitly using different methods. Hossfeld et al.<sup>270</sup> performed peel-off experiments under varying angles. By optical tracking of the detachment, they could locate the crack nucleation, leading to detachment, at the center of the contact area. In conformity with their observations, finite element analysis predicted stress peaks at the same positions and low stress at the edges.

Varenberg and Gorb et al. utilized high-speed video recording to follow the nucleation and the propagation of cracks during pull-off normal to the contact area in air<sup>271,272</sup> and underwater.<sup>273</sup> They also located the crack nucleation at the center of the contact area of T-shapes, propagating toward the edges. For flat punch micropillars, the cracks propagated from the edges to the center. Additionally, the resulting detachment was faster for flat

---

punches. Further, they observed the same detachment mechanism for T-shapes underwater, although the pull-off force was lower.

Paretkar et al. used *in situ* scanning electron microscopy to take a more global view on the detachment of flat punch and T-shaped pillars.<sup>274</sup> They attributed the advantage in adhesion to the stochastic effect of more T-shaped pillars than flat punches remaining attached at the same elongation during retraction. Thus, the study showed the macroscopic effect of the different detachment mechanisms. Despite detailed investigation of the detachment mechanism, a direct measurement of the contact stresses during detachment has been missing so far.

In theoretical approaches, the stress distribution at the contact area of flat punch and T-shaped pillars was investigated in numerous studies.<sup>275-282</sup> For flat punch micropillars, stress singularities at the edges were predicted. In contrast, the stress distribution of T-shaped pillars was predicted to be minimal at the edges and tension to be concentrated at the center. These differences in the stress distributions were expected to be the cause of the respective detachment mechanisms, but had not been determined experimentally yet.

## IV.2. Resolving Contact Stresses with Mechanoresponsive Polymer Brushes

In this study, the experimental observations of the detachment already gained were linked to the predictions made by theory. Mechanoresponsive surfaces<sup>9,47</sup> were used to sense the contact stress distributions of biomimetic micropillar structures with flat punch and T-shape geometry. This novel type of mechanosensitive polymeric layer was recently reported for being able to resolve local stresses on the micrometer scale.<sup>9</sup> The mechanosensitive surface coating is a polyelectrolyte brush labeled with a fluorescent dye. The dye can be quenched by charges of the polyelectrolyte brush so that conformational changes affect the fluorescence intensity. With the soft colloidal probe technique,<sup>151</sup> it could be demonstrated that the fluorescence of the polyelectrolyte brush is sensitive to mechanical triggers. Compressive and tensile stress increase and decrease quenching, respectively. It can be localized and distinguished with high spatial resolution (1  $\mu\text{m}$ ) using confocal laser scanning microscopy (CLSM) for fluorescence read-out (Figure IV-1). This unique approach allowed to map the local stresses under micropillars during detachment. The contact, approach, and detachment of the micropillar structures was controlled with a micro-contact printing setup. In this respect, the preparation methods of micro-contact printing stamps and micropillar structures had to be adapted and combined.

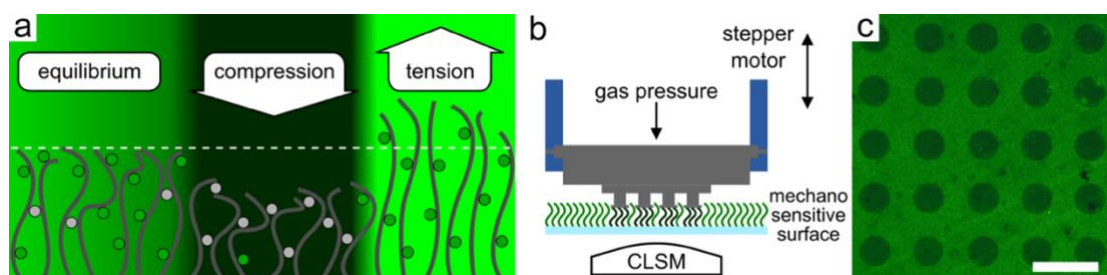


**Figure IV-1.** (A) Scheme of the polyelectrolyte brush response mechanism to mechanical triggers. In water, the equilibrium conformation of the polyelectrolyte brush is predominantly stretched normal to the surface. Here, most of the dye molecules attached to the polyelectrolyte brush are fluorescing (green dots). Quenching of the dye molecules can occur by cationic complexation in the polyelectrolyte chains (light gray dots) upon compression. On the contrary, further stretching of the chains owing to external tension reduces quenching. (B) Schematic alignment of the micro-contact printing stamps and the mechanosensitive surface on a confocal laser scanning microscope (CLSM). An overpressure can be applied in the stamp to bulge and compensate concavity. Moved by a stepper motor, the micropillars on the stamp are brought in contact with the mechanosensitive surface. The pillars compress the brush structure so that the resulting quenching can be locally resolved with the CLSM. (C) CLSM image of the mechanosensitive polymer surface locally quenched by the approached T-shaped pillars. The scale bar depicts 50  $\mu\text{m}$ . Reprinted with permission from Neubauer et al.<sup>10</sup> Copyright American Chemical Society 2016.

---

### IV.3. Combination of Microcontact Printing and Confocal Microscopy

#### *Adaption of Micropillar Structure Preparation*

Arrays of flat punch and T-shaped micropillars can be produced according to the approaches published in earlier work.<sup>264,269</sup> Flat punch micropillars were generated with soft lithography: A negative of the micropillar structure was generated with photolithography. It was used to mold the flat punch micropillars as positive structure with polydimethylsiloxane (PDMS), an elastomer. As common, PDMS was casted as a formulation of precursor and curing agent, and crosslinked at elevated temperature (65 – 90 °C).

T-shaped micropillars were based on flat punch micropillars. For creating annular overhangs, a layer of micrometer thickness was created by doctor blading from a PDMS formulation left at room temperature for several hours. Flat punch micropillars were inked in this PDMS formulation layer. The curing of the inked flat punches was completed in contact with a plane surface at elevated temperature. T-shape overhangs resulted from crosslinking the inked PDMS.

For the micro-contact printing setup used in the experiments, microstructured stamps could be created. They were casted into stamp blanks custom-made for the setup. The stamp blanks were chucked in a molding station so that a cavity for the stamp structure remained. Usually, a negative of the desired structure is placed at the bottom of the cavity for molding. Then, PDMS is injected into the stamp cavity and cured at elevated temperature. When demolding the stamp from the cavity, it exhibits a concave shape owing to thermal shrinkage. Whereas this could be compensated in the printing setup with an overpressure bulging the stamp, the concave shape of the stamp would be present during handling and further preparation steps.

As a consequence, it would have been feasible to directly fabricate stamps with flat punch pillar microstructures using an according negative structure. However, the modification to create overhangs requires plane and even contact of the flat punch structure which was hardly possible without bulging pressure. Therefore, the preparation process was adapted to achieve stamps with T-shaped pillar microstructures. Combining both preparation methods (Figure IV-2), flat punch and T-shaped pillar structures were generated following

the conventional procedure. Either of both structures were glued to unpatterned, flat micro-printing stamps using a minimal amount of PDMS in a final curing step.

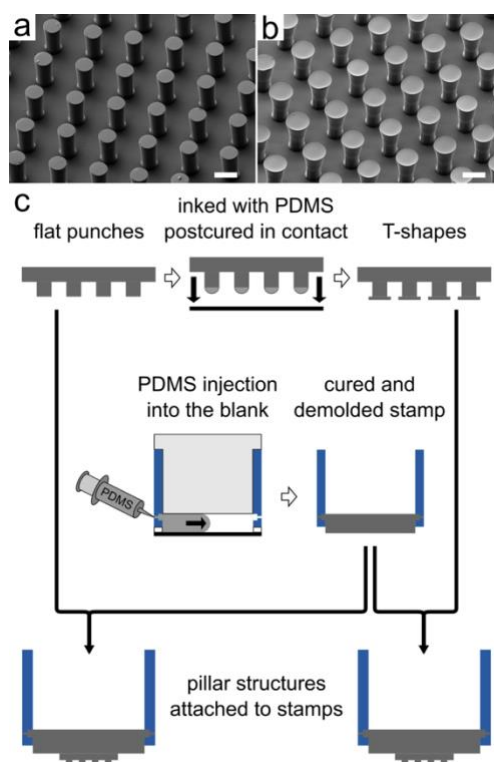


**Figure IV-2.** (A) SEM micrograph of flat punch micropillars. (B) SEM micrograph of T-shaped micropillars. The scale bars represent 20 μm for both micrographs. (C) Fabrication scheme of the micro-contact printing stamps. The flat punch micropillar patterns were produced in a double soft molding procedure. Optionally, the flat punches were inked in a thin film of precured PDMS and postcured in contact to create T-shaped pillars. For featureless flat micro-contact printing stamps, PDMS was casted into the blue custom-made stamp blanks, using an unpatterned silicon master. After curing and demolding, flat punch or T-shaped pillar structures were attached to the stamp. Reprinted with permission from Neubauer et al.<sup>10</sup> Copyright American Chemical Society 2016.

---

## *Contact Formation of Micropillars on Mechanoresponsive Polyelectrolyte Brushes*

To determine the contact stress distributions of flat punch and T-shaped micropillars, they were brought in contact with a force sensing surface. It consisted of a mechanoresponsive polyelectrolyte brush resolving stress distributions at the micrometer scale.<sup>9</sup> This mechanosensitive coating was polymerized from the surface and labeled with a fluorescent dye (5(6)-carboxyfluorescein). Its responsiveness to compressive and tensile stress has been demonstrated before elsewhere.<sup>9,151</sup>

Owing to solvent interactions, the equilibrium conformation of the polyelectrolyte brush is predominantly stretched normal to the surface in aqueous media (cf. Section III.1.2). The polyelectrolyte brush is only responsive in aqueous media because it is collapsed in dried state and in non-solvents. The brush thickness was determined with atomic force microscopy force-distance measurements to be on the order of 100 – 150 nm.<sup>283</sup> The charges of the polyelectrolyte can quench the fluorescence of the dye so that most of the dye molecules are fluorescing in equilibrium conformation. Compression leads to an increase in quenching, resulting in lower fluorescence intensity. On the contrary, tension further stretches the chains and decreases the quenching, generating a higher fluorescence intensity.<sup>9</sup> Accordingly, compressive and tensile stresses can be distinguished from the local fluorescence intensity and read out optically with the high spatial resolution of confocal laser scanning microscopy (CLSM).

Mounting the micro-contact printing setup to a CLSM, the fluorescence response of the mechanosensitive surface could be monitored *in situ* during approach and retraction of the microstructures (Figure IV-3). Thus, the local stresses during contact and detachment could be deduced from spatially resolved fluorescence.

Prior to the approach to the mechanosensitive surface, the micro-contact printing stamps carrying the structures were bulged with a gas pressure to compensate their slightly concave shape mentioned above. To avoid air entrapments while moving downwards,<sup>284</sup> the stamps were immersed carefully in the water that was wetting the polyelectrolyte brush.

After equilibrating, the stamp was further moved toward the surface with the stepper motor until contact formation at the surface could be observed in the CLSM. Imaging the

fluorescing mechanosensitive surface, dark spots of the size of the pillars indicated local quenching from the compressive stress of the pillars.

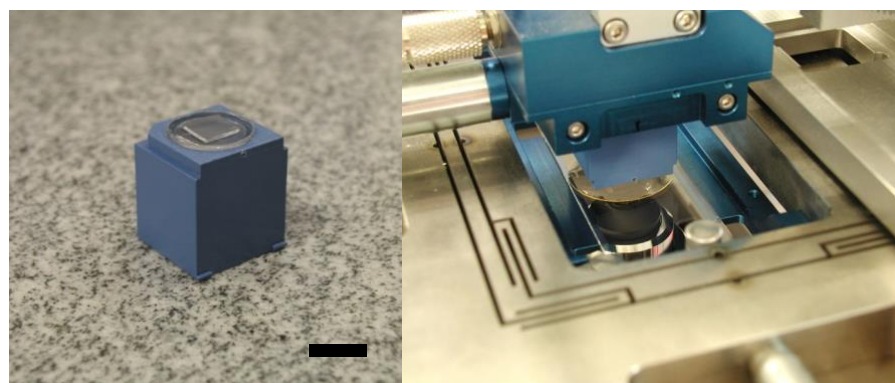


**Figure IV-3.** Photographs of a micropillar array structure attached to a micro-contact printing stamp (left, flipped upside-down, scale bar 1 cm), and of the setup (right). The micro-contact printer is placed on the microscope stage. A stamp with pillar structures is mounted in the micro-contact printing device. Immersed in water, the stresses acting on the mechanosensitive surface on the cover slip can be read out with the confocal laser scanning microscope in bottom-view. The cover slip is fixed on a glass slide with a droplet of water. Reprinted with permission from Neubauer et al.<sup>10</sup> Copyright American Chemical Society 2016.

---

## IV.4. Determination of Contact Stress Distribution for Adhesive Microstructures

### *Flat Punch Pillars*

In a typical experiment, the micropillars were moved against the mechanosensitive surface with the stepper motor and retracted. CLSM images were taken in between the motor steps. An animation of the CLSM images is available in the Supporting Information of the publication.<sup>10</sup> (Figure IV-4).

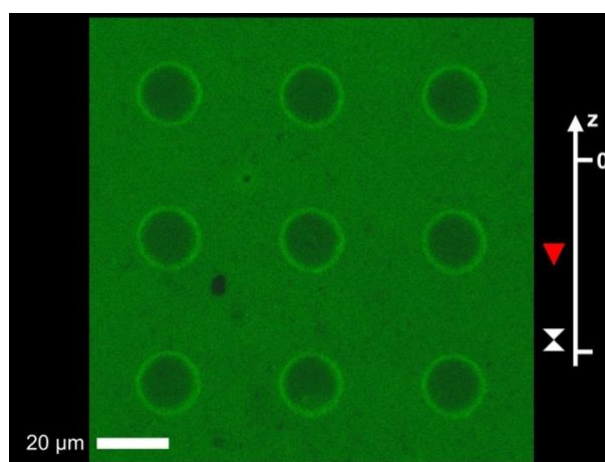


**Figure IV-4.** Image from an animation of CLSM images during a typical approach-retrace experiment of flat punches. It is available in the Supporting Information of the publication.<sup>10</sup> The z-scale on the right is relative to the minimum motor position and the position before the first fluorescence change was observable. The arrow direction corresponds to approach and retrace. The CLSM images were taken in between the motor steps. Transient effects appeared temporarily when the micropillar structure and the polyelectrolyte brush came into contact. They were not existent in force equilibrium when compression or tension acted on the polyelectrolyte brush. Reprinted with permission from Neubauer et al.<sup>10</sup> Copyright American Chemical Society 2016.

For a detailed understanding of the detachment mechanism of the micropillars, images of individual pillars were taken into closer investigation. On a flat punch pillar, the fluorescence response at different steps during approach and retraction was investigated by azimuthally averaging the fluorescence intensity in the contact area (Figure IV-5). For comparison, the fluorescence intensity was normalized to the equilibrium intensity of the mechanosensitive surface outside of the contact area, which served as an internal reference. In Figure IV-5, CLSM images during stages of approach (images 1-3, reddish colors) and retraction (images 5-7, bluish colors) are shown. At the minimum of the approach-retraction-cycle (Figure IV-5, image 4), the azimuthally averaged intensity profile is depicted in black. The corresponding z-position of the stepper motor is depicted below the



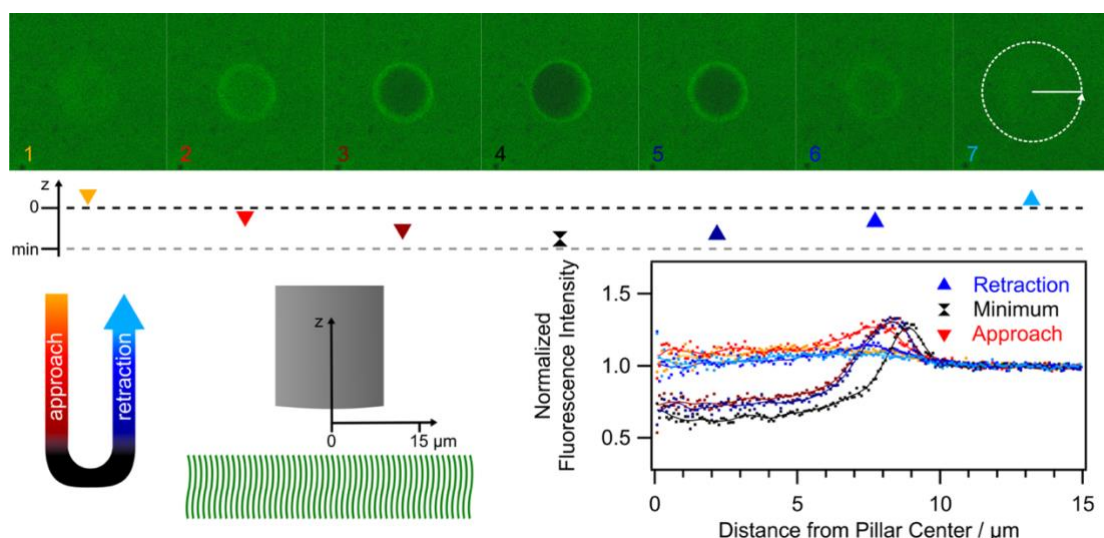


**Figure IV-5. Top:** CLSM images of an individual flat punch pillar during approach (images 1-3), at the minimum (image 4), and during retraction (images 5-7). Below, the z-position is plotted relatively to the minimum position and the position of the first noticeable change of fluorescence. The fluorescence intensity was averaged azimuthally, as implied in image 7 (radius 15  $\mu\text{m}$ ), and plotted on the **bottom right**. For normalization, the fluorescence intensity was related to the equilibrium intensity outside of the contact area. Lines were added to guide the eye. In direct comparison, lower intensity could be related to local compression, and higher intensity to local tension, respectively. **Bottom left:** Scheme of the orientation of the depicted quantities. The color code of approach and retraction corresponds to the image numbers, the symbols on the z-scale, and the radial fluorescence intensity profiles. Reprinted with permission from Neubauer et al.<sup>10</sup> Copyright American Chemical Society 2016.

CLSM images. It was scaled relatively to the starting and the minimum position of the stepper motor. The starting position was defined at the motor step before the first noticeable change of fluorescence. The z-position was scaled relatively because the absolute movement did not correspond to the deformation of the mechanosensitive surface-coating, the overall deformation scenario is more complex: the z-stepper movement is transferred into the deformation of the polymeric surface, the deformation of the pillars, the deformation of the bulged support and the Laplace pressure from the wetting of the micropillar structures<sup>285,286</sup> so that the deformation of the surface or the pillars could not be quantified precisely. The equilibrium fluorescence outside the contact area is not changed, proving that the responsiveness of the polyelectrolyte brush was not affected by this wetting phenomenon.

Comparing approach and retraction, similar stress distributions were observed at equal z-positions. During approach, compressive stress built up over the whole contact area, apparent from the decreasing fluorescence intensity. The fluorescence quenching ceased during retraction. The radial intensity profiles support this observation (Figure IV-5, bottom right). The profiles at equal z-positions coincide, besides slight differences between the

light red (Figure IV-5, image 2) and the middle blue intensity profile (Figure IV-5, image 6). It has to be noted that the bright rim at the edges of the pillar might not be due to local tensile stresses, as it already appeared during approach. It might have been an effect of scattering of the excitation laser at the edges of the flat punch pillar. The locally higher excitation intensity would have resulted in a locally increased fluorescence intensity. Optical reflective microscopy images with dark-field condenser confirm the higher scattering intensity at the edges of flat punches (Figure IV-6).

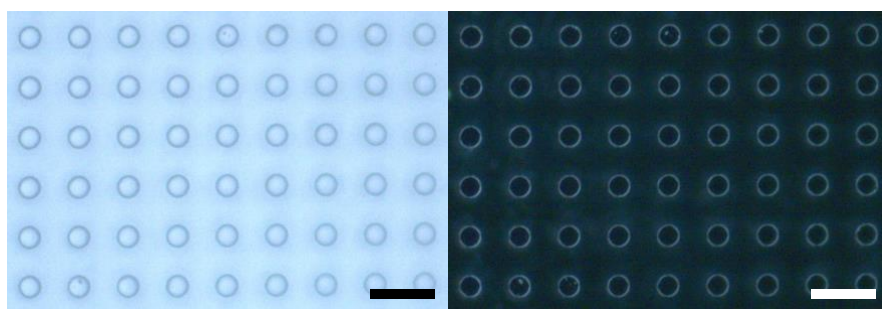


**Figure IV-6.** Optical reflective microscopy images of flat punch micropillars under illumination with bright-field condenser (left) and with dark-field condenser (right) in air. Enhanced scattering intensity could be located at the pillar edges. The scale bars depict 50  $\mu\text{m}$ . Reprinted with permission from Neubauer et al.<sup>10</sup> Copyright American Chemical Society 2016.

### *T-shaped Pillars*

The contact formation and detachment of T-shaped micropillars was investigated in analogous experiments. The according animation is available in the Supporting Information of the publication.<sup>10</sup> (Figure IV-7).

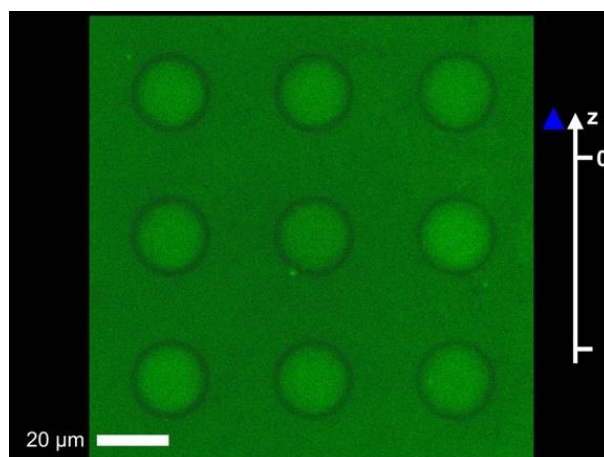


**Figure IV-7.** Image from an animation of two typical approach-retrace experiments of T-shaped micropillars on different spots. It is available in the Supporting Information of the publication.<sup>10</sup> The z-scale on the right is relative to the minimum motor position and the position before the first

fluorescence change was observable. The arrow direction corresponds to approach and retrace. The CLSM images were taken in between the motor steps. Transient effects appeared temporarily when the micropillar structure and the polyelectrolyte brush came into contact and after detachment. They were not existent in force equilibrium when compression or tension acted on the polyelectrolyte brush. Reprinted with permission from Neubauer et al.<sup>10</sup> Copyright American Chemical Society 2016.

The fluorescence response during approach and retraction of T-shaped pillars is presented in Figure IV-8, similar to the results of the flat punch pillars (Figure IV-5)

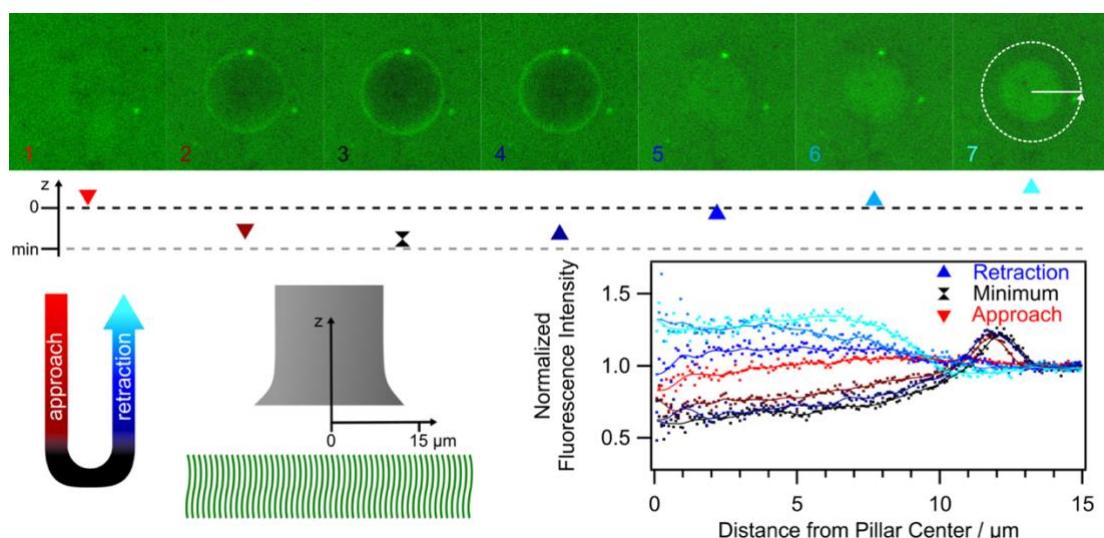


**Figure IV-8.** **Top:** CLSM images of an individual T-shaped pillar during approach (images 1+2), at the minimum (image 3), and during retraction (images 4-7). Below, the z-position is plotted relatively to the minimum position and the position of the first noticeable change of fluorescence. The fluorescence intensity was averaged azimuthally, as implied in image 7, and plotted on the **bottom right**. For normalization, the fluorescence intensity was related to the equilibrium intensity outside of the contact area. Lines were added to guide the eye. In direct comparison, lower intensity could be related to local compression, and higher intensity to local tension, respectively. **Bottom left:** Scheme of the orientation of the depicted quantities. The color code of approach and retraction corresponds to the image numbers, the symbols on the z-scale, and the radial fluorescence intensity profiles. Reprinted with permission from Neubauer et al.<sup>10</sup> Copyright American Chemical Society 2016.

During approach to minimum (Figure IV-8, images 1-3, reddish and black), T-shaped pillars did not differ from flat punches qualitatively. Upon retraction (Figure IV-8, images 4-7, bluish colors), an obvious difference could be perceived in the stress distribution.

Retracting below the starting z-position (Figure IV-8, images 4+5), the quenching diminished. At the starting z-position (Figure IV-8, image 6), the fluorescence at the center of the contact area was slightly increased. When the pillars were retracted above the starting z-position (Figure IV-8, image 7), the fluorescence in the central contact area increased

further. In addition, quenching at the edges appeared. Before the adhesion broke up spontaneously, the contact area contracted slightly.

In the case of the T-shaped pillars, the increased fluorescence in the center (Figure IV-8, images 6+7) directly relates to local tensile stresses during detachment. It did not appear during approach. However, in some cases, also fluorescence rims at the edges appeared (Figure IV-8, images 2-4). They might be caused by the same edge scattering effect as for the flat punches (Figure IV-9).

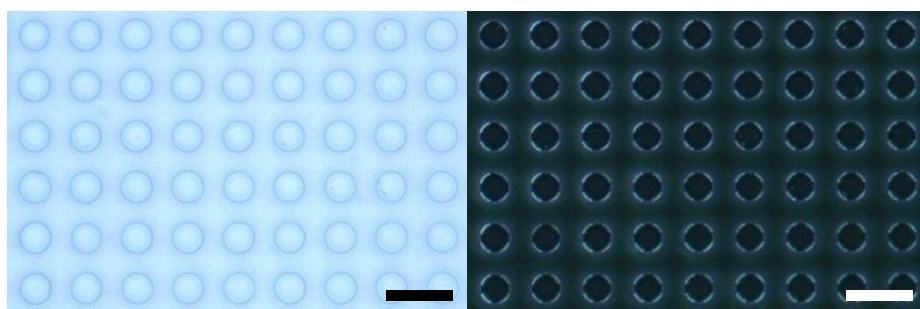


**Figure IV-9.** Optical reflective microscopy images of T-shaped micropillars under illumination with bright-field condenser (left) and with dark-field condenser (right) in air. Enhanced scattering intensity could be located at the overhangs. The scale bar depicts 50  $\mu\text{m}$ . Reprinted with permission from Neubauer et al.<sup>10</sup> Copyright American Chemical Society 2016.

### *Comparison of Detachment Mechanisms of Flat Punch and T-shaped Pillars*

To gather insight into the detachment mechanisms of flat punch and T-shaped pillars, the compressive and tensile areas were deduced from the local fluorescence intensity. For direct comparison, the detachment from the mechanosensitive surface is sketched schematically for both pillar geometries (Figure IV-10).

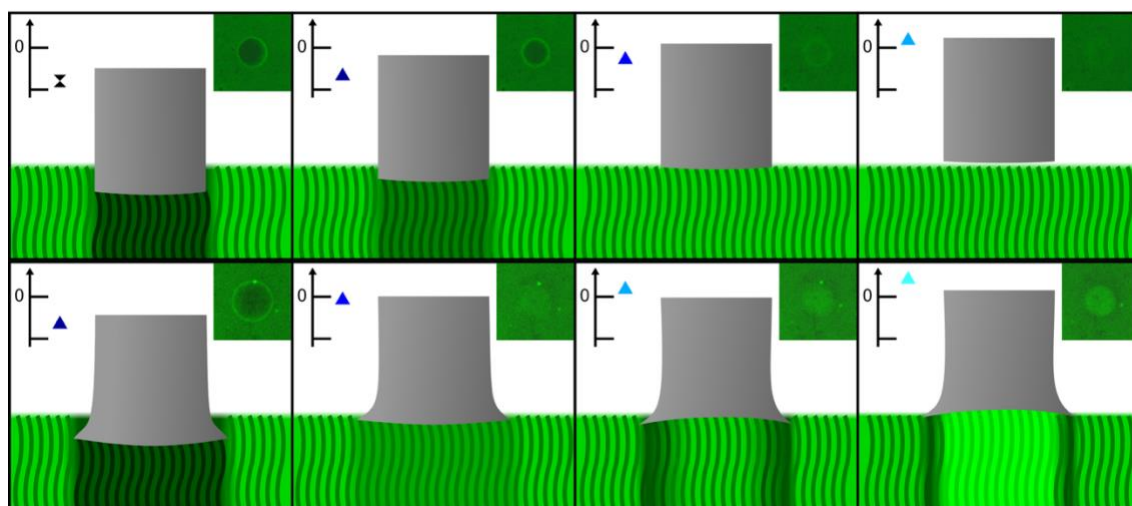


**Figure IV-10.** Schematic interpretation of the observed fluorescence response of the mechanosensitive surface during the retraction of the pillars. From the left to the right, stages of retraction are depicted for flat punch (top) and T-shaped pillars (bottom). The corresponding inset CLSM images and z-scales are adapted from Figure IV-5 and Figure IV-8, respectively. In the depiction, the size of the pillars (approx. 20  $\mu\text{m}$  in height) and the thickness of the mechanosensitive surface (approx. 150 nm) are not to scale. Reprinted with permission from Neubauer et al.<sup>10</sup> Copyright American Chemical Society 2016.

The flat punch pillars do not feature an adhesion break-up, but rather a gradual removal from the mechanosensitive surface. Fading compressive stresses could be assigned to the whole contact area during retraction up to the starting z-position where no mechanical interactions could be recognized anymore.

Several groups calculated the stresses acting during the detachment of flat punches.<sup>275,276,278,280,282</sup> The calculated stress was found to be minimal at the central region of the pillar. Hence, adhesion failure was attributed to stress singularities at the edges, allowing detachment cracks to propagate to the center. This is more pronounced for rounded edges.<sup>281</sup>

In the results shown above, the flat punch pillars were detached from the mechanosensitive surface with a fluorescent rim. This effect can be attributed to a local fluorescence increase from back-scattering. With the adhesion strength being lower in water,<sup>287</sup> the acting tensile stresses might have been masked by the fluorescence increase from scattering.



---

Nevertheless, the deduced detachment mechanism is in good agreement with the aforementioned literature. Although the scattering and tensile stress contributions to the fluorescence increase at the very edges cannot be distinguished clearly, the compressive stress decreases over the whole contact area from the center toward the edges. In addition, the rupture event is too fast for CLSM. With high-speed video recording, Heepe et al. determined the crack propagation speed to the order of magnitude of 1 m/s for flat punch pillars.<sup>272</sup>

During the retraction of the T-shaped pillars, a comparable gradual decrease in compression as for the flat punches could be determined. However, at the original starting position, the annular overhangs seemed to bend toward the mechanosensitive surface. This was apparent from the acting compressive stresses at the edges of the contact area. When the pillars were further retracted above the original starting point, the behavior during pull-off was recognized. As the tension increased in the center, the compression increased at the edges. Moreover, the contact area was contracted slightly until the pillar was detached spontaneously.

For modeling of T-shapes, their geometry was simplified to be a flat punch with a plate-like cap.<sup>276,280,282</sup> Above a certain plate thickness, the pillars behave like larger flat punches. For thin plates, the stress is minimal at the edges of the plate, but stress peaks appear in the region of the pillar diameter. In between the limiting cases, an almost uniform tension is prominent in the central contact area, decreasing toward the edges.<sup>276</sup> As a consequence, the adhesion failure usually does not originate from the edges, but from the center of the contact area.<sup>272</sup>

Modeling the pull-off of T-shapes with an annular wedge-like geometry, Aksak et al. further elucidated the detachment mechanism by varying the wedge angle and the ratio of cap-to-pillar.<sup>279</sup> At steep wedge angles and low cap-to-pillar ratios, singularities appear at the edges, similar to flat punches. By decreasing the wedge angle, the stress at the edges can be reduced.

Although the T-shapes in this study resembled a bell-like shape and might not be compared directly with either of the presented models, the main features of the theoretical predictions were identified in the measured stress distributions. Essentially, the tensile stress is concentrated uniformly to the center, and decreases toward the edges.

For the investigated T-shaped pillars, the overhangs are expected to be deformed further during approach and detachment. When retracted, the tensile stress in the central region forces the overhangs to bend down for preserving the contact. This effect intensifies when

the T-shaped pillars are pulled off the surface. It can be deduced from the increasing tensile stresses in the center and stronger compression at the edges of the contact area of the pillars. As a result, the contact area contracts permanently until the pillar is detached from the surface. Such suction-cup-like bending has been observed before.<sup>262,271,273,288</sup>

Summarizing, these results indicate that the main reason for T-shapes excelling flat punches in adhesion is the suppression of crack formation at the edges of T-shapes. The tensile stresses are concentrated to the center of the contact area, as predicted by theory.

---

## IV.5. Conclusions

The contact stress distributions of bioinspired flat punch and T-shaped pillar microstructures were determined with a polymeric mechanosensitive surface. Utilizing a micro-contact printer, they were approached and retracted normal to the surface. In contact with the surface, increasing compressive stresses over the whole contact area were monitored during approach. Up to the position of contact formation, the compressive stresses decreased again. For flat punch pillars, theory predicts stress singularities at the edges causing cracks to propagate toward the center. However, tensile mechanical interactions could not be determined undoubtedly. Either the acting tensile stresses were below the sensitivity of the polymeric surface, or the adhesion of the flat punches was too low. On the contrary, tensile stress is expected to be minimal at the edges of T-shaped pillars. Indeed, tensile stresses acting in the central contact area were observed during pull-off. Simultaneously, compressive stresses appeared at the edges of the contact area owing to the overhangs bending toward the surface. With the tension increasing in the center, the compression increased at the edges. Additionally, the contact area contracted during pull-off, supporting the depiction of a suction cup-like bending of the overhangs. Consequently, the detachment of the pillars is forced to develop from the center toward the edges. Hence, the adhesion failure originating from the edges is suppressed.

As further perspectives, the presented approach to determine the stress distributions during pull-off might be a powerful tool in further development of biomimetic adhesive microstructures. This technique is valuable in particular for the design of wet adhesion systems. Beyond the specific case of biomimetic adhesion, mechanosensitive surfaces as presented here might be of interest for clarifying adhesion of soft matter in water, as for instance, hydrogels on polyelectrolyte brushes.<sup>289-291</sup>



## IV.6. Experimental Section

### *Preparation of Biomimetic Micropillar Structures*

Silicon wafers (100 orientation) were purchased from Crystec (Berlin, Germany). SU-8 photoresist 2025 and the developer mr-Dev 600 were purchased from Micro Resist Technology (Berlin, Germany). 1H,1H,2H,2H-Perfluorodecyltrichlorosilane (96%) was purchased from Alfa Aesar (Karlsruhe, Germany). PDMS elastomer kits (Sylgard 184) were purchased from Dow Corning (Midland, MI, USA). Masks for lithography were custom-made by ML&C (Jena, Germany).

Thin PDMS precursor films were prepared with a Multicator 411 film applicator (Erichsen, Hemer, Germany). For surface activation, a PlasmaActivate MiniFlecto plasma chamber was used (Plasma Technology, Rottenburg, Germany).

The micro-contact stamps were casted in the custom-made molding stations shipped with the device ( $\mu$ CP-PVM-A from GeSiM, Großberkmannsdorf, Germany).

Detailed information about the preparation of flat punch and T-shaped micropillar structures can be found in previous publications.<sup>264,269</sup> By photolithographic processing of SU-8, 8x8 mm<sup>2</sup> cubic patterns of micropillars were generated on silicon wafers. The height, the diameter and the spacing of the pillars was 20  $\mu$ m. To prepare for soft lithography, the silicon masters were perfluorosilanized. A negative of the photolithographic micropillar patterns was cast from polydimethylsiloxane (PDMS) to produce a soft mold. PDMS was mixed in a 10:1 ratio of prepolymer/crosslinker, degassed for 30 minutes, poured onto the SU-8 pattern and cured at 90 °C for one hour. Before its use as a mold, the negative PDMS replica was perfluorosilanized as well.

Flat punch micropillars were fabricated by molding from the PDMS negative. To produce T-shaped micropillars, flat punches were manually inked in a thin film of PDMS, precured at room temperature for 8-9 hours. Subsequently, the inked pillars were postcured in contact with a perfluorosilanized silicon wafer at 65 °C for 14 hours. The enlargement of the cap diameter was approximately 35%.

For the micro-contact printing setup, featureless flat stamps were produced for the setup. For their fabrication, unpatterned perfluorosilanized silicon wafers were placed as masters in the molding stations for the micro-contact printing stamps. A gasket between the stamp blank and the unpatterned master defined the height of the stamps. To further constrain the cavity, a cylindrical block was inserted into the stamp blank. PDMS was injected into the cavity of the stamp blank. After curing for 4 hours at 65 °C, the stamps were removed from

---

the molding stations and demolded from the gasket and the block. By inking the backside of the pillar microstructures with PDMS, they were attached to the stamps, and fixed by curing the connecting layer at 90 °C for one hour.

### *Preparation of Mechanosensitive Surfaces*

For the preparation of the mechanosensitive surfaces, a polyelectrolyte brush was synthesized in a *grafting from*-approach. As surface-initiator, 3-(trimethoxysilylpropyl)-2-bromo-methylpropionate (95 %) was purchased from Gelest (Morrisville, PA, USA). [2-(Methacryloyloxy)ethyl]trimethylammonium chloride (METAC, 80 wt. % aqueous solution), 2-aminoethyl methacrylate hydrochloride (AEMA, 90 %), triethylamine (99 %), 2,2'-bipyridine (99 %), copper(II)-chloride (99.999 %), copper(I)-bromide (99.999 %), 5(6)-carboxyfluorescein N-hydroxysuccinimide ester, dry toluene (99.8 %), and dimethyl sulfoxide (DMSO, 99.5 %) were purchased from Sigma-Aldrich Co. Round cover slips (Ø 24 mm) were purchased from VWR International GmbH. Deionized water was purified with a Milli-Q system (Merck Millipore, Darmstadt, Germany).

The mechanoresponsive polymer structures were prepared in a surface-initiated controlled radical polymerization, as published elsewhere.<sup>9</sup> Briefly, round cover slips were used as substrates. They were cleaned by sonication and oxygen plasma treatment, directly followed by immersion into a solution of surface-initiator in toluene. After attachment overnight, the surface-initiator was fixed at 150 °C for 4 hours. Each substrate was placed in a separate Schlenk tube under argon atmosphere. An isopropyl alcohol/water solution [7/2 (v/v)] of the monomers (METAC and AEMA [ratio 10 000:1]), copper(II)-chloride, and bipyridine were dissolved and degassed. Under argon atmosphere, copper(I)-bromide was added to the polymerization solution. It was dispensed among the substrate-loaded Schlenk tubes and left for 4 hours at room temperature under argon atmosphere. Then, the polymerization was quenched with ethanol.

For labeling, the substrates were immersed in 0.1 M hydrogen carbonate solution. Carboxyfluorescein was dissolved in DMSO and added to the immersed substrates. Overnight, the dye covalently bonded to the comonomer AEMA. Excess was removed by subsequent sonication in 1 M sodium chloride solution and water.

### *Determination of Contact Stress Distributions*

The contact formation of the stamps with the structures was controlled with a  $\mu$ CP-PVM-A micro-contact printer from GeSiM (Großberkmannsdorf, Germany). For a plane contact formation, the system is able to bulge the stamp by applying an overpressure (130-140 kPa) to compensate the concavity originating from the preparation. The movement of the stamps toward and away from the surface was performed with a stepper motor.

The micro-contact printer and the mechanosensitive surfaces were aligned on an Axio Observer Z.1 inverted microscope combined with an LSM710 confocal laser scanning module (Carl Zeiss Microscopy, Jena, Germany) to monitor the fluorescence response during contact. For the measurements, the cover slip with the mechanosensitive surface was fixed on a glass slide with a droplet of water in between. Before the measurements, the mechanoresponsive polyelectrolyte surface coating was wetted with Milli-Q water. After the measurements, the mechanosensitive surface coating was regenerated by extensive rinsing with Milli-Q water.

For the read-out of the mechano-response, the fluorescein dye was excited with an Ar laser at a wavelength of 488 nm from LASOS (Jena, Germany). Emission was detected at a wavelength interval from 493-685 nm. The pinhole size was fixed to 1 Airy unit (4.4  $\mu$ m). As objective, an EC Epiplan-Neofluar 20x/NA 0.5 was used (Carl Zeiss Microscopy, Jena, Germany).

The azimuthally averaged intensity profiles were generated with the Radial Profile Plugin (v.2009) in ImageJ 1.50d.

### *Electron Microscopy*

The shape of the micropillars was determined with scanning electron microscopy using a Zeiss Leo Gemini 1530 (Carl Zeiss Microscopy, Jena, Germany) equipped with a field-emission cathode with an operating voltage of 3 kV. Beforehand, the samples were sputtered with a 3 nm platinum layer.

### *Optical Microscopy*

An Axio Imager.A1m microscope with a 20x objective (Carl Zeiss Microscopy, Jena, Germany) and a SPOT Insight camera (Diagnostic Instruments Inc., Sterling Heights MI, USA) were used for bright-field and dark-field optical reflective microscopy of the pillar structures.

---

# V. Mechanoresponsive Hydrogel Particles as a Platform for Three-Dimensional Force Sensing

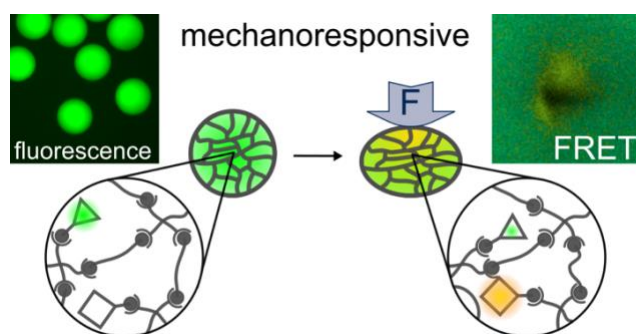
Some parts of the following chapter were published in the manuscript of the research article

“Mechanoresponsive Hydrogel Particles as a Platform for Three-Dimensional Force Sensing”

by Jens W. Neubauer, Nicolas Hauck, Max J. Männel, Maximilian Seuss, Andreas Fery, and Julian Thiele. *ACS Appl. Mater. Interfaces* **2019**, *11* (29), 26307–26313.

It is reprinted with permission, whereas the copyright remains with the American Chemical Society 2019. The text and the published figures of the manuscript are reused, expanded by content of the Supporting Information and unpublished content, and adapted to be integrated into this thesis.

---



Introducing a novel concept for mechanosensitive hydrogel microparticles, deformation is translated into changes in fluorescence so that they can function as mechanical probes. The hydrogel particles with controlled polymer network were produced via droplet microfluidics from poly(ethylene glycol) (PEG) precursors. Förster resonance energy transfer (FRET) donors and acceptors were coupled to the PEG hydrogel network for reporting local deformations as fluorescence shifts. It was demonstrated that global network deformations, which occur upon drying/rehydration, can be detected via a characteristic fluorescence shift. Combined characterization with confocal laser scanning microscopy and atomic force microscopy (AFM) showed that also local deformation of the particles could be detected. Using AFM, the mechanical properties of the particles could be quantified, which allows linking strain with stress and thus force sensing in a three-dimensional environment. Microfluidic material design allowed to precisely vary the size and the polymer network structure via the choice of the macromolecular precursors and their functionalization with fluorophores. The resulting changes in mechanical properties and mechanosensitivity qualify these hydrogel microparticles as an adjustable material platform for force sensing in structural mechanics or cell culturing.

---



## V.1. Concept for the Preparation and Characterization of Mechanoresponsive Polymer Network Structures

The mechanoresponsive polyelectrolyte brushes applied in the prior chapter are surface coatings. This structural feature limits their applicability to contact on planar surfaces. Moreover, mechanical stresses are signaled by changes in fluorescence. Such changes might not only originate from the quenching mechanism responsive to compression and tension, but also from photobleaching, which could induce errors in the measurements.

Particularly in the context of mechanobiology, mechanoresponsive materials have been developed and utilized to sense forces exerted by cells. These materials rely on various architecture, structure, and response mechanisms (cf. Section III.4). Cells usually interact dynamically in three-dimensional environment, but existing strategies lack of three-dimensionality,<sup>211</sup> cell-compatible matrices,<sup>180</sup> scalability,<sup>8</sup> or reversibility,<sup>230</sup> for example.

On this account, the approach is to develop a three-dimensional mechanically homogeneous network structure, reporting local deformations with a reversible response mechanism. Building from scalable motifs, the polymer network structures is to signal deformations in microscale resolution to bridge the length scales of existing approaches (Figure V-1).

Following design criteria derived from the Flory-Rehner theory, the aim was a homogeneous three-dimensional hydrogel network structure by preparing the network from macromolecular precursors which resemble Flory's and Rehner's tetrahedral cell. These 4-arm starpolymer precursors were coupled in a polymer-analogous gelation. For the purpose of reversibly reporting network deformations, FRET pairs were included in the network as "spectroscopic rulers".<sup>175</sup> The energy transfer from an excited donor (Alexa Fluor 488) to an acceptor molecule (Alexa Fluor 555) is distance-dependent.<sup>171,174</sup> Attached to the network, deformations cause changes in the distance between FRET donors and acceptors. With fluorophores coupled to precursors, the network was prepared via droplet microfluidics, yielding hydrogel microparticles. The hydrogel particles were characterized in a combined setup of CLSM and AFM, enabling characterization of mechanics and the fluorescent mechanoresponse.

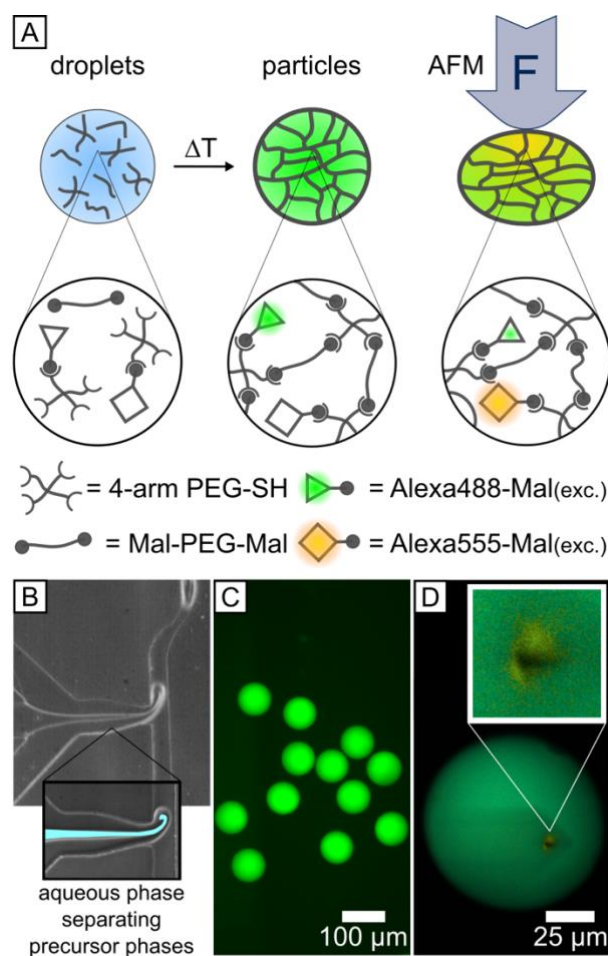


**Figure V-1.** (A) Concept of the mechanoresponsive hydrogel particles. The FRET pair fluorophores (Alexa Fluor 488 and Alexa Fluor 555) are coupled to 4-arm star PEG precursors before crosslinking with another PEG precursor in a Michael-type addition of thiol (SH) and maleimide (Mal) via droplet microfluidics. Mechanoresponsive particles are yielded to report network deformations by a localized FRET based fluorescence shift. (B) Microscopy image of the T- junction structure for droplet microfluidics. In the dispersed phase (entering from the left), an additional aqueous phase (colorized blue in the inset) separates the precursors to prevent premature reaction of the functionalities. (C) Fluorescence microscopy image of the gelled and demulsified hydrogel particles (only Alexa Fluor 488 fluorescence). (D) Confocal laser scanning microscopy (CLSM) image of a hydrogel particle depicting the fluorescence in true color. A pyramidal tip is indented into the hydrogel. The mechanical compression is causing the observed fluorescence shift (inset). Reprinted with permission from Neubauer et al.<sup>11</sup> Copyright American Chemical Society 2019.

## V.2. Droplet Microfluidics for the Preparation of Hydrogel Particles

### *Choice of Materials*

Design criteria for scalable polymer networks could be derived from the Flory-Rehner theory (cf. Section III.1.3).<sup>49,50</sup> Therefore, the hydrogel network was crosslinked from 4-arm star poly(ethylene glycol) (PEG) precursor molecules, as they resemble Flory's and Rehner's tetrahedral cell and their chain length is predefined. In contrast, a free radical polymerization with crosslinkers can lead to material inhomogeneities.<sup>94,95</sup> Moreover, PEG is a cell-compatible material.<sup>292</sup>

Still, the network formation is critically dependent on the efficiency of the crosslinking reaction. To oppose this, precursors terminated with maleimide and thiol functionalities were selected because of the high reactivity of this Michael-type addition reaction.<sup>293</sup> The precursors carried the same functionalities each (A-A and B-B type precursors). The same reaction was used for coupling FRET donors and acceptors to the network precursors. Alexa Fluor 488 and Alexa Fluor 555 functionalized with maleimide groups were linked to the thiol-PEG precursor before crosslinking. In general, phosphate buffered saline (PBS buffer) was used as medium for the thiol-Michael addition of maleimide in fluorophore-labeling and crosslinking to avoid acidic pH.<sup>293</sup>

With respect to the high reactivity of the crosslinking reaction, heterogeneities might arise if the mixing is slower than the network formation. Using droplet microfluidics, not only the reaction volume is reduced, but also microfluidic structures for fast and efficient mixing can be included (cf. Section III.1.3).

### *Development of the Microfluidic Structure*

Established for creating hydrogel particles,<sup>76</sup> a microfluidic structure with a cross-flow junction was employed in the first experiments (Figure V-2A). The two PEG precursor solutions were joined at the nozzle of the junction and dispersed into droplets by an oily continuous phase (surfactant-containing highly fluorinated polyether). The generated droplets were stabilized by a self-synthesized ABA-type triblock copolymer (PEG middle block, perfluoroether terminal blocks).<sup>294,295</sup> For mixing, the droplets were transported through a meander structure.

In principle, it was possible to generate controlled droplets of the precursor solutions. However, a premature reaction of the crosslinking groups at the interface lead to successive clogging of the nozzle within minutes (Figure V-2B). As a result, undefined droplets and fractures of the nozzle clogging were collected during the experiment. Moreover, the droplets ruptured in the meander structure (Figure V-2C). Ultimately, particles of polydisperse size distribution were yielded after gelation and demulsification (Figure V-2D).

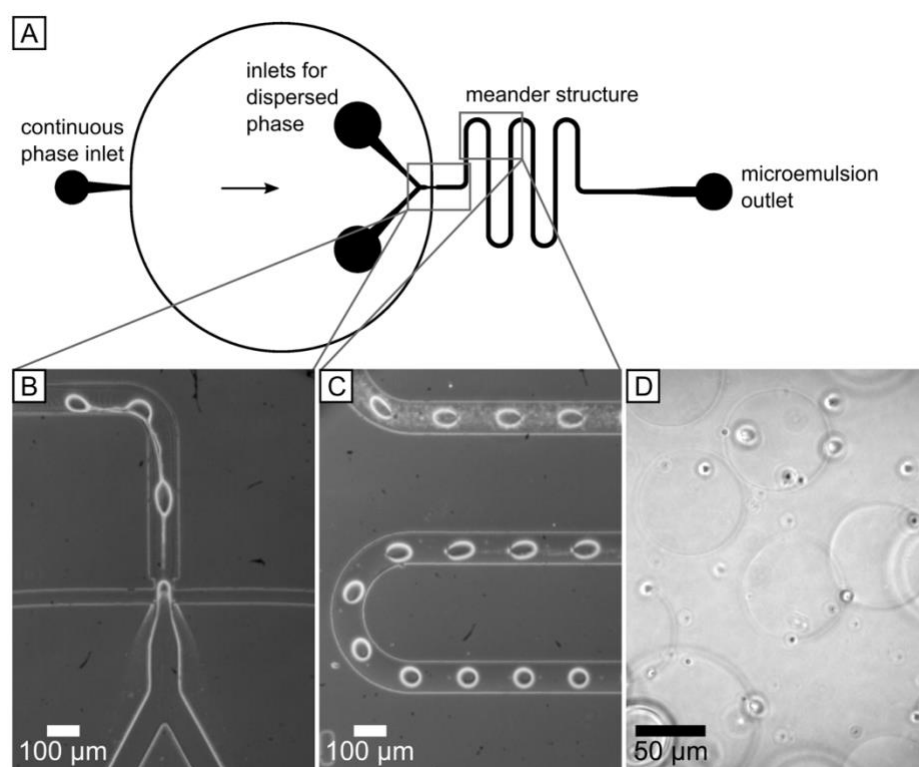


**Figure V-2.** (A) Microfluidic structure with cross-flow junction as computer-aided design. (B) Microscopy image of premature crosslinking reaction leading to nozzle clogging. (C) Microscopy image of droplet rupture in meander structure. (D) Microscopy image of the yielded hydrogel particles of polydisperse size.

From these first findings, the microfluidic preparation could be refined tackling the perceived issues. To avoid clogging of the nozzle, the premature reaction of the precursors needed to be suppressed. A third channel in the nozzle created an aqueous separating phase so that the crosslinking could not take place before droplet formation. Moreover, it is beneficial for adjusting the overall concentration of polymer in the droplets with a solvent being injected analog to the precursor solutions.

Besides premature crosslinking, both ruptured droplets in the meander structures and polydispersity in particle size indicated an insufficient droplet stability. As a consequence, the size dispersity might have originated from droplet coalescence and Ostwald ripening. Potential influences of the surfactant were encountered by changing to another synthesized batch. Moreover, trying to further avoid meander structures for mixing, the nozzle geometry was changed to a T-junction, assuming that the circular flow induced during droplet formation might be sufficient for mixing.<sup>83</sup> The specified changes resulted in a revised design of the microfluidic structure (Figure V-3).

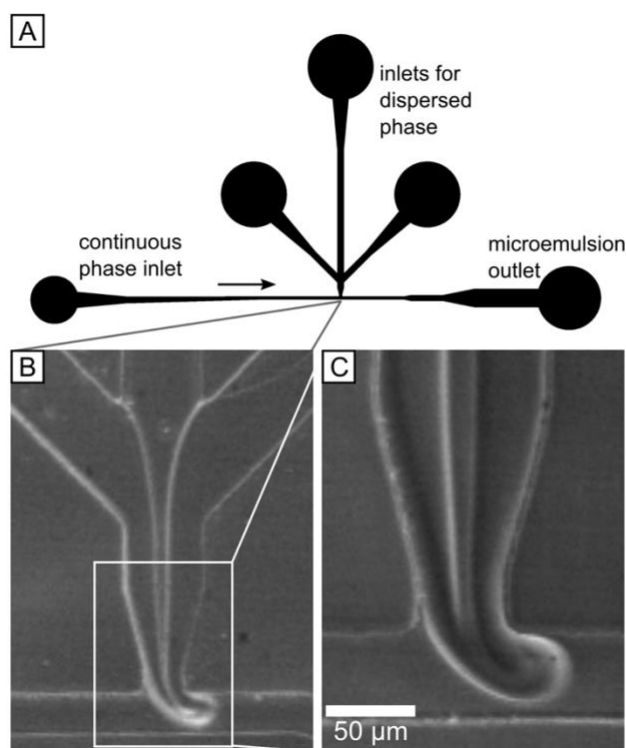


**Figure V-3.** (A) Microfluidic structure with T-junction as computer-aided design. (B) Phase-contrast microscopy image of the aqueous phases dispersed into droplets at the T-junction. (C) Close-up image of the laminar co-flow of the aqueous phase with a precursor-less separating phase to prevent premature crosslinking.

Employing a T-junction microfluidic structure with a third stream in the nozzle, premature crosslinking at the nozzle could be prevented by separating the precursors (PEG in PBS solutions) with an additional stream of pure precursor solvent (PBS). In general, a complete study of microfluidic regimes of this structure was omitted. The main focus was set on the determination of microfluidic conditions to generate defined droplets while suppressing nozzle clogging and the formation of satellite droplets. Satellite droplets can appear upon droplet breakup.<sup>296</sup>

As a generic guidance for the microfluidic flow conditions, the flow rates of the precursor phases were identical for equimolar amounts (here: 75  $\mu\text{L/h}$  each). For defined and stable droplet formation, the flow rate of the aqueous separating phase needed to be as high (here: 75  $\mu\text{L/h}$ ). While droplet formation at a lower flow rate of the separating phase (50  $\mu\text{L/h}$ ) was barely stable over minutes, higher flow rates of the separating phase expectably also enabled stable droplet formation (100  $\mu\text{L/h}$ ). As a drawback, this further diluted the precursor concentration in the droplet. With increasing dilution, the statistical distance between the reacting precursors in the droplet is increased. Accordingly, an encounter of the crosslinking reactants is less probable so that the network formation might be hampered or even prevented.

After collecting the generated microemulsion, it was treated thermally for completing the gelation. The gelled hydrogel particles were demulsified and transferred to an aqueous phase by exchanging the microfluidics surfactant (ABA triblock copolymer) for a weak surfactant (perfluorooctanol) under vigorous shaking.<sup>91</sup> The yielded hydrogel particles exhibited a spherical shape, but with an inhomogeneous distribution of the fluorophores, resembling Janus particles.

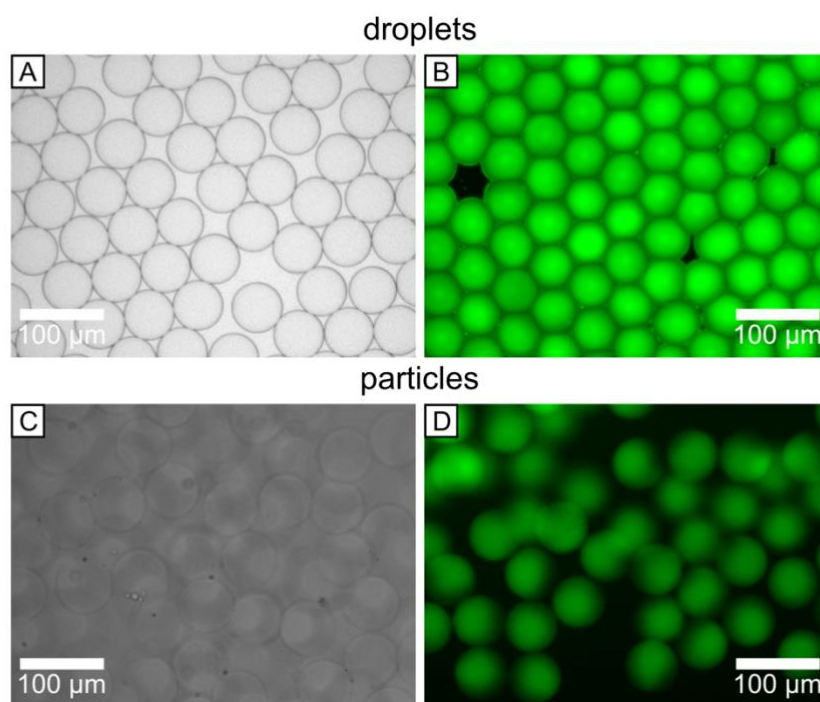


**Figure V-4.** Images of gelled hydrogels before demulsification in microemulsion droplets from bright-field (A) and fluorescence microscopy (B), and as particles after demulsification (C and D, respectively).

As a matter of fact, network formation must have occurred in the particles to a certain degree, in view of their spherical shape and their stability despite the rough conditions during demulsification. However, the inhomogeneous distribution of the fluorophore in the particles indicated incomplete mixing of the precursor droplets. Considering the reactivity of the precursors, more extensive mixing might be required quickly after droplet formation. Hence, a serpentine meander structure with narrowed turns for strong shearing was included in the microfluidic structure (Figure V-5A). Using phase contrast microscopy, the interfaces within the droplets could be visualized (Figure V-5B).

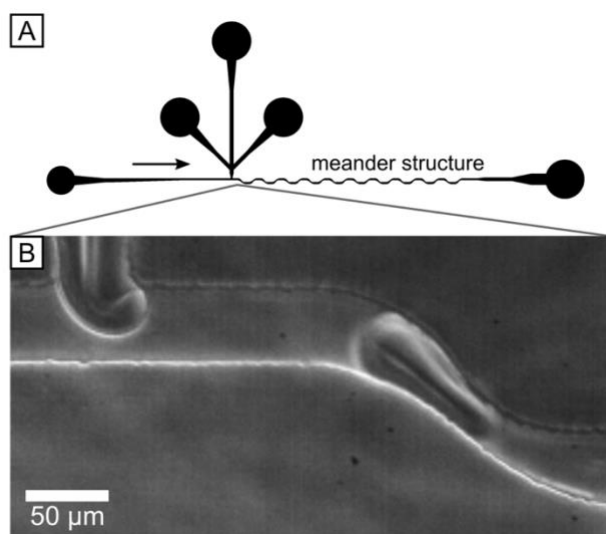


**Figure V-5.** (A) Microfluidic structure with T-junction and meanders as computer-aided design. (B) Phase-contrast microscopy image of the aqueous phases dispersed into droplets at the T-junction, and sheared in the meander structures.

Despite encounters with reduced droplet stability in the meanders of the preliminary experiments, the droplets did not rupture in the newly designed meanders. Consequently, microemulsions with low dispersity in size could be processed to homogeneously fluorescing particles upon gelation and demulsification (Figure V-6).

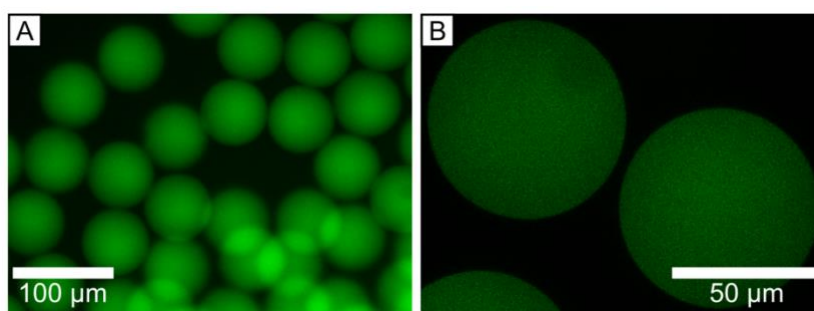


**Figure V-6.** Homogeneously fluorescing particles in fluorescence microscopy (A) and CLSM (B) exciting and imaging the donor fluorophore only.

---

### *Adaptions and Variations in Hydrogel Preparation*

Besides optimization in microfluidics, a large parameter space is available regarding the building blocks of the hydrogel network, the precursors and the fluorophores. Among these, certain building blocks were chosen as starting materials during the development of the microfluidic preparation method and altered selectively to assess the impact on the preparation and the yielded hydrogel structures. The central insights from the proceeded approaches are explained in the following.

In view of the Flory-Rehner theory as a blueprint, homogeneous networks are built up from tetrahedral cells with chains of equal length. To account for this, 4-arm star polymer precursors from PEG were selected, as the tetrahedral structure of the cells can be reflected in these precursors. In a polymer-analogous reaction, two types of 4-arm PEG precursors of similar size (MW 10 kDa) with either maleimides or thiol functionalities at each arm were coupled (4-arm PEG-Mal and 4-arm PEG-SH). Varying the network geometry, one 4-arm precursor was replaced by a bifunctional linker (PEG-diMal) in varying size. The high reactivity of the thiol-Michael addition reaction should facilitate quantitative crosslinking,<sup>293</sup> being another parameter to be altered. The reporter FRET pair fluorophores, Alexa Fluor 488 and Alexa Fluor 555, were carrying maleimides so that the thiol-PEG 4-arm precursors could be labeled before crosslinking, utilizing the same coupling reaction.

The number of fluorophores was related to the number of potential coupling groups, usually on the order of thousandths, varying in donor/acceptor ratios from 0.5:0.5 to 1:6 per mille thiols. Usually, these fluorophores are dissolved and stored in dimethyl sulfoxide (DMSO) to prevent the hydrolysis of the maleimide function. However, in some cases, partial gelation occurred already during the preparation of the precursor solutions after the addition of the fluorophore solutions. To circumvent disulfide bridging by DMSO,<sup>297</sup> the fluorophores were dissolved in water so that no DMSO was added to the aqueous thiol-PEG solution.

The amount and ratio of both fluorophores is expected to have an influence on the desired network response. Therefore, the adjustment of these factors needs to be in accordance with the investigated particle response. Without preempting results, the main focus was set on the formation of functional networks with responsivity to mechanical deformations (“proof



of concept”), while the sensitivity of the response mechanism was a secondary goal. For the adjustment of sensitivity, the fluorophore amount and ratio might be effective parameters.

Regarding the formation of functional networks, the concentration of both precursors was always adjusted to the same number of coupling groups so that a fully quantitative coupling for a perfect network was achievable theoretically. Hereby, the amount of fluorophore added was neglected with the fraction of fluorophore labeled thiols being 1 % and less.

Realistically, unreacted precursor functionalities might remain in the as-is crosslinked swollen network, but could meet upon network deformation, as for instance, from drying. When a fully crosslinked hydrogel network is collapsed by drying, its original dimensions should be restored upon reswelling. In case of the yielded hydrogel particles, smaller sizes and non-spherical shapes were observed after reswelling. For one thing, this might originate from adhesion to the glass substrate in collapsed state so that swelling expansion was hampered. Comparable geometrical constraints to network swelling have also been discussed in literature.<sup>54,298</sup> For another thing, further crosslinks might have formed during collapsing, as described. To prevent this, molecular maleimide was added to the hydrogel particles after demulsification for capping unreacted thiol groups and inhibiting delayed formation of covalent crosslinks.

Aiming to preserve the as-is crosslinked network structure, no changes could be perceived in the appearance of fluorescing hydrogel particles before and after capping. However, independent of the capping, the particles exhibited the same behavior upon reswelling after a complete collapse (Figure V-7).

This indicates that delayed reaction to crosslinks might not be the only constraint upon reswelling of the collapsed structures. Nevertheless, maleimide capping was conducted for a long-term stabilization of the hydrogel particles to avoid inter-particle crosslinking. Further alterations to influence reswelling might originate from entanglements (physical crosslinks) or rearrangement of the network (cf. phantom network model, Section III.1.3), besides mentioned adhesion on the surface.

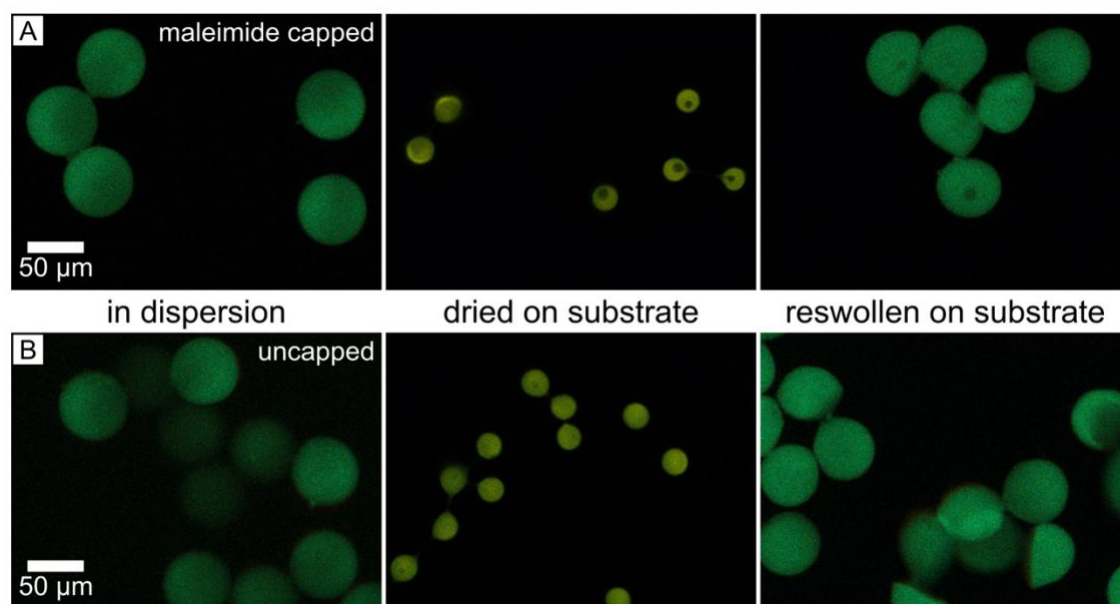


**Figure V-7.** Hydrogel particles of identical preparation with (A) and without maleimide capping (B) in PBS dispersion, and successively dried and reswollen in water.

The structure of 4-arm star polymers suggests that their steric interactions might differ from those of linear chains. This might contribute to physical crosslinking during collapsing and reswelling, but also hamper complete network formation.

In this regard, the 4-arm PEG-Mal precursors were replaced by respective bifunctional linear linkers (PEG-diMal) in two sizes (MW 2 kDa and 5 kDa) to crosslink the 4-arm PEG with thiol groups. The short linear linker (MW 2 kDa) was of comparable size to one arm of the star polymers (MW 2.5 kDa), the longer linker was of comparable size to two arms of the star polymers (MW 5 kDa). Thus, the network design was still based on tetrahedral cells, following the mentioned Flory-Rehner blueprint, but the distance between two potential junction points in the resulting network was increased (Figure V-8A).

Carrying out the microfluidic preparation, microdroplet emulsions could be generated with both combinations of the 4-arm PEG-SH and either of the bifunctional precursors. After gelation and demulsification, no particles were yielded with the 2 kDa linkers, however. Probably, the network had not been formed at all or partially incomplete so that the particles were ruptured owing to the rough conditions during demulsification.

Using the 5 kDa linkers, hydrogel particles could be achieved in similar size to comparable hydrogel particles formed solely from 4-arm precursors (Figure V-8B+C).

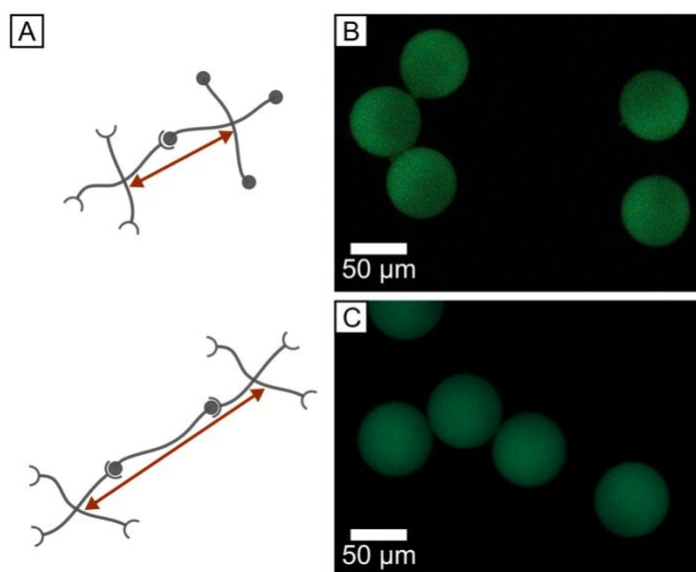


**Figure V-8.** (A) Schematic comparison of influence of precursor architecture on potential junction points. The CLSM images depict two batches prepared from the corresponding precursor system of two 4-arm precursors (B) and 4-arm precursor with bifunctional linker (C) at similar conditions.

The exchange of one precursor did not lead to substantially different particle sizes. Bearing in mind the dilution of precursor from the separating phase in microfluidics, it implies that the network in the depicted hydrogel particles is rather loose than completely formed.

The lower the precursor concentration, the larger is the statistical distance between potential coupling groups. Therefore, the precursor concentration represents another adjustment parameter for the network formation. To increase the precursor concentration in the droplet in the microfluidic system used, the dilution by the flow of the separating phase needs to be decreased or the concentration of the precursor feed solutions increased.

Up to the latest microfluidic design, the flow rate of the separating phase could not be lowered significantly below the flow rates of the precursor feeds while maintaining stable conditions. Mostly, the precursor feed concentration was around 4 wt. %, as it was for the hydrogel particles shown above (Figure V-8). Although microfluidic preparations with such precursors have been conducted in higher concentrations,<sup>98</sup> only concentrations up to 6 wt. % could be managed with the existing microfluidic structures in acceptable flow stability. Therefore, further optimization of the microfluidic design might also be beneficial for processing higher concentrations.

Ensuing from microfluidics and polymer coupling chemistry in parallel to influence the network formation, the kinetics of the coupling are expected to be another adjustment parameter in network formation. For the coupling reaction, the kinetics can be altered by

changing one reactant of the Michael-type addition, e.g. the addition of thiol to vinylsulfone is less reactive than to maleimide.<sup>293</sup> Accordingly, the coupling should occur slower so that mixing within the droplets is less impeded by the forming network. However, hydrogel particles of strongly inhomogeneous size resulted from this variation (Figure V-9). While the microemulsion droplets were of defined similar size, the differences probably arose during swelling after release from the emulsion droplets. They might originate from heterogeneity in crosslinking or expansion rupture. Either case could be caused by an incomplete network formation, as the divinylsulfone linker (MW 3.5 kDa) was shorter than the maleimide linker employed before (MW 5 kDa).

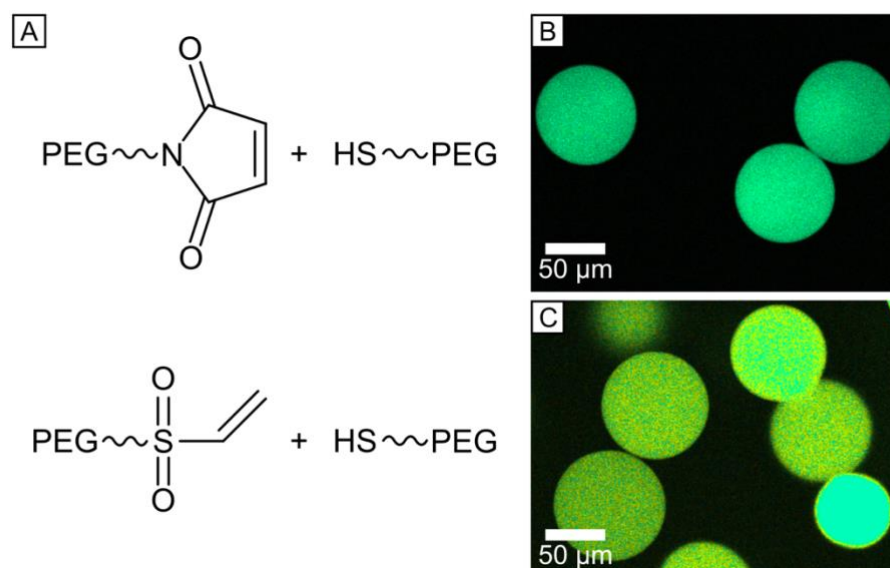


**Figure V-9.** (A) Scheme of the coupling reactions with CLSM images of the corresponding hydrogel particles crosslinked with a maleimide-thiol addition (B) and a vinyl sulfone-thiol addition (C). The particles were prepared with comparable precursor concentrations. Differences in fluorescence color originate from the fluorophore labeling ratio.

Although this particular experiment yielded particle of a broad size dispersion, it indicates how adjusting the crosslinking kinetics might help to affect the network formation, e.g. by controlling the temperature during preparation, or by blending precursors of varying reactivity. Indeed, this might require the adjustment of further parameters, but might also allow reducing the microfluidic separation phase. As an effect, higher effective precursor concentrations in the droplet could be reached. However, lower reactivity bears the risk of incomplete network formation so that the development in material design and microfluidic design are interconnected; they must go hand in hand.

In conclusion, the parameters and aspects discussed here do not only reflect challenges in preparation, but rather demonstrate the variability of adjustment for this material platform by precursor size, geometry, and concentration, as well as crosslinking chemistry. From this variety, parameter combinations were identified to yield homogeneously appearing hydrogel particles. These were further characterized regarding their responses to network deformations.

### V.3. FRET Response to Global Network Deformations from Swelling in Humidity

Attached to the network structure, the distance-dependency of the FRET pairs is to be exploited for reporting network deformations. To investigate this correlation between network deformations and fluorescence shifts between the FRET donor (Alexa Fluor 488) and acceptor (Alexa Fluor 555), the fluorescence response of the hydrogel particles to global network deformations was monitored with CLSM in spectral unmixing.

#### *Global Response from Collapse and Reswelling in Humidity*

The complete collapse of the hydrogel network is a strong global deformation. The dried particles exhibited a yellowish fluorescence, shifted toward FRET acceptor fluorescence, as already depicted above (Figure V-7).

To quantify the fluorescence shift from the global deformation of the hydrogel network, particles were dried for a complete collapse. From dried state, the collapsed hydrogel particles were reswollen successively in an environment with controlled humidity. For this purpose, the experiment was conducted in a sealed container (Figure V-10).

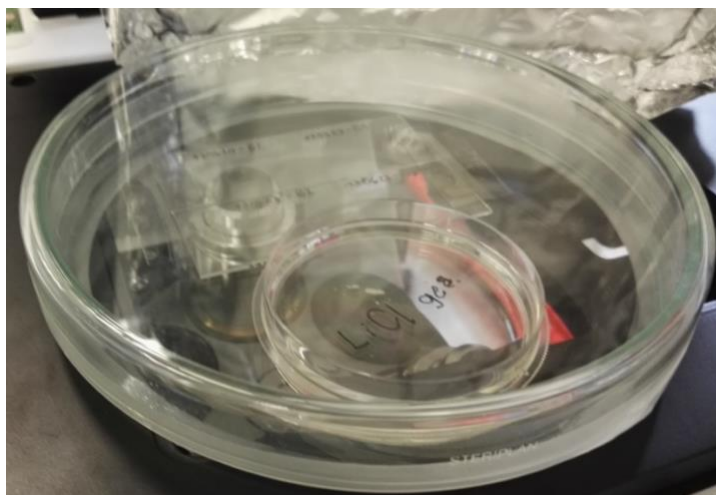


**Figure V-10.** Experimental setup of hydrogel particles dispersed on glass slides and kept in a sealed container with controlled humidity.

The humidity within the container was controlled by the vapor pressure of a saturated salt solution present in an open vial, and altered by exchange of the solution. Saturated aqueous solutions of lithium chloride (LiCl), potassium carbonate ( $K_2CO_3$ ), and sodium chloride (NaCl) equilibrated the relative humidity (RH) in the container to 11 %, 43 %, and 75 %, respectively.<sup>299</sup> CLSM images were taken in spectral unmixing for each step. With increasing humidity, a shift of the hydrogel fluorescence from orange over green-yellowish to green was observed (Figure V-11).

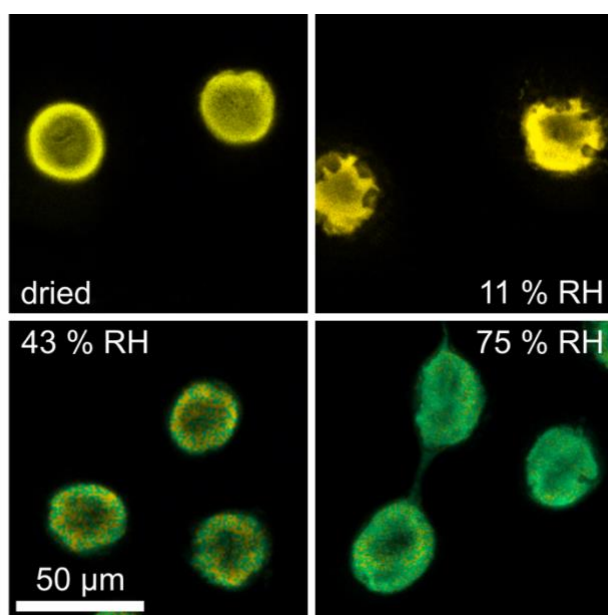


**Figure V-11.** True color CLSM images of hydrogel particles in dried state and successively reswollen in controlled humidity. Reprinted with permission and adapted from Neubauer et al.<sup>11</sup> Copyright American Chemical Society 2019.

To evaluate the fluorescence shift between FRET donor and acceptor, the intensities at their emission maxima were compared. Accordingly, spectrally unmixed confocal images at the emission maxima detection ranges were taken for evaluation. For that purpose, the intensity of the hydrogel particles (in grayscale units) in the FRET donor and acceptor images were read out and averaged.

The manufacturer's spectra of the fluorophores depict donor emission in the wavelength range of the maximum acceptor emission. From these spectra, the spectral bleeding of the donor in the acceptor intensity was assumed to be 25 % of the maximum donor emission intensity (Figure V-12).

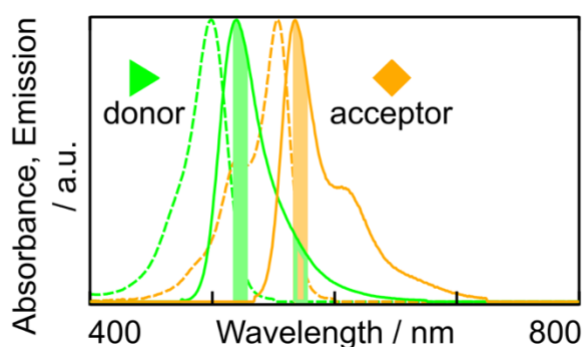


**Figure V-12.** Absorbance (dashed lines) and emission (solid lines) spectra of Alexa Fluor 488 (green) and 555 (orange) in solution.<sup>300</sup> For evaluation of the average donor and acceptor intensity, confocal scans in the detection ranges of the respective emission maxima (green and orange) were used. The spectral bleeding of the donor in the acceptor intensity (green line in orange bar) was estimated from these spectra and subtracted from the acceptor intensity. Reprinted with permission and adapted from Neubauer et al.<sup>11</sup> Copyright American Chemical Society 2019.

To account for the spectral bleeding of the donor in the acceptor image, 25 % of the determined donor intensity was subtracted from the determined acceptor intensity ( $I_{A,corr} = I_A - 0.25 I_D$ ). The FRET efficiency, as well as spectral bleeding, of a system can be determined with methods which require comparative material with either donor or acceptor labeling only (cf. Section III.3.2). For a direct measure of FRET in the prepared hydrogel particles, the average intensities were compared as FRET acceptor/donor intensity ratio ( $I_{A,corr} / I_D$ ) at each humidity (Figure V-13). The comparison shows two hydrogel particle systems prepared from 4-arm precursors, and from 4-arm precursors and bifunctional linkers, as compared before (Figure V-8).

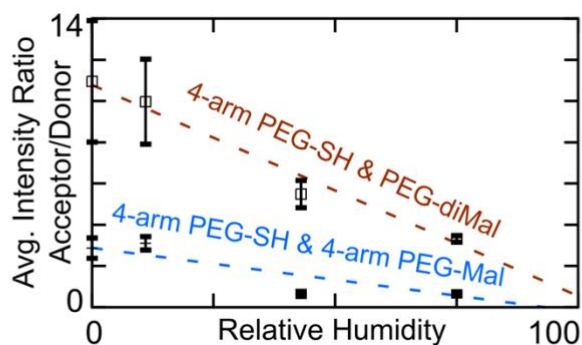


**Figure V-13.** Ratio of averaged acceptor and donor fluorescence intensity for hydrogel particles prepared from 4-arm precursors (crosses), and from 4-arm precursors and bifunctional linkers (open squares) with differing network and fluorophore concentration as a function of relative humidity. The error bars depict the standard deviation. The blue and red lines are guides to the eye. The compositions of both types of hydrogels are given below. Reprinted with permission and adapted from Neubauer et al.<sup>11</sup> Copyright American Chemical Society 2019.

In general, a strong correlation between the network deformation by humidity-induced swelling and the decrease in the ratio of acceptor/donor intensity can be derived for both the 4-arm precursor system (4-arm PEG-SH & 4-arm PEG-Mal) and the precursor/linker system (4-arm PEG-SH & PEG-diMal). In parallel to network expansion, the acceptor/donor ratio is shifting toward donor fluorescence, as expected from an increase of the fluorophore distances in the swollen hydrogel particles.

One of the main differences between the compared hydrogel systems was the number ratio of donor and acceptor fluorophores. In the precursor/linker system it was 1:6, whereas it was 1:1 in the 4-arm precursor system. Moreover, the two systems varied in precursor architecture and concentration. The 4-arm precursor system was prepared from solutions of 4-arm PEG thiol (MW 10 kDa) and 4-arm PEG maleimide (MW 10 kDa) in PBS (6 wt. % each), with a ratio of coupled donor and acceptor of 1:1, occupying approx. 0.1% of the available thiol groups. The precursor/linker system was prepared from solutions of 4-arm PEG thiol (MW 10 kDa) and PEG dimaleimide (MW 5 kDa) in PBS (4 wt. % each) with a ratio of coupled donor and acceptor of 1:6, occupying approx. 1% of the available thiol groups (for further information cf. Section V.7). All in all, the overall fluorophore concentration in the precursor/linker system was higher than in the 4-arm precursor system by a factor of five, besides potential differences in network structure.

These parameters directly affect the sensitivity of the hydrogel such that the precursor/linker system exhibits a stronger shift in the acceptor/donor intensity ratio with humidity, presumably due to its higher number of acceptor fluorophores. While the 4-arm precursor system shifts from yellow to green with increasing humidity (Figure V-11), the



acceptor/donor intensity ratio in the precursor/linker system was larger than one for up to 75% RH, meaning predominating acceptor intensity. Therefore, the particles appeared slightly yellowish in CLSM at all humidity steps.

To gather insight to the response functionality of the network, a statistical approach was based on the parameters of the 4-arm precursor system with an equimolar ratio of the FRET pair to simplify the assumptions.

### *Statistical Approach to the FRET Response from Humidity Reswelling*

For a deeper understanding of the FRET response of the 4-arm precursor system, statistically expectable fluorophore distances were taken from the preparation parameters and compared to the distance required for FRET.

The Förster radius of the coupled Alexa 488 and Alexa 555 fluorophores is 7.0 nm in solution.<sup>300</sup> The FRET efficiency decays to a power of six,<sup>171</sup> limiting efficient FRET to distances lower than approx. 15 nm (Figure V-14).

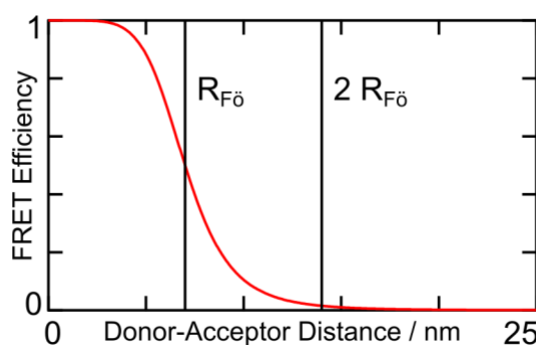


**Figure V-14.** FRET efficiency as a function of the donor-acceptor distance calculated for Alexa Fluor 488 and Alexa Fluor 555, assuming a Förster radius of 7.0 nm. Reprinted with permission and adapted from Neubauer et al.<sup>11</sup> Copyright American Chemical Society 2019.

From the preparation parameters, an average distance between donor and acceptor in the hydrogel network can be calculated from the molecular dimensions of the precursors. The fluorophores had been coupled to 4-arm thiol-PEG precursors in an equimolar ratio, occupying one thousandth of the thiol functionalities of the precursors. Hence, statistically one out of 250 thiol-PEG precursors carried either a donor or an acceptor. Assuming an alteration of donor and acceptor, an average donor-acceptor distance in the network can be approximated by the end-to-end distance in a random walk along the precursor molecules. The network was formed from 4-arm PEG-SH and 4-arm PEG-Mal precursors that were connected in an alternating order owing to the crosslinking reaction. Thus, the mentioned

average random walk comprises 250 maleimide-PEG and 251 thiol-PEG precursors (Figure V-15A).

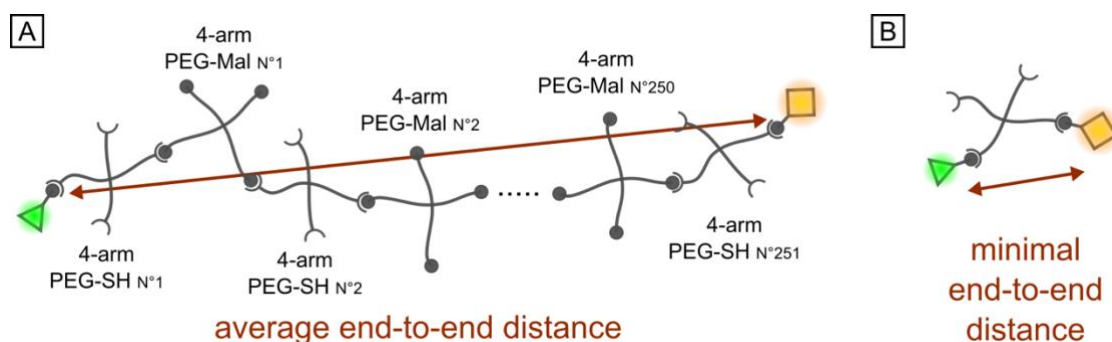


**Figure V-15.** (A) Scheme of random walk from donor to acceptor along the network for average end-to-end distance. (B) Limiting case of minimal end-to-end distance for both donor and acceptor being attached to the same precursor molecule.

Neglecting terminal functional groups, the end-to-end distance depicting the average donor-acceptor distance in the network can be calculated from the molecular weights of the 4-arm precursors (MW 10kDa each) and the monomer (MW 44 Da), and the effective length per monomer unit ( $l = 0.28$  nm).<sup>301</sup> For the network collapsed in dried state, the ideal chain model is assumed, giving the end-to-end distance  $R_0$ . For the fully swollen network, solvated Flory chains are assumed, giving the end-to-end distance  $R_F$  (cf. Section III.1.1).

$$R_{0,avg} = l \cdot ((251 + 250) \cdot 2 \cdot N_{arm})^{\frac{1}{2}} = 0.28 \text{ nm} \cdot 56932^{\frac{1}{2}} = 66.8 \text{ nm} \quad \text{cf. (1)}$$

$$R_{F,avg} = 0.28 \text{ nm} \cdot 56932^{\frac{3}{5}} = 199.7 \text{ nm} \quad \text{cf. (2)}$$

$$\text{with } N_{arm} = \frac{1}{4} \cdot \frac{10\,000 \text{ Da}}{44 \text{ Da}}$$

Both in dried and swollen state, the donor-acceptor distances in the network assumed from the average end-to-end distances  $R_{0,avg}$  and  $R_{F,avg}$  exceed the Förster radius of  $R_{F0} = 7.0$  nm drastically.

In contrast to the average value, one limiting case would be the donor and acceptor attached to the same 4-arm thiol-PEG precursor (Figure V-15B). Despite its relatively low probability, the according minimal donor-acceptor distances in the network can be determined from the corresponding minimal end-to-end distances in the dried ( $R_{0,min}$ ) and the fully solvated state ( $R_{F,min}$ ) to the following.

$$R_{0,\min} = l \cdot (2 \cdot N_{\text{arm}})^{\frac{1}{2}} = 0.28 \text{ nm} \cdot 114^{\frac{1}{2}} = 3.0 \text{ nm} \quad \text{cf. ( 1 )}$$

$$R_{F,\min} = 0.28 \text{ nm} \cdot 114^{\frac{3}{5}} = 4.8 \text{ nm} \quad \text{cf. ( 2 )}$$

Realistically, the discussed cases might be considered as boundary conditions for a distribution of donor-acceptor distances in the hydrogel network. Assuming it is described by a normal distribution, the probability density function of the donor-acceptor distance  $r_{\text{DA}}$  is given in equation (35).<sup>302</sup>

$$P(r_{\text{DA}}) = \frac{1}{\sqrt{2\pi\sigma^2}} \cdot \exp\left(-\frac{(r_{\text{DA}} - \mu)^2}{2\sigma^2}\right) \quad (35)$$

Both in dried and solvated state, a distribution of  $r_{\text{DA}}$  can be expected. The corresponding calculated average end-to-end distances may be the mean value  $\mu$  for each distribution ( $\mu_{0\% \text{RH}} = R_{0,\text{avg}}$  and  $\mu_{100\% \text{RH}} = R_{F,\text{avg}}$ ). The variance  $\sigma^2$  is determined from the width of the distribution of the donor-acceptor distance. The interval  $\mu \pm 3\sigma$  covers more than 99 % of the distribution. Thus, the interval  $\mu - 3\sigma$  is calculated from the boundary conditions so that the difference between the average value ( $\mu_{0\% \text{RH}} = R_{0,\text{avg}}$  and  $\mu_{100\% \text{RH}} = R_{F,\text{avg}}$ , resp.) and the minimal donor-acceptor distance ( $R_{0,\min}$  and  $R_{F,\min}$ , resp.) is approximated to be  $3\sigma$  of the distribution in dried and solvated state, respectively. For example, in the solvated swollen state,  $\sigma$  is calculated according to equation (36).

$$\sigma_{100\% \text{ RH}} = \frac{1}{3} \cdot (R_{F,\text{avg}} - R_{F,\min}) = \frac{1}{3} \cdot (\mu_{100\% \text{ RH}} - R_{F,\min}) \quad (36)$$

As it is assumed that the ideal chain and the Flory chain reflect the chain conformation at 0 % and 100 % RH, respectively, the donor-acceptor distances are interpolated linearly for the humidity steps in between. Below, it is shown exemplarily for 11 % RH: the mean donor-acceptor distance  $\mu_{11\% \text{ RH}}$  (equation (37)) and the minimal donor-acceptor distance  $r_{\text{DA},\min,11\% \text{ RH}}$  (equation (38)) are interpolated from the end-to-end distances in dried and solvated state, whereas  $\sigma$  is calculated analog as before (cf. equation (36)).

$$\mu_{11\% \text{ RH}} = \mu_{0\% \text{ RH}} + 0.11 \cdot \mu_{100\% \text{ RH}} = R_{0,\text{avg}} + 0.11 \cdot R_{F,\text{avg}} \quad (37)$$

$$r_{\text{DA},\text{min},11\% \text{ RH}} = R_{0,\text{min}} + 0.11 \cdot R_{F,\text{min}} \quad (38)$$

$$\sigma_{11\% \text{ RH}} = \frac{1}{3} \cdot (\mu_{11\% \text{ RH}} - r_{\text{DA},\text{min},11\% \text{ RH}}) \quad \text{cf. (36)}$$

From the  $\mu$  and  $\sigma$  values yielded in these interpolations, normal distributions of the donor-acceptor distance  $r_{\text{DA}}$  could be calculated at each humidity step (Figure V-16). Consistently, the distribution is significantly narrower in collapsed state (ideal chain model) than for the fully solvated and swollen network (Flory chain model).

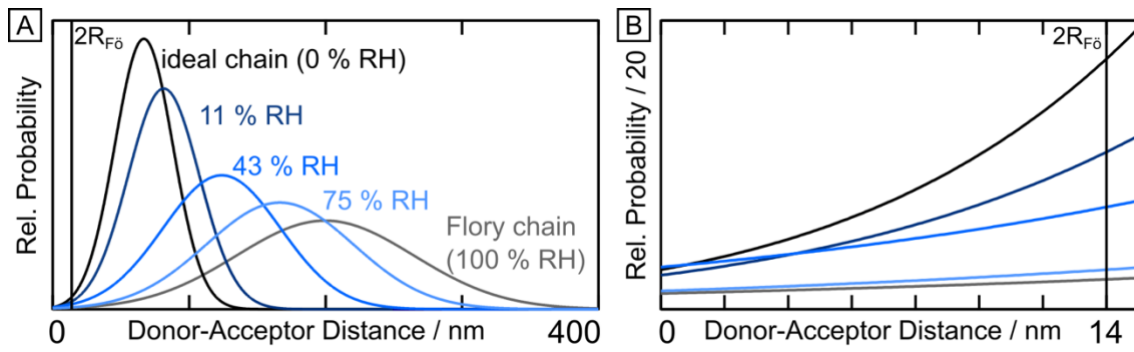


**Figure V-16.** (A) Theoretically derived normal probability distributions of the donor-acceptor distances in the hydrogel network at investigated humidity steps. For comparison, the two-fold Förster radius  $2R_{F0}$  is indicated (black line). (B) Close-up plot of the probability distributions within the two-fold Förster radius.

The comparison of the derived distribution ranges with the plausible FRET distance range, the two-fold Förster radius, reveals that only a minor number of fluorophores might be in a distance able to contribute to the observed fluorescence shift, at least according to this model. A closer look to the relevant distances below the two-fold Förster radius, a qualitative compliance with the observed fluorescence shifts was found (Figure V-16 B).

Although a statistical model simplifying the donor-acceptor distance distributions to a two-body problem along one model chain is not sufficient to describe a whole network, the derived results already give a qualitative validation of the observed effect. For a full description, the statistical model would need to be expanded from one chain with two fluorophores to a 3D network structure, accounting for further donor and acceptor fluorophores in the surrounding. Moreover, unequal donor/acceptor number ratios need to be taken into account. However, these first promising approaches offer a perspective for future theoretical studies on this hydrogel platform.

## V.4. Mechanical Characterization of the Hydrogel Network Structure

AFM was utilized for investigating the fluorescence response to mechanical deformations. It allows to apply mechanical loads and monitor the resulting deformation. Therefore, it is well suited for mechanical characterization of the hydrogel particles. To ensure a defined interaction geometry, colloidal probe AFM (CP-AFM) was used as it features spherical particles as probes indenting into the hydrogel particles. In regard to the mechanical properties and the fluorescence response to mechanical triggers, hydrogel particles prepared from the aforementioned precursor/linker system were investigated (4-arm PEG-SH & PEG-diMal, cf. Section V.3).

Commonly, the elastic properties of hydrogel particles are evaluated with continuum mechanics models of elastic spheres (cf. Section III.2).<sup>148-150</sup> Indentation experiments were conducted on hydrogel particles with CP-AFM to determine the Young's modulus (19.59  $\mu\text{m}$  CP diameter). The processed force-indentation plots typically showed a slight hysteresis between approach and retraction, and strong adhesion (Figure V-17A).

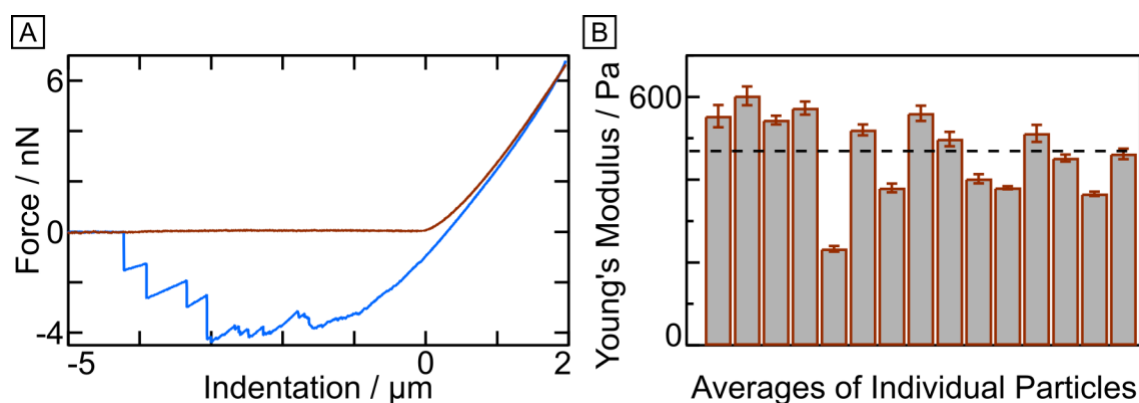


**Figure V-17.** (A) Typical AFM force-indentation curve on a hydrogel particle, illustrating approach (red) and retraction (blue). (B) Average Young's modulus of 15 hydrogel particles evaluated with the Hertz model. The error bars depict the standard deviation between the measurements on each particle (usually five indentations each). The dotted vertical line denotes the overall average value. Reprinted with permission and adapted from Neubauer et al.<sup>11</sup> Copyright American Chemical Society 2019.

Within the initial indentation of up to 600-800 nm, the data matches the Hertz model. Despite the observed adhesion, the data usually could be fitted to the power law of the Hertzian contact ( $F \propto d^{\frac{3}{2}}$ ) with a deviation of 5 % or less. Data with a stronger deviation was not taken into account for the statistics (Figure V-17B). From the indentation of 15 hydrogel particles, the Young's modulus was averaged to  $469 \pm 101$  Pa.

For investigating the behavior of the hydrogel particles at large deformations, a different experimental setup for CP-AFM was utilized (JPK CellHesion, cf. Section V.7 for further details). Moreover, a larger CP (approx. 53  $\mu\text{m}$  diameter) in a size similar to the hydrogel particle size (approx. 80  $\mu\text{m}$  diameter) was used for a more global deformation of the particles.

Applying large forces on the order of micronewtons, the deformation at certain forces was read out from the force-indentation plots of individual particles (Figure V-18). For comparison, they were plotted next to the idealized force-deformation behavior of a Hertzian elastic sphere, possessing a Young's modulus of 469 Pa as determined for the particles in prior experiments.

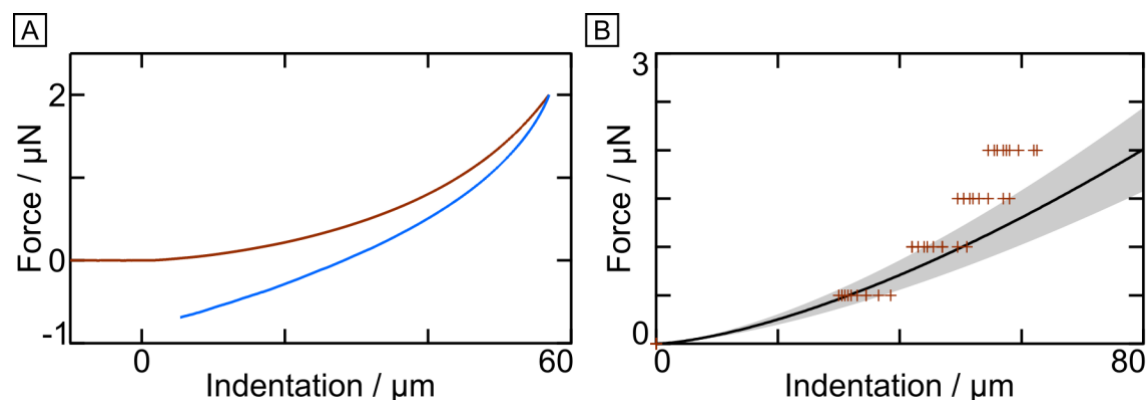


**Figure V-18.** (A) Typical force-indentation curve on a hydrogel particle in an experimental setup for large forces and large deformations, illustrating approach (red) and retraction (blue). (B) Indentation values of ten individual particles at certain forces extracted from the corresponding force-indentation curves (red crosses) in comparison with the idealized force-deformation curve (black line) of a Hertzian elastic sphere with the Young's modulus determined before ( $469 \pm 101$  Pa). The gray shade around the line depicts the standard deviation. Reprinted with permission and adapted from Neubauer et al.<sup>11</sup> Copyright American Chemical Society 2019.

The direct comparison expectably reveals a strong deviation between the Hertz model and the hydrogel particles at forces above 1  $\mu\text{N}$ . As the Hertz model is based on small, purely elastic deformation, additional permanent or time-dependent contributions arising at larger deformations are not taken into account. This is even more obvious when comparing a sequence of indentations to the same hydrogel particle (Figure V-19).

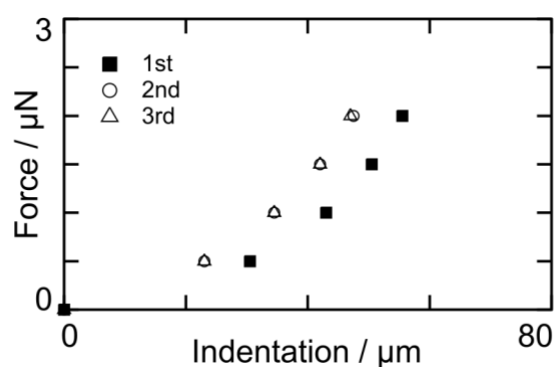


**Figure V-19.** Indentation values at certain forces extracted from consecutive force-indentation curves of the same particle. Reprinted with permission and adapted from Neubauer et al.<sup>11</sup> Copyright American Chemical Society 2019.

After the first indentation, the following indentations were conducted in the same manner without any delay. At the same force, a smaller indentation was reached at the second and third cycle. This is a strong indication of permanent or time-dependent deformation of the material. In case of a hydrogel, this may be plastic deformation or squeezing out of solvent which would take time to reswell. Consequently, these contributions add up to the elastic forces and result in the determined forces higher than predicted by the Hertz model. This is pronounced stronger for indentation larger than 40  $\mu\text{m}$ . From the opposite view, however, an acceptable agreement between the large indentation measurements and the Hertz model might be up to a force of 1  $\mu\text{N}$ . Models for describing large deformation of hydrogels<sup>303,304</sup> might contribute in future studies to elucidate the effects at large forces.

Both, the determination of the elastic properties and the behavior at large deformation are essential to understand the mechanical behavior of the hydrogel particles. Eventually, defined and predictable mechanical behavior are required to correlate the hydrogel mechanoresponse to the acting forces for an application as force sensor.

---

## V.5. FRET Response to Mechanical Deformations of the Hydrogel Network

The fluorescence response to strong network deformations from collapse and swelling in humidity indicated the desired functionality of the mechanoresponse concept. In these experiments, the precursor/linker system (4-arm PEG-SH & PEG-diMal) showed a more pronounced FRET shift during swelling in humidity. Therefore, these hydrogel particles were investigated regarding their mechanical properties and put to proof for fluorescence response to mechanical compression.

Utilizing the ability to apply defined loads with AFM, indentation experiments were conducted in a combined CLSM-AFM setup to image the fluorescence of the particle *in situ* with CLSM. Besides microscopy characterization, hydrogel particles of various network and fluorophore composition were tested for a fluorescence response to mechanical indentation. However, only the hydrogel particles prepared from the aforementioned precursor/linker system are discussed here. Exhibiting the most pronounced response to mechanical compression, these particles were chosen for an in-depth characterization and development of a validation method for the mechanoresponse.

### *Global Mechanoresponse to Mechanical Deformations*

Similar to the indentation experiments at large forces, a CP-AFM probe in a size similar to the hydrogel particle (approx. 53  $\mu\text{m}$  CP diameter to approx. 80  $\mu\text{m}$  particle size) was indented into the hydrogel particles for causing deformation all over the hydrogel network. The applied load was increased incrementally. CLSM images were taken in between with the load kept constant (Figure V-20).

Aiming for monitoring the changes in the overall emission of the hydrogel network, the focus of the CLSM images at each force increment was adjusted to the midplane of the deformed particle, i.e. the focal plane in which the hydrogel particle appeared largest. In the series of spectrally unmixed CLSM images, a shift in the detected color could be observed (Figure V-20B).



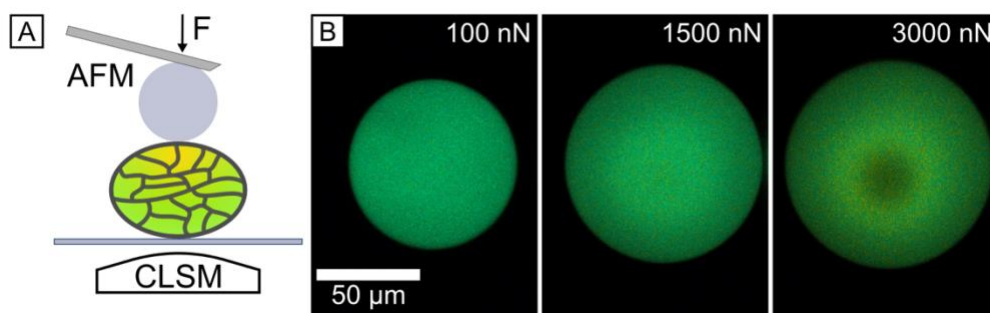


**Figure V-20** (A) Scheme of the combined setup utilizing CP-AFM and CLSM to trigger and detect the mechanoresponse of the hydrogel particles. The size ratio of the CP and the particle are to scale (approx. 53:80  $\mu\text{m}$  diameter). (B) True color CLSM images of the same particle at the denoted loads. The black shade at 3000 nN originates from the CP.

Similar to the swelling experiments, the average intensities of the donor and the acceptor emission maxima were determined at each load over the whole particle focal plane. Analog, the spectral bleeding of the donor in the detected acceptor intensity was corrected and plotted as a function of the applied load (Figure V-21).

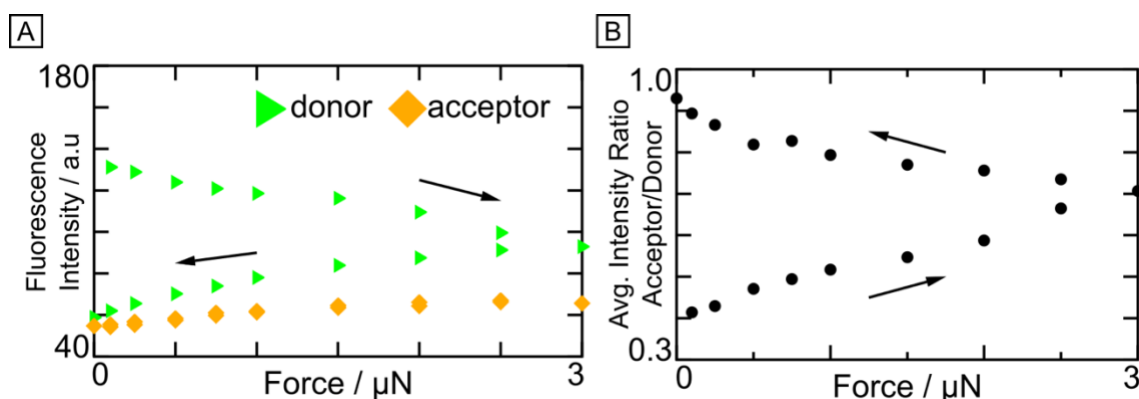


**Figure V-21.** (A) Fluorescence intensity of the donor (green triangles) and the acceptor (orange squares) averaged in the particle midplane, and (B) resulting acceptor/donor intensity ratio as functions of the applied load. The arrows are to guide the eye along the loading-unloading cycle in both plots.

While the acceptor intensity was comparably unchanged over the loading-unloading cycle, the donor intensity and the resulting acceptor/donor intensity ratio were significantly diverging between loading and unloading. Whereas a shift of the A/D intensity ratio toward the acceptor signal is expected upon loading and compressing the network, it would be expected to shift back toward donor signal when unloaded. However, a further decrease in donor intensity and a further increase in A/D intensity ratio was observed for the unloading increments.

With the images being taken successively, a time-dependent effect might be superimposing the desired response to the mechanical stimuli. As the donor intensity decreased apparently independent of the load, photobleaching of the donor fluorophores might be an explanation. Imaging an uncompressed, pristine hydrogel particle serially with the same parameters as in the indentation series, a strong indication for photobleaching was verified (Figure V-22).

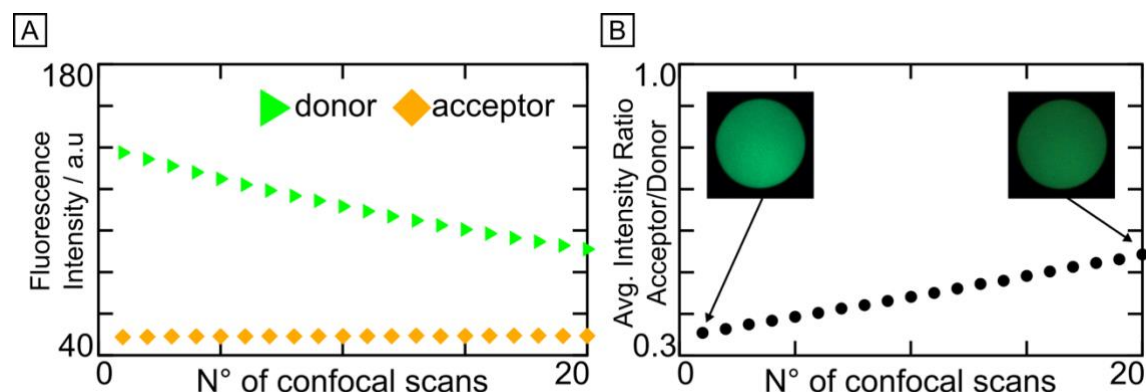


**Figure V-22.** (A) Fluorescence intensity of the donor (green triangles) and the acceptor (orange squares) averaged in the particle midplane, and (B) resulting acceptor/donor intensity ratio as functions of the confocal scan repetition. The inset true color CLSM images depict the particle in the first and the last scan.

The acceptor intensity does not change notably in the series, but a strong decay of approx. 35 % in the donor intensity is found over 20 scans. This decay causes a significant shift in acceptor/donor intensity ratio. On the one hand, this finding reveals that close attention has to be paid to photobleaching for interpretation of the data. On the other hand, it is a strong indication that the acceptor fluorophore is uninfluenced by the laser source exciting the donor fluorophores during scanning.

For interpreting the data of global particle deformation by CP-AFM, the donor photobleaching needs to be compensated. As an internal standard for photobleaching, a neighboring uncompressed particle was taken as control (Figure V-23).

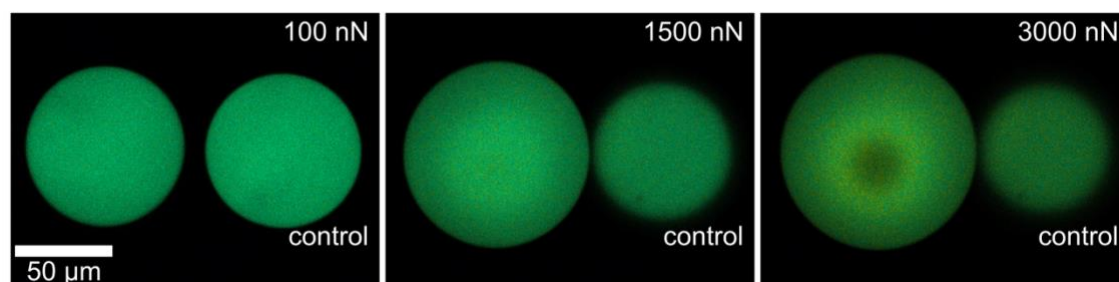


**Figure V-23.** Load increment series of the same particle as in Figure V-20 with depiction of a neighboring control particle to determine the influence of donor photobleaching.

In each image  $i$ , the control particle's donor intensity  $I_{D,ctrl,i}$  is compared to its original intensity  $I_{D,ctrl,0}$  in the very first image. This ratio is then used as correction factor for the donor intensity of the compressed particle  $I_{D,comp,i}$  to compensate for photobleaching in the corresponding image  $i$ .

$$I_{D,bleach.corr., i} = I_{D,comp,i} \cdot \frac{I_{D,ctrl,0}}{I_{D,ctrl,i}} \quad (39)$$

For depicting the global A/D intensity ratio shift as a function of the load increments, the acceptor intensity is corrected for spectral bleeding, and the donor intensity is compensated for photobleaching with the described correction factor (Figure V-24).

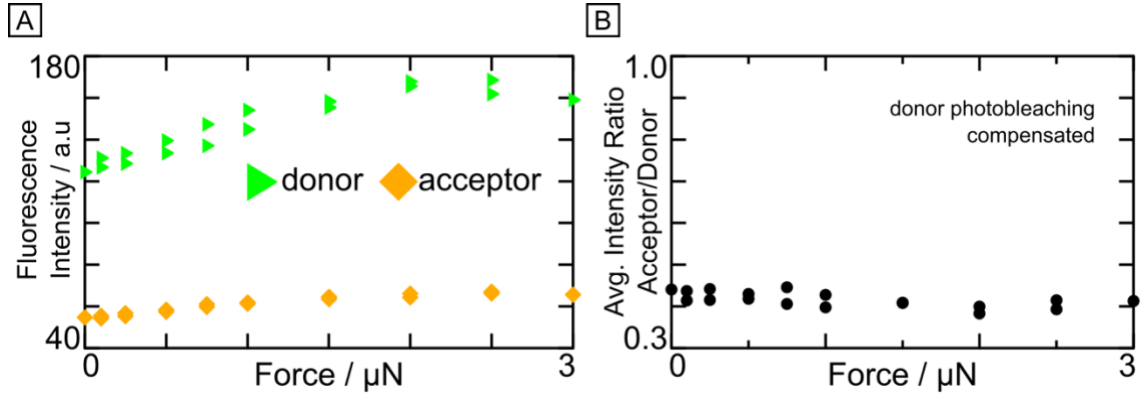


**Figure V-24.** (A) Photobleaching compensated fluorescence intensity of the donor (green triangles) and fluorescence intensity of the acceptor (orange squares) averaged in the particle midplane, and (B) resulting acceptor/donor intensity ratio as functions of the applied load.

Comparing the donor photobleaching compensated intensity plot (Figure V-24) with the uncompensated one (Figure V-21), it is most notably that the donor intensity does not diverge over the loading-unloading cycle, but rather shows good agreement indicating a successful compensation of the photobleaching effect. The acceptor intensity is depicted identical in both plots. Both donor and acceptor intensity increased with load, whereas the increase seemed to be more pronounced for the donor. However, the acceptor/donor intensity remained relatively constant at a value of 0.4 over the whole loading-unloading cycle. Therefore, the observed intensity increase might originate from an overall compression of the hydrogel.

In contrast to the strong fluorescence response observed during collapse and reswelling in humidity, no global response in the A/D intensity ratio could be identified for deformation with CP-AFM. For one thing, the A/D intensity ratio was majorly influenced by the

occurring photobleaching of the donor. For another thing, the compression of the hydrogel was strongest at the apex of the CP whereas a significant share of the hydrogel particle was squeezed around the probe so that strong compression in the center and stretching deformation from squeezing might average out a detectable effect. Accordingly, the mechanoresponse is investigated more locally in the following.

### *Local Mechanoresponse to Mechanical Deformations*

The stress acting on the hydrogel network originated from a localized indentation of a spherical probe. Therefore, the fluorescence response should be more pronounced in the surrounding of the indented CP, the origin of the mechanical deformation.

When imaging with higher magnification (63x oil immersion objective, compared to 20x air objective in previous images), also the confocal resolution in *z*-direction is expected to be higher (cf. Section III.3.3) so that the resolution in all dimensions is increased. As in prior experiments, the hydrogel particle was imaged while the applied load was kept constant (Figure V-25). The focal plane was set to the apex of the indented CP, visible as a cyan-blueish reflection of the exciting laser (488 nm).

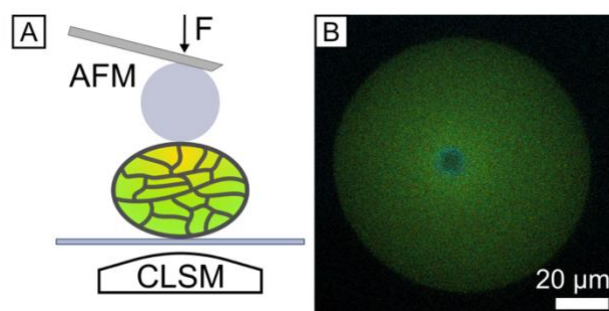


**Figure V-25.** (A) Scheme of the combined setup utilizing CP-AFM and CLSM to trigger and detect the mechanoresponse of the hydrogel particles. The size ratio of the CP and the particle are to scale (approx. 53:80  $\mu\text{m}$  diameter). (B) True color CLSM image of a hydrogel particle indented by a CP at 7  $\mu\text{N}$  load (cyan-blueish reflection of the apex). Reprinted with permission and adapted from Neubauer et al.<sup>11</sup> Copyright American Chemical Society 2019.

The hydrogel surrounding the CP exhibited a slight yellowish fluorescence shift toward FRET acceptor emission owing to compressive deformation of the material. Moreover, the compression lead to a localized increase in overall fluorescence intensity because of an increase of fluorophore concentration in the confocal volume. This could be identified in spectrally unmixed images of the donor and acceptor emission maxima (Figure V-26). Similar indications were observed in the global fluorescence response to CP indentation.

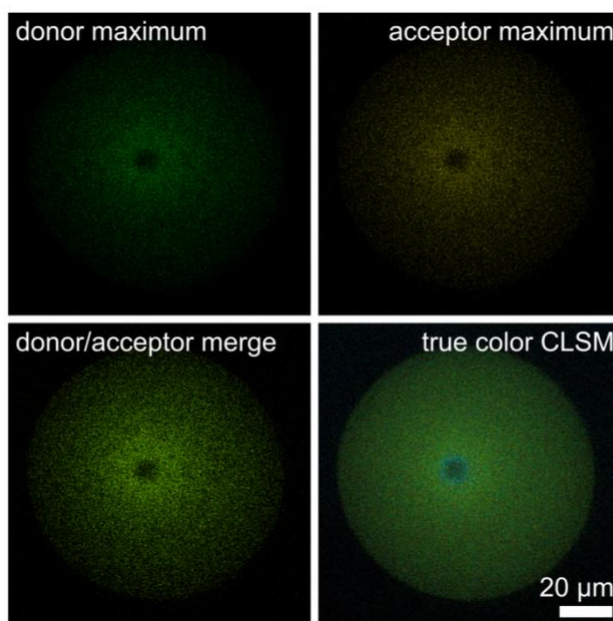


**Figure V-26.** Spectrally unmixed confocal images of a hydrogel particle indented with CP-AFM at  $7\mu\text{N}$ , illustrating the detection channel of the donor and acceptor emission maxima (top). The image of both maxima channels merged (bottom left) is placed next to the true color image (bottom right), comprising all of the detected channels. Brightness and contrast of the images were adjusted for illustration. Reprinted with permission and adapted from Neubauer et al.<sup>11</sup> Copyright American Chemical Society 2019.

In analogy to the evaluation of global responses to hydrogel particle deformation above, the local fluorescence shift was determined by the acceptor/donor intensity ratio from the spectral confocal images comprising the according emission maxima. To correlate the local fluorescence shift with the mechanical stress applied by the CP, the spatially resolved intensities of the FRET donor and acceptor were averaged azimuthally as a radial function of the distance from the center of the CP, which is the origin of the mechanical stress (Figure V-27A, white sketch).

The reflection of the CP was utilized to align the area for azimuthal averaging, but the radial function was averaged from a circular section only. If the full circular area was averaged to a radial function, an offset in aligning the centers of the averaging area and the CP could attenuate or even nullify radial features in the averaged function.

Whereas the spectral bleeding in the acceptor intensity was corrected analog to all prior evaluations, the photobleaching of the donor was not taken into account because the compared intensities originated from the same image.

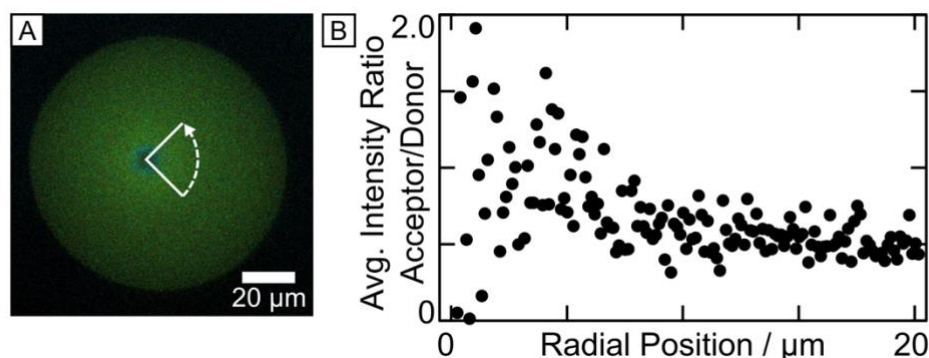


**Figure V-27.** (A) True color CLSM image of a hydrogel particle indented by a CP at 7  $\mu\text{N}$  load (cyan-blueish reflection of the apex). The white sketch marks the circular section, where the fluorescence intensity of the donor and acceptor was averaged azimuthally as a radial function. Brightness and contrast were adjusted for illustration. (B) Ratio of the average fluorescence intensity of the acceptor and donor during CP indentation, corresponding to the radial function marked in (A). Reprinted with permission and adapted from Neubauer et al.<sup>11</sup> Copyright American Chemical Society 2019.

Strikingly, the determined acceptor/donor ratio in the hydrogel was shifted toward acceptor fluorescence in close vicinity to the center. The acceptor/donor shift was most pronounced within a radial distance of approx. 8  $\mu\text{m}$ , correlating with the size of the CP reflection. The increased scattering of the data at smaller radii is most probably an artifact of azimuthal averaging, as noise is more present with less pixels averaged. As a result, the localized fluorescence shift toward acceptor intensity can be attributed to the mechanical compression of the hydrogel under the CP apex. This mechanoresponse could be observed in several particles, as depicted in a representative overview (Figure V-28).



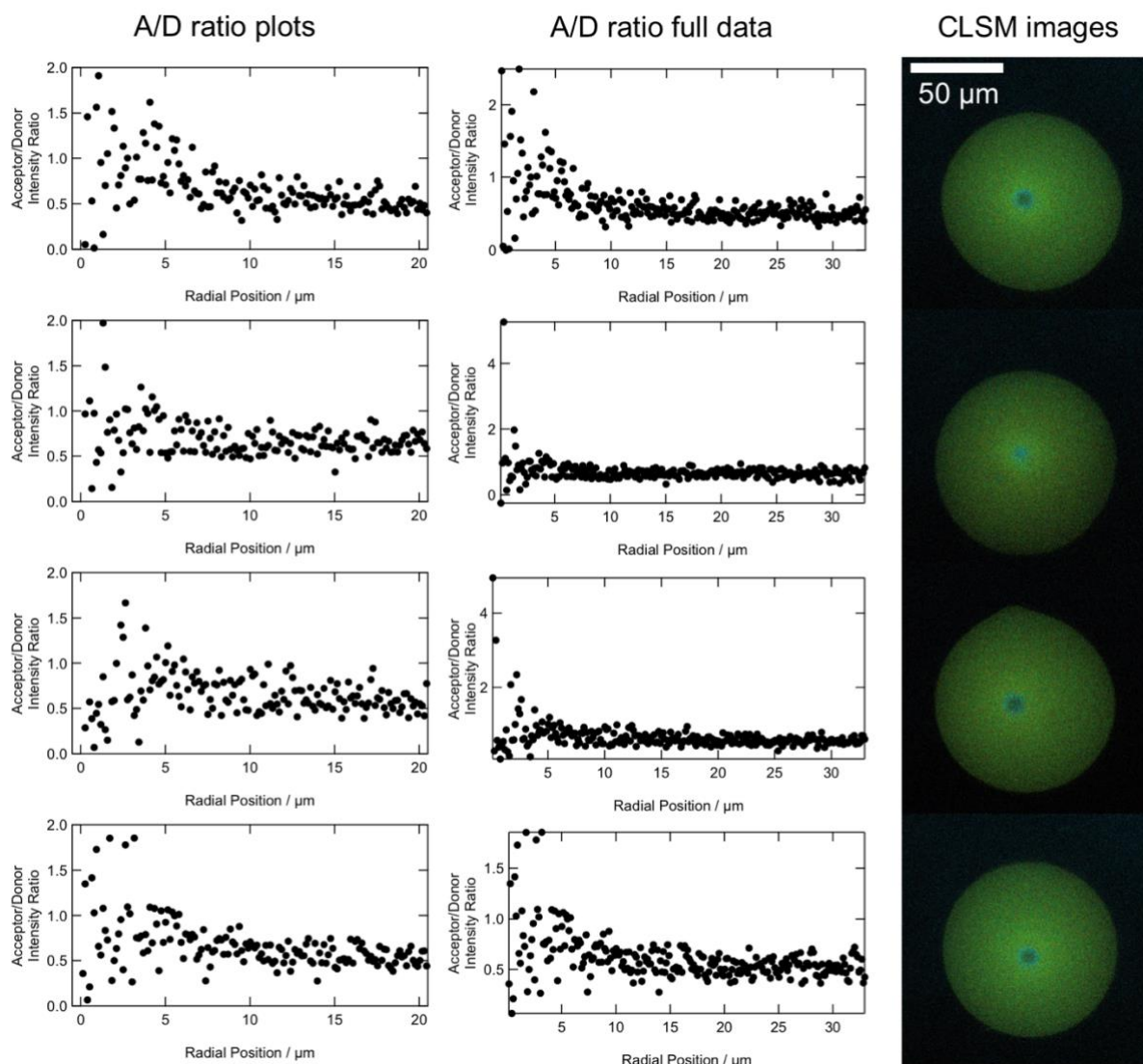


**Figure V-28.** Mechanoresponse in hydrogel particles as representative selection of acceptor/donor intensity ratio plots (left column). The first plot on the top left is shown in Figure V-27. Next to the plots of each particle, the corresponding full data for each particle (middle column) and the corresponding CLSM images are shown (right column). Reprinted with permission and adapted from Neubauer et al.<sup>11</sup> Copyright American Chemical Society 2019.

The mechanoresponse of these hydrogel particles was more pronounced at larger AFM loads. The data depicted above was observed at 7  $\mu\text{N}$  load. To benchmark the stress resolution of the hydrogel particles, the pressure profile under the CP is calculated at the smallest load (1  $\mu\text{N}$ ) triggering a detectable mechanoresponse (Figure V-29).

For the calculation of the local pressure acting at the CP apex, the Hertz model was utilized as an approximation.<sup>9,152</sup>

$$p(r) = \frac{3Ka}{2\pi R_{\text{eff}}} \left(1 - \frac{r^2}{a^2}\right)^{\frac{1}{2}} \quad \text{cf. ( 26 )}$$

$$\text{with } \frac{1}{K} = \frac{3}{4} \left( \frac{1 - \nu_{\text{particle}}^2}{E_{\text{particle}}} + \frac{1 - \nu_{\text{CP}}^2}{E_{\text{CP}}} \right) \quad \text{cf. ( 22 )}$$

$$\text{and } a^3 = \frac{R_{\text{eff}}}{K} F \quad \text{cf. ( 23 )}$$

To estimate the radial pressure distribution  $p(r)$ , the contact radius  $a$  was calculated for a load of  $F = 1 \mu\text{N}$ , assuming  $R_{\text{eff}}$  from the radii of the undeformed particle ( $R_{\text{particle}} = 80 \mu\text{m}$ ) and the CP ( $R_{\text{CP}} = 53 \mu\text{m}$ ),  $E_{\text{particle}} = 469 \text{ Pa}$  (as determined above), and  $\nu_{\text{particle}} = 0.5$  (as assumed in the mechanical characterization). The term comprising the elastic properties of the CP was neglected owing to its rigidity and comparably high elastic modulus.

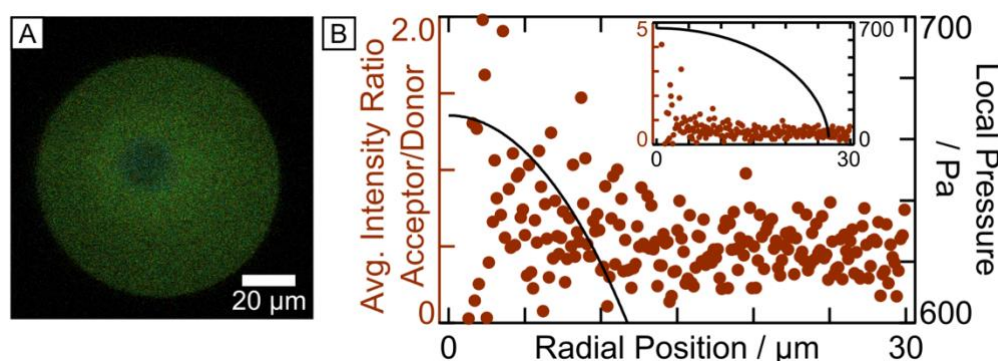


**Figure V-29.** (A) True color CLSM image of a hydrogel particle indented by a CP at  $1 \mu\text{N}$  load (cyan-blueish reflection of the apex). Analog to the previous evaluation, the fluorescence intensity of the donor and acceptor was averaged azimuthally as a radial function. Brightness and contrast were adjusted for illustration. (B) Ratio of the average fluorescence intensity of the acceptor and donor during CP indentation (dark red dots, left axis) in comparison with a calculated Hertz pressure profile under the CP apex (black line, right axis) with axes scaled for better visualization. The inset depicts the same plot in full scale of both data axes. Reprinted with permission and adapted from Neubauer et al.<sup>11</sup> Copyright American Chemical Society 2019.

Admittedly, assumptions of the Hertz model include a small contact area and small deformation and neglect adhesion so that the boundary conditions at the applied load are beyond these conditions. Despite this, the comparison of indentation with the large CP and the Hertz prediction from the determined elastic modulus has shown an acceptable agreement up to a load of  $1 \mu\text{N}$  (Figure V-18B). Assuming a Hertzian contact, the pressure at the CP apex could be approximated to the order of  $1 \text{ kPa}$  in the area with an observable shift in acceptor/donor intensity ratio (Figure V-29B). Although this approximation



deviates from the actual contact mechanics, this threshold stress allows to anticipate the stress resolution of the hydrogel particles be at least in the lower kPa range (1–10 kPa). The spatial resolution was determined by the fluorescence shift arising from the indentation of an AFM tip as a more localized mechanical trigger (Figure V-30). The indented pyramidal tip presented above in the concept scheme (Figure V-1D) is a sharp AFM probe, as usually used for conventional imaging. Here, the fluorescence response is strongly localized to the side of the indented tip. Hence, the spatial resolution must be on the lower micrometer scale.

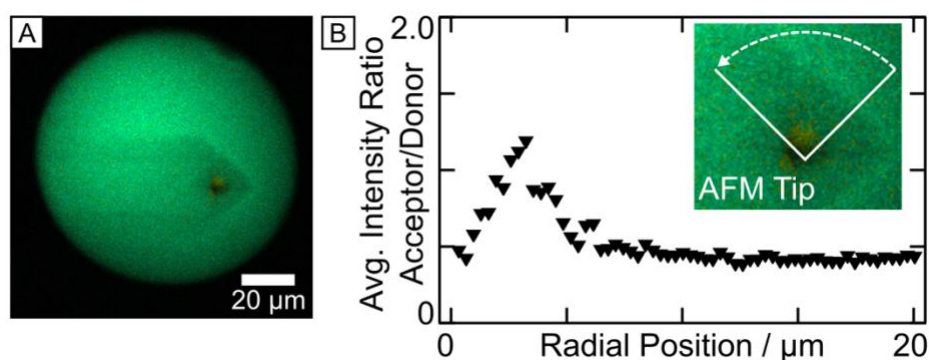


**Figure V-30.** (A) True color CLSM image of a hydrogel particle indented by an AFM tip (black triangle, the cantilever is visible as slight shade). Brightness and contrast were adjusted for illustration. (B) Ratio of the average fluorescence intensity of the acceptor and donor during CP indentation, corresponding to the white sketch marked in the inset. It denotes the circular section where the fluorescence intensity of the donor and acceptor was averaged azimuthally as a radial function. Reprinted with permission and adapted from Neubauer et al.<sup>11</sup> Copyright American Chemical Society 2019.

In the surrounding of the indented AFM imaging tip (black triangle), areas with shifted fluorescence appeared. In contrast to CP indentation, the fluorescence shift is not radially symmetrical around the tip (Figure V-30A and inset of B). On the one hand, the tip is not spherical but pyramidal. On the other hand, the cantilever can be slightly tilted from the manual mounting in the AFM and its inclination.<sup>122</sup> An area exhibiting a pronounced fluorescence shift was averaged azimuthally and evaluated, analog to the CP experiments. In the spatial acceptor/donor intensity ratio, a clear shift toward FRET acceptor fluorescence was found in close distance to the AFM tip.

Owing to the geometrical difference to a spherical probe, the higher localization of the fluorescence mechanoresponse may originate from the stronger localization of the mechanical interaction between the AFM tip and the hydrogel particle. Potential fluorescence artifacts from the cantilever tip can be ruled out, as the manufacturer of the cantilevers used (Nanosensors, Switzerland) is known for very low autofluorescence.<sup>305</sup>

---

## V.6. Conclusions

In conclusion, mechanoresponsive microscopic hydrogel particles were developed from PEG macromolecular precursors with defined chain length for a homogeneous network, following the blueprint of the Flory-Rehner theory. Fluorophores forming FRET pairs were connected to the hydrogel network structure for reporting global and local deformations of the polymer network *in situ* as fluorescence shifts.

Utilizing droplet microfluidics, hydrogel particles could be yielded from monodisperse microemulsion droplets of the PEG precursor solutions. Owing to the high reactivity of the precursor crosslinking reaction, adaptations of the microfluidic structure were required to prevent premature crosslinking of the precursor solutions, and to facilitate thorough mixing of the droplets. Besides variations in the microfluidic setup, the precursor system was varied in concentration, molecular architecture, and crosslinking chemistry for a homogeneous network formation in the hydrogel particles. Moreover, further subsequent crosslinking causing aggregation was to be prevented, e.g. by capping reactive groups.

In the concept, network deformations should be signaled by coupled FRET donor and acceptor molecules, causing a shift in fluorescence from donor toward stronger acceptor emission. Indeed, this could be observed when the network was collapsed after drying. Increasing the surrounding humidity in a controlled fashion, the fluorescence successively shifted back from FRET acceptor toward donor emission, signaling global network deformations induced from the swelling expansion. With a simplified model of one FRET pair at the termini of a single polymer chain, FRET pair distance distributions were calculated, explaining the humidity-dependent shift qualitatively.

The hydrogel particle response to mechanical stress was investigated in a combined CLSM-AFM setup. For observing a fluorescence response to mechanical stress, hydrogel particles were prepared with variations in network formation and fluorophore labeling. Whereas the collapse by drying usually led to the expected fluorescence shift for most particle variations, only one hydrogel particle variation was investigated in detail regarding its mechanoresponsiveness.

Colloidal Probe AFM (CP-AFM) was used for mechanical characterization of the mechanoresponsive hydrogel particles. With the Hertz model, an elastic modulus in the order of 0.5 kPa could be determined. Moreover, the force-deformation relation was investigated for these particles up to an indentation of approx. 70 % of the particle radius.

Both, the elastic properties and the behavior at large deformation are essential to understand the mechanical behavior of the hydrogel particles when aiming for predictable mechanics. For investigating the mechanoresponse, a mechanical load was applied with CP-AFM on the hydrogel particles while their fluorescence response was monitored with CLSM *in situ*. Observing the fluorescence shift on a global particle level, no correlation between the applied load and the intensity ratio FRET acceptor and donor emission was found when averaged over the whole particle. Owing to multiple excitation in a loading-unloading cycle, photobleaching of the donor was more pronounced than network responses in the acceptor/donor intensity ratio. An alternative approach for determining FRET would be to spatially resolve the lifetimes of the donor fluorophores in the system (e.g. FLIM, cf. Section III.3). This approach requires a combined AFM-FLIM instrumentation, but it could be a perspective to advance in this direction.

Evaluating the fluorescence intensity as a function of the distance from the center of the indented CP allowed to rule out the influence of photobleaching between successive images. With the FRET acceptor/donor intensity ratio shifted toward acceptor emission in close distance to the center, this finding clearly indicated the functionality of the network mechanoresponse. Comparing the mechanical characterization and the fluorescence response to mechanical loads, the stress resolution could be estimated to the lower kPa range (1-10 kPa). With non-elastic contributions increasing with large indentation, modeling of the acting stresses comprises complexities that might be tackled in future studies. Indenting an AFM imaging tip, the higher localization of mechanical stress allowed to determine the spatial resolution of the hydrogel network to be on the lower micrometer scale.

The rather simple material platform of these hydrogel particles allows altering of precursors and network density, which will in turn affect the mechanical properties, as demonstrated for macroscopic approaches.<sup>292</sup> Consequently, the mechanosensitivity could be adjusted by the sensitivity of fluorescence response via fluorophore concentration and donor/acceptor number ratio. Moreover, by increasing the polymer network density, the hydrogel is not only expected to be stiffer but also able to respond to smaller deformations. Further, by increasing the fluorophore concentration, the hydrogel could be expected to generate fluorescence response already at smaller deformations. In addition, by incorporating cell-binding sites, these hydrogel particles might serve as a general material platform for force sensing in mechanobiology.

---

## V.7. Experimental Details

### *Materials*

The photoresist SU-8 2050 with developer was purchased from Micro Resist Technology (Berlin, Germany). The Sylgard 184 kit was purchased from DowCorning (Midland, MI, USA). The fluorinated oils HFE-7500 and HFE-7100 were produced by 3M and purchased from IoLiTec (Heilbronn, Germany). (Tridecafluoro-1,1,2,2,-tetrahydrooctyl)-trichlorosilane was purchased from Gelest (Morrisville, PA, USA). Maleimide-PEG-maleimide (MW 5 kDa), 4-arm PEG thiol (MW 10 kDa), and 4-arm PEG maleimide (MW 10 kDa) were purchased from JenKem Technology (Plano, TX, USA). Alexa Fluor 488 C5 maleimide and Alexa Fluor 555 C2 maleimide were purchased from Thermo Fisher Scientific (Waltham, MA, USA). Maleimide, Phosphate buffered saline (PBS) tablets, mercaptopropyltrimethoxysilane, sodium chloride, and Hellmanex were purchased from Sigma-Aldrich. Perfluorooctanol was purchased from AlfaAesar. Lithium chloride was purchased from Merck. Potassium carbonate was purchased from Fluka. Ethanol (p.a. grade) was purchased from VWR International GmbH.

If not stated otherwise, the water used was purified with a microfiltration system (USF ELGA PureLab Plus).

### *Fabrication of Microfluidic Structures*

Microfluidic (MF) structures were fabricated combining photo- and soft lithography. The channel design was blueprinted with CAD (AutoCAD 2016, v. M.107.0.0) and plotted as a photomask. The positive of the structure was generated with photolithography, as described elsewhere.<sup>66</sup>

Briefly, a layer of a photoresist (SU-8 2050) was spin-coated on a silicon wafer, and illuminated through the photomask. After curing and developing, the positive of the MF structure could be molded by soft lithography using polydimethylsiloxane (PDMS, Sylgard 184, precursor-curing agent ratio 1:10) at a curing temperature of 65 °C for 2 h. The demolded structures and glass slides were activated in oxygen plasma and connected to close the negative structure. The MF channels were fluorinated by rinsing with a solution of (tridecafluoro-1,1,2,2,-tetrahydrooctyl)trichlorosilane in a fluorinated polyether (HFE-7500, 2 % (v/v) silane conc.).

### *Preparation of Hydrogel Particles*

The hydrogel particles were generated via droplet micro-fluidics and thermally elevated gelation of the precursor droplets.

For droplet MF, a ABA triblock surfactant consisting of two perfluoropolyether (PFPE) blocks and a poly(ethylene glycol) block<sup>294</sup> was supplied and dissolved in a fluorinated oil (HFE-7500, 2 wt. % surfactant conc.) as the continuous oil phase. For forming the hydrogels, precursor solutions of 4-arm PEG thiol (MW 10 kDa) and PEG(Maleimide)<sub>2</sub> (MW 5 kDa) in 1X PBS solution (4 wt. % each) were prepared. To the PEG thiol solution, the fluorophores Alexa Fluor 488 (FRET donor) and Alexa 555 (FRET acceptor) were added from stock solutions (1mg/mL) for attachment. As a matter of course, the PEG thiol had been dissolved in an accordingly smaller volume of PBS solution to reach the desired concentration after addition of the fluorophore solutions. The ratio of coupled donor and acceptor was 1:6 occupying approx. 1 % of the thiols.

For the particles in the humidity swelling experiments, solutions of 4-arm PEG thiol (MW 10 kDa) and 4-arm PEG maleimide (MW 10 kDa) (6 wt. % each) were used. The ratio of coupled donor and acceptor was 1:1 occupying 0.1% of the thiols.

The microfluidic conditions for generating the hydrogel particles were kept at a flow rate of 800  $\mu\text{L/h}$  for the continuous phase and 225  $\mu\text{L/h}$  for the dispersed phase (75  $\mu\text{L/h}$  each). Collected in vials, the droplet emulsions were shaken gently at elevated temperature (37 °C) for gelation overnight. For demulsification, the sedimented oil phase was removed and 1X PBS solution was added to the emulsion for phase transfer of the demulsified particles. The triblock copolymer surfactant was removed by a threefold extraction against perfluorooctanol in HFE-7100 (1:4 (v/v)). For the maleimide capping, an amount of maleimide (0.1 M, aqueous) was added in a tenfold excess of the original amount of thiol groups and left for one hour at elevated temperature (37 °C). Subsequently, the particle dispersion was sedimented gently (30 s, 1000 G rcf) so that one fourth of the dispersion volume could be removed from the supernatant and replaced with 1X PBS solution, in three repetitions altogether. With respect to the sensitivity of the fluorophores to light, the particle dispersions were stored in darkness.

### *Optical Characterization*

Conventional fluorescence microscopy was performed on DMI8 inverted microscope (Leica Microsystems, Germany) using a 10x air objective (NA 0.30) and a GFP filter set.

---

### *Mechanical Characterization*

For the mechanical characterization of the hydrogel particles, colloidal probe (CP) AFM was used. Tipless cantilevers (NSC 35 and CSC 37, without Al backside coating, MikroMasch, Tallinn, Estland) were calibrated with the thermal noise method.<sup>132</sup> Stöber silica particles (at CSC 37, 19.59  $\mu\text{m}$  diameter, microParticles, Germany) and glass beads (at NSC 35, 30-50  $\mu\text{m}$  diameter, Polysciences, Germany) were glued to the apex of the cantilever (NOA 63, Norland Products, USA) as spherical probes. As substrates, cover slips (35 mm diameter, 0.17 mm thickness, VWR) were functionalized with mercaptopropyltrimethoxysilane (MPTMS) to immobilize the hydrogel particles. Prior to the experiments, the cover slips were cleaned by ultrasonication in Hellmanex solution, water, and ethanol, successively. Blow-dried with nitrogen, they were cleaned further in oxygen plasma (SmartPlasma, plasma technology, Germany) for one minute (80 W, 0.2 mbar) and kept in a desiccator with MPTMS (10-20  $\mu\text{L}$ ) under reduced pressure for two hours. Afterwards, the substrates were rinsed with ethanol for removal of unbound silane. The AFM experiments were conducted with an MFP-3D (Asylum Research, USA) in a closed fluid cell. The cell was filled with 1X PBS solution. Then, a small amount of the particle dispersion (5  $\mu\text{L}$ ) was added and left for sedimentation and surface immobilization for at least 30 mins.

Freestanding particles (15 particles) were chosen randomly for mechanical characterization. A coarse optical alignment of the individual particles and the colloidal probe was followed by quick force-mapping of each particle apex for a finer alignment. On each particle, ten force-deformation curves were recorded (CSC 37).

For evaluation, the data was fitted with the Hertz model,<sup>148</sup> using Igor Pro 6 and a custom-made evaluation code<sup>306</sup> based on the fundamentals of force spectroscopy.<sup>122</sup> For fitting, an indentation range of up to 600-800 nm was used. Usually, only fits with a deviation of less than 5% from the expected Hertzian contact slope were considered.

The experiments at large deformations were conducted with a Nanowizard Ultra Speed AFM equipped with a CellHesion module (JPK Instruments, Germany) allowing large z-displacements (100  $\mu\text{m}$ ). Ten freestanding particles were chosen randomly and aligned optically with the glass bead colloidal probe (NSC 35). The force curves were driven to the maximal photodiode deflection of the setup (equivalent to approx. 2  $\mu\text{N}$  in this case). Using the manufacturer software (JPK DataProcessing), the deflection-displacement data was processed, and the contact point was determined to extract the deformation at certain forces.

### *Investigation of the Mechanical Response*

For correlating the fluorescence to mechanics, a combined setup of an Axio Observer Z.1 inverted microscope with an LSM710 confocal laser scanning module (Carl Zeiss Microscopy, Germany) and an MFP-3D AFM was used. The sample preparation was analog to the mechanical characterization. After calibration of the sensitivity on the bare substrate, the colloidal probe of the cantilever (glass bead at NSC 35) was aligned optically with the hydrogel particles. The illumination during the whole experiment was kept at minimum with respect to the light sensitivity of the fluorophores.

The applied loads on the particles were defined as approach setpoint so that the force was kept constant in a feedback loop. After approach to a particle, the load was increased successively, with further approach if necessary. At each load, the focus was set to the apex of the CP before the confocal image was taken.

For imaging, a 63x oil immersion objective (NA 1.25) was used. The donor was excited with an Ar laser (488 nm, 3.75 mW). The emission was detected spectrally resolved (9.8 nm resolution) resulting in a separate intensity image for each detected range. The pinhole was set to 1 AU. In case of the AFM tip indenting (PPP-NCHAuD, Nanosensors, Switzerland), the image was taken with a 20x air objective (NA 0.50), excited with an Ar laser (488 nm, 5 mW).

The data was evaluated in ImageJ 1.52e with the plugin Radial Profile Angle.

### *Investigation of the Humidity Response*

The humidity experiments were conducted on the same setup as the mechanoresponse experiments. A droplet of hydrogel particle dispersion was dispersed onto a glass slide and left in darkness for drying. For CLSM, the sample was kept in a sealed glass container flooded with an Ar gas stream to ensure complete drying. The images of dry particles were recorded immediately after complete drying. Using a 20x air objective (NA 0.50), the sample was excited with an Ar laser (488 nm, 0.5 mW). The emission was detected spectrally resolved (4.9 nm resolution). The pinhole was set to 1 AU. The humidity was increased gradually by the presence of saturated salt solutions (LiCl, K<sub>2</sub>CO<sub>3</sub>, and NaCl). After quickly exchanging the vial in the glass container, it was sealed again and left in darkness for at least 30 min to ensure equilibration before taking the according images. The data was evaluated in ImageJ 1.52e by determining the average intensity of the particles in the images detecting the according emission maxima of the fluorophores.

---



## VI. Outlook and Perspectives

---

## VI.1. Adaption of the Hydrogel Platform to an Application in Force Sensing

Having established to functionalize a hydrogel network for optical response to mechanical stress, two key challenges are deciding for applying the hydrogel network platform as a force sensor: the mechanics and the mechanoresponse have to be adapted to the sensitivity required for the application, and the purpose of application, defining the size, morphology, and functionalization of the hydrogel network.

Regarding the sensitivity of the mechanoresponse, the consideration to match mechanical properties of the sensor and sample, but also the sensitivity of detection is essential in any case of force sensing. For the hydrogel preparation, this involves matching the elasticity of the hydrogel with the forces the investigated actor is able to apply. Simultaneously, the hydrogel deformation caused by the investigated actor must be sufficient to induce an emission shift from coupled FRET pairs to localize and quantify the acting force.

With the presented hydrogel platform, several parameters are available to alter the network structure and density. By increasing the precursor concentration, a denser network could be expected. As a result, the elastic modulus of the hydrogel can be increased, as demonstrated by Phelps et al.<sup>292</sup> Moreover, they found differences in elastic modulus when varying crosslinking functionalities, indicating that the crosslinking reaction might as well have a significant effect on the resulting network.

In this study, the maleimide-thiol Michael addition was employed as crosslinking reaction almost exclusively. It was intended for a high crosslinking efficiency owing to its high reactivity.<sup>293</sup> Possibly, the homogeneity in building up the network could be improved by controlling the reaction kinetics with temperature or by switching to a different crosslinking reaction. In view of potential applications in mechanobiology, a bandwidth of bioorthogonal reactions is reported, for example by Azagarsamy and Anseth.<sup>97</sup>

Combining two or more addressable crosslinking reactions would increase the obtainable level of complexity. Extending the presented A-B type crosslinking scheme, another parallelized coupling reaction (C-D) could be utilized for coupling another type of precursor, as the architecture of these network building blocks obviously affects the achievable network structure. Moreover, parallelized coupling reactions could serve for addressing and positioning fluorophores or biological functionalities needed in application, for instance.

---

Conceptually, the deformation sensitivity of the mechanoresponse should be adjustable by the fluorophore concentration and the number ratio of FRET donor and acceptor. With a higher concentration, the overall number of fluorophores is increased so that their distance is statistically smaller. Hence, smaller network deformations are required for FRET. However, the donor emission is omnipresent in the image bearing the risk to overexpose the FRET acceptor emission which signals local network deformations. In analogy to a signal-to-noise ratio, the number ratio of the fluorophores could be adjusted in favor of the acceptor when increasing the fluorophore concentration to compensate this effect.

With respect to the purpose of application in cell biology, integrating biological functionalities will be required, as for example the RGD peptide as cell-binding motif. The influence of matrix mechanics on cell specification and differentiation is known for more than a decade.<sup>7</sup> This was considered in experimental design, for example, by encapsulating human mesenchymal stem cells (hMSCs) in hydrogel particles,<sup>76</sup> accounting for the three-dimensional cell environment in tissues. When inverting the concept from determining the influence of the matrix mechanics on the cells to determining the mechanical interactions of cells on their matrix, cells are investigated as force actors, requiring the RGD peptide as a binding site for cell integrins to firmly attach to the network. Encapsulating cells in mechanoresponsive hydrogel particles might then allow to investigate and quantify the mechanical interactions of cells with their matrix.

In this perspective, promising work has been reported by Headen et al.<sup>75</sup> With droplet microfluidics, they encapsulated hMSCs in hydrogel particles formed from a comparable PEG network functionalized with the RGD peptide. For seven days, they observed nearly full cell viability, compared to the initial cell viability.

Vice versa, various approaches were conducted to incorporate fluorescent droplets and particles in the cell environment to derive acting forces from changes in shape.<sup>294,307,308</sup> Accordingly, mechanoresponsive hydrogel particles could be adapted to such an application to enable FRET based localization of stress fields instead of shape-reconstruction based approaches.

Novel tissue engineering approaches are based on 3D printing of hydrogels.<sup>309</sup> In the same way, it is conceivable to add mechanoresponsive hydrogel particles to the bioink so that they can act as force sensors in the cell environment of the construct. Moreover, the optically readable mechanoresponse might assist in determining shear stress in the printing nozzle. This mechanical stress in the nozzle was identified as a deciding parameter for cell

survival during and after printing.<sup>310</sup> In this regard, models describing the deformation of cells during printing are developed by Stephan Gekle and coworkers.<sup>§</sup> In preliminary evaluation, good agreement was found between modeling and the experimental data from the mechanical characterization of the hydrogel particles in this thesis. Accordingly, this hydrogel particle platform might serve as sensors to read out shear stress in a printing nozzle *in situ*. In a further step, the presented mechanoresponse concept might be transferred from the particle concept to a hydrogel material system, e.g. for bioinks, enabling insight to tissue mechanics far above single particle scale.

Whereas the calibration of the hydrogel particles as shear stress sensors in the printing process could be feasible already by mimicking the nozzle geometry with microfluidics, the application of the hydrogel platform as force-sensing cell matrix will require an in-depth understanding of the network mechanics.

## VI.2. Approaches for Quantifying Stresses Acting in the Network

In the presented work, the mechanical properties of the mechanoresponsive hydrogel particles and the correlation of mechanical stress with optical response were evaluated in a first approximation with the Hertz model. To benchmark the capabilities of the hydrogel platform, the deformation caused by indenting spheres was described with classic contact mechanics models.

A sphere indented into a hydrogel network is loaded with a unidirectional force causing a three-dimensional stress field around the contact area. Considering an encapsulated cell within the hydrogel network, this actor might apply multidirectional forces on the network causing complex three-dimensional deformations of the hydrogel. At the latest, such complex situations might require computational modeling approaches to elucidate the acting mechanics.

The mechanics of such soft polymeric materials has been investigated combining experimental, analytical, and Finite Element Modeling (FEM) approaches. Based on classic contact mechanics, the transition to nonlinear, hyperelastic behavior at larger deformation

<sup>§</sup> In the scope of a collaborative research center of the German Research Foundation (DFG SFB/TRR 225 “Biofabrication”)

---

can be described.<sup>311</sup> Furthermore, hyperelastic parameters can be determined by modeling-supported indentation experiments.<sup>312,313</sup> Applying fluorescent droplets and particles as local stress sensors, as mentioned in the section above, FEM can be utilized to derive acting stresses from reconstructions of their deformed shape.<sup>307,308,314</sup>

These examples do not only indicate the feasibility of utilizing FEM for a detailed understanding of the mechanics triggering the mechanoresponse of the hydrogel particles, but also demonstrate the potential of FEM to elucidate more complex stress fields from an application in mechanobiology.

Whereas FEM might enable to advance in interpreting the mechanics of the hydrogel platform, it requires *in situ* 3D CLSM data of the deformed hydrogel. As the hydrogel deformation is observed from the emission of the FRET donor and acceptor, the optical information enables an insight to the mechanics acting on the network, and is the data base for modeling and interpretation, in the first place.

The confocal microscopy technique allows imaging of focal planes, comparable to slices of the object, that can be reconstructed to 3D models of the sample. For example, Böl et al.<sup>315</sup> used this approach to investigate the detachment of a biofilm. Moreover, 3D CLSM imaging proved its capabilities to capture wetting phenomena and dynamic rearrangements of granular particulate systems, as demonstrated by Auernhammer and coworkers.<sup>285,316</sup>

### VI.3. FRET for Sensing in Polymer Brushes

Bridging the concepts of the materials presented in this study, polymer brushes labeled with FRET pairs could combine a defined polymer structure with an optical response sensitive on the order of the brush thickness. Preliminary work on this topic has been started in collaboration with Rainer Jordan and coworkers.

For the mechanoresponsive polyelectrolyte brush presented in this study, a quenching mechanism was utilized to read out the conformational state of the polymer chains. The chains were labeled with fluorescein. The fluorescence of this dye is quenched upon complexation with the cationic charges of the polyelectrolyte. Mechanical compression of the polymer brush lead to an increase in quenching, notable by lower fluorescence intensity. Concurrently, the fluorophore is photobleached during illumination, simultaneously

decreasing fluorescence intensity. Moreover, this effect can hamper a quantitative calibration of the fluorescence intensity to defined loads.

Utilizing FRET pairs to quantify the brush conformation would offer an observable quantity that is less influenced by photobleaching. As FRET pair, fluorescein isothiocyanate (FITC) and trirhodamine isothiocyanate (TRITC) were employed. These fluorophores are comparable to the FRET pair used in the presented mechanoresponsive hydrogel.

In first preliminary approaches, polymer brushes from various monomers were tested for a response. Among them, also the monomer METAC, which was used for the experiments in this work, was polymerized to a brush structure and labeled with FITC and TRITC. It turned out that the cationic quenching mechanism depleted FRET in the investigated samples.

Nonetheless, also this concept is promising in regard to the variability of parameters for triggering a FRET mechanoresponse. Besides the type and charge of the monomer, the grafting density and brush thickness, the fluorophore concentration, and the FRET pair ratio are strongly influencing parameters to achieve and tune a FRET mechanoresponse in planar contact geometry.

---



# Bibliography

- (1) Lackner, J. R.; DiZio, P. Space Motion Sickness. *Exp Brain Res* **2006**, *175* (3), 377–399.
- (2) Van Zanten, A. T. Bosch ESP Systems: 5 Years of Experience; SAE International: 400 Commonwealth Drive, Warrendale, PA, United States, 2000; Vol. 1, pp 2000–01–1633.
- (3) Petruso, K. M. Early Weights and Weighing in Egypt and the Indus Valley. *M Bulletin Museum of Fine Arts, Boston* **1981**, *79*, 44–51.
- (4) International Bureau of Weights and Measures. *The International System of Units*; U.S. Dept. of Commerce, National Bureau of Standards, 1977.
- (5) Cheng, G.; Dean-Leon, E.; Bergner, F.; Olvera, J. R. G.; Leboutet, Q.; Mittendorfer, P. A Comprehensive Realization of Robot Skin: Sensors, Sensing, Control, and Applications. *Proceedings of the IEEE* **2019**, *107* (10), 2034–2051.
- (6) Binnig, G.; Quate, C. F. Atomic Force Microscope. *Phys. Rev. Lett.* **1986**, *56* (9), 930–933.
- (7) Engler, A. J.; Sen, S.; Sweeney, H. L.; Discher, D. E. Matrix Elasticity Directs Stem Cell Lineage Specification. *Cell* **2006**, *126* (4), 677–689.
- (8) Grashoff, C.; Hoffman, B. D.; Brenner, M. D.; Zhou, R.; Parsons, M.; Yang, M. T.; McLean, M. A.; Sligar, S. G.; Chen, C. S.; Ha, T.; et al. Measuring Mechanical Tension Across Vinculin Reveals Regulation of Focal Adhesion Dynamics. *Nature* **2010**, *466* (7303), 263–266.
- (9) Bünsow, J.; Erath, J.; Biesheuvel, P. M.; Fery, A.; Huck, W. T. S. Direct Correlation Between Local Pressure and Fluorescence Output in Mechanoresponsive Polyelectrolyte Brushes. *Angew. Chem. Int. Ed.* **2011**, *50* (41), 9629–9632.
- (10) Neubauer, J. W.; Xue, L.; Erath, J.; Drotlef, D.-M.; del Campo, A.; Fery, A. Monitoring the Contact Stress Distribution of Gecko-Inspired Adhesives Using Mechano-Sensitive Surface Coatings. *ACS Appl. Mater. Interfaces* **2016**, *8* (28), 17870–17877.
- (11) Neubauer, J. W.; Hauck, N.; Männel, M. J.; Seuss, M.; Fery, A.; Thiele, J. Mechanoresponsive Hydrogel Particles as a Platform for Three-Dimensional Force Sensing. *ACS Appl. Mater. Interfaces* **2019**, *11* (29), 26307–26313.
- (12) Strobl, G. *The Physics of Polymers*; Springer Berlin Heidelberg: Berlin, Heidelberg, 2007.
- (13) Fleer, G. J.; Stuart, M. A. C.; Scheutjens, J. M. H. M.; Cosgrove, T.; Vincent, B. *Polymers at Interfaces*; Springer Netherlands: Dordrecht, 1998.
- (14) Brittain, W. J.; Minko, S. A Structural Definition of Polymer Brushes. *J. Polym. Sci., Part A: Polym. Chem.* **2007**, *45* (16), 3505–3512.
- (15) Barbey, R.; Lavanant, L.; Paripovic, D.; Schüwer, N.; Sugnaux, C.; Tugulu, S.; Klok, H.-A. Polymer Brushes via Surface-Initiated Controlled Radical Polymerization: Synthesis, Characterization, Properties, and Applications. *Chem. Rev.* **2009**, *109* (11), 5437–5527.
- (16) Alexander, S. Adsorption of Chain Molecules with a Polar Head a Scaling Description. *J. Phys. France* **1977**, *38* (8), 983–987.
- (17) de Gennes, P. G. Conformations of Polymers Attached to an Interface. *Macromolecules* **1980**, *13* (5), 1069–1075.
- (18) Milner, S. T.; Witten, T. A.; Cates, M. E. A Parabolic Density Profile for Grafted Polymers. *Europhys. Lett.* **1988**, *5* (5), 413–418.
- (19) Milner, S. T.; Witten, T. A.; Cates, M. E. Theory of the Grafted Polymer Brush. *Macromolecules* **1988**, *21* (8), 2610–2619.
- (20) Zhulina, E. B.; Birshtein, T. M.; Borisov, O. V. Theory of Ionizable Polymer Brushes. *Macromolecules* **1995**, *28* (5), 1491–1499.
- (21) Henderson, L. J. Concerning the Relationship Between the Strength of Acids and Their Capacity to Preserve Neutrality. *American Journal of Physiology* **1908**, *21* (4), 173–179.
- (22) Hasselbalch, K. A. Die Berechnung der Wasserstoffzahl des Bluts aus der freien und gebundenen Kohlensäure desselben, und die Sauerstoffbindung des Bluts als Funktion der Wasserstoffzahl. *Biochemische Zeitschrift* **1917**, *78*, 112–144.
- (23) Biesalski, M.; Johannsmann, D.; Rühle, J. Synthesis and Swelling Behavior of a Weak Polyacid Brush. *J. Chem. Phys.* **2002**, *117* (10), 4988.
- (24) Zhulina, E. B.; Borisov, O. V. Structure and Interaction of Weakly Charged Polyelectrolyte Brushes: Self-Consistent Field Theory. *J. Chem. Phys.* **1997**, *107* (15), 5952.
- (25) Sidorenko, A.; Minko, S.; Schenk-Meuser, K.; Duschner, H.; Stamm, M. Switching of Polymer Brushes. *Langmuir* **1999**, *15* (24), 8349–8355.
- (26) Milner, S. T. Polymer Brushes. *Science* **1991**, *251* (4996), 905–914.

- (27) Farhan, T.; Azzaroni, O.; Huck, W. T. S. AFM Study of Cationically Charged Polymer Brushes: Switching Between Soft and Hard Matter. *Soft Matter* **2005**, *1* (1), 66–68.
- (28) Azzaroni, O.; Brown, A. A.; Huck, W. T. S. Tunable Wettability by Clicking Counterions Into Polyelectrolyte Brushes. *Adv. Mater.* **2007**, *19* (1), 151–154.
- (29) Liu, X.; Ye, Q.; Yu, B.; Liang, Y.; Liu, W.; Zhou, F. Switching Water Droplet Adhesion Using Responsive Polymer Brushes. *Langmuir* **2010**, *26* (14), 12377–12382.
- (30) Raftari, M.; Zhang, Z.; Carter, S. R.; Leggett, G. J.; Geoghegan, M. Frictional Properties of a Polycationic Brush. *Soft Matter* **2014**.
- (31) Kumar Vyas, M.; Schneider, K.; Nandan, B.; Stamm, M. Switching of Friction by Binary Polymer Brushes. *Soft Matter* **2008**, *4* (5), 1024–1032.
- (32) Synytska, A.; Svetushkina, E.; Pureskiy, N.; Stoychev, G.; Berger, S.; Ionov, L.; Bellmann, C.; Eichhorn, K. J.; Stamm, M. Biocompatible Polymeric Materials with Switchable Adhesion Properties. *Soft Matter* **2010**, *6* (23), 5907.
- (33) Wischerhoff, E.; Uhlig, K.; Lankenau, A.; Börner, H. G.; Laschewsky, A.; Duschl, C.; Lutz, J.-F. Controlled Cell Adhesion on PEG-Based Switchable Surfaces. *Angew. Chem. Int. Ed.* **2008**, *47* (30), 5666–5668.
- (34) Zhou, F.; Huck, W. T. S. Surface Grafted Polymer Brushes as Ideal Building Blocks for “Smart” Surfaces. *Phys. Chem. Chem. Phys.* **2006**, *8* (33), 3815–3823.
- (35) Uhlmann, P.; Merlitz, H.; Sommer, J.-U.; Stamm, M. Polymer Brushes for Surface Tuning. *Macromol. Rapid Commun.* **2009**, *30* (9–10), 732–740.
- (36) Block, S.; Helm, C. A. Conformation of Poly(Styrene Sulfonate) Layers Physisorbed From High Salt Solution Studied by Force Measurements on Two Different Length Scales. *J. Phys. Chem. B* **2008**, *112* (31), 9318–9327.
- (37) Rauch, S.; Eichhorn, K. J.; Kuckling, D.; Stamm, M.; Uhlmann, P. Chain Extension of Stimuli-Responsive Polymer Brushes: a General Strategy to Overcome the Drawbacks of the “Grafting-to” Approach. *Adv. Funct. Mater.* **2013**, *23* (45), 5675–5681.
- (38) Pettersson, T.; Naderi, A.; Makuška, R.; Claesson, P. M. Lubrication Properties of Bottle-Brush Polyelectrolytes: an AFM Study on the Effect of Side Chain and Charge Density. *Langmuir* **2008**, *24* (7), 3336–3347.
- (39) Gunkel, G.; Weinhart, M.; Becherer, T.; Haag, R.; Huck, W. T. S. Effect of Polymer Brush Architecture on Antibiofouling Properties. *Biomacromolecules* **2011**, *12* (11), 4169–4172.
- (40) Chen, T.; Amin, I.; Jordan, R. Patterned Polymer Brushes. *Chem. Soc. Rev.* **2012**, *41* (8), 3280–17.
- (41) Xu, C.; Wu, T.; Drain, C. M.; Batteas, J. D.; Fasolka, M. J.; Beers, K. L. Effect of Block Length on Solvent Response of Block Copolymer Brushes: Combinatorial Study with Block Copolymer Brush Gradients. *Macromolecules* **2006**, *39* (9), 3359–3364.
- (42) Wu, T.; Gong, P.; Szleifer, I.; Vlček, P.; Šubr, V.; Genzer, J. Behavior of Surface-Anchored Poly(Acrylic Acid) Brushes with Grafting Density Gradients on Solid Substrates: 1. Experiment. *Macromolecules* **2007**, *40* (24), 8756–8764.
- (43) Steenackers, M.; Küller, A.; Ballav, N.; Zharnikov, M.; Grunze, M.; Jordan, R. Morphology Control of Structured Polymer Brushes. *Small* **2007**, *3* (10), 1764–1773.
- (44) Steenackers, M.; Küller, A.; Stoycheva, S.; Grunze, M.; Jordan, R. Structured and Gradient Polymer Brushes From Biphenylthiol Self-Assembled Monolayers by Self-Initiated Photografting and Photopolymerization (SIPGP). *Langmuir* **2009**, *25* (4), 2225–2231.
- (45) Mansky, P.; Liu, Y.; Huang, E.; Russell, T. P.; Hawker, C. Controlling Polymer-Surface Interactions with Random Copolymer Brushes. *Science* **1997**, *275* (5305), 1458–1460.
- (46) Erath, J.; Cui, J.; Schmid, J.; Kappl, M.; del Campo, A.; Fery, A. Phototunable Surface Interactions. *Langmuir* **2013**, *29* (39), 12138–12144.
- (47) Bünsow, J.; Kelby, T. S.; Huck, W. T. S. Polymer Brushes: Routes Toward Mechanosensitive Surfaces. *Acc. Chem. Res.* **2010**, *43* (3), 466–474.
- (48) Heida, T.; Neubauer, J. W.; Seuss, M.; Hauck, N.; Thiele, J.; Fery, A. Mechanically Defined Microgels by Droplet Microfluidics. *Macromol. Chem. Phys.* **2017**, *218*, 1600418.
- (49) Flory, P. J.; Rehner, J. Statistical Mechanics of Cross-Linked Polymer Networks I. Rubberlike Elasticity. *J. Chem. Phys.* **1943**, *11* (11), 512–10.
- (50) Flory, P. J.; Rehner, J., Jr. Statistical Mechanics of Cross-Linked Polymer Networks II. Swelling. *The Journal of Chemical Physics* **1943**, *11* (11), 521–526.
- (51) Flory, P. J. *Principles of Polymer Chemistry*; Cornell University Press: Ithaca, New York, 1953; pp 1–687.
- (52) Flory, P. J. Statistical Mechanics of Swelling of Network Structures. *The Journal of Chemical Physics* **1950**, *18* (1), 108–111.

- (53) Peppas, N. A.; Merrill, E. W. Crosslinked Poly(Vinyl Alcohol) Hydrogels as Swollen Elastic Networks. *J. Appl. Polym. Sci.* **1977**, *21* (7), 1763–1770.
- (54) Hong, W.; Liu, Z.; Suo, Z. Inhomogeneous Swelling of a Gel in Equilibrium with a Solvent and Mechanical Load. *Int. J. Solids Struct.* **2009**, *46* (17), 3282–3289.
- (55) Brannon-Peppas, L.; Peppas, N. A. Equilibrium Swelling Behavior of pH-Sensitive Hydrogels. *Chemical Engineering Science* **1991**, *46* (3), 715–722.
- (56) Akagi, Y.; Gong, J. P.; Chung, U.-I.; Sakai, T. Transition Between Phantom and Affine Network Model Observed in Polymer Gels with Controlled Network Structure. *Macromolecules* **2013**, *46* (3), 1035–1040.
- (57) *Physical Properties of Polymers Handbook*; Mark, J. E., Ed.; Springer Science: New York, NY, 2007; pp 1–1050.
- (58) James, H. M.; Guth, E. Theory of the Increase in Rigidity of Rubber During Cure. *The Journal of Chemical Physics* **1947**, *15* (9), 669–683.
- (59) Peppas, N. A.; Bures, P.; Leobandung, W.; Ichikawa, H. Hydrogels in Pharmaceutical Formulations. *European Journal of Pharmaceutics and Biopharmaceutics* **2000**, *50* (1), 27–46.
- (60) van der Sman, R. G. M. Biopolymer Gel Swelling Analysed with Scaling Laws and Flory-Rehner Theory. *Food hydrocolloids* **2015**, *48* (C), 94–101.
- (61) Di Lorenzo, F.; Hellwig, J.; Klitzing, von, R.; Seiffert, S. Macroscopic and Microscopic Elasticity of Heterogeneous Polymer Gels. *ACS Macro Lett.* **2015**, *4* (7), 698–703.
- (62) Whitesides, G. M. The Origins and the Future of Microfluidics. *Nature* **2006**, *442* (7101), 368–373.
- (63) Terry, S. C.; Jerman, J. H.; Angell, J. B. A Gas Chromatographic Air Analyzer Fabricated on a Silicon Wafer. *IEEE Transactions on Electron Devices* **1979**, *26* (12), 1880–1886.
- (64) Seemann, R.; Brinkmann, M.; Pfohl, T.; Herminghaus, S. Droplet Based Microfluidics. *Rep. Prog. Phys.* **2012**, *75* (1), 016601.
- (65) Mashaghi, S.; Abbaspourad, A.; Weitz, D. A.; van Oijen, A. M. Droplet Microfluidics: a Tool for Biology, Chemistry and Nanotechnology. *Trends in Analytical Chemistry* **2016**, *82* (C), 118–125.
- (66) Wolfe, D. B.; Qin, D.; Whitesides, G. M. Rapid Prototyping of Microstructures by Soft Lithography for Biotechnology. In *Microengineering in Biotechnology*; Methods in Molecular Biology; Humana Press, Totowa, NJ: Totowa, NJ, 2010; Vol. 583, pp 81–107.
- (67) Xia, Y.; Whitesides, G. M. Soft Lithography. *Angew. Chem. Int. Ed. Engl.* **1998**, *37* (5), 550–575.
- (68) Choi, C.-H.; Wang, H.; Lee, H.; Kim, J. H.; Zhang, L.; Mao, A.; Mooney, D. J.; Weitz, D. A. One-Step Generation of Cell-Laden Microgels Using Double Emulsion Drops with a Sacrificial Ultra-Thin Oil Shell. *Lab Chip* **2016**, *16* (9), 1549–1555.
- (69) Männel, M. J.; Selzer, L.; Bernhardt, R.; Thiele, J. Optimizing Process Parameters in Commercial Micro-Stereolithography for Forming Emulsions and Polymer Microparticles in Nonplanar Microfluidic Devices. *Adv. Mater. Technol.* **2019**, *35*, 1800408.
- (70) Nunes, J. K.; Tsai, S. S. H.; Wan, J.; Stone, H. A. Dripping and Jetting in Microfluidic Multiphase Flows Applied to Particle and Fibre Synthesis. *J. Phys. D: Appl. Phys.* **2013**, *46* (11), 114002.
- (71) Kumacheva, E.; Garstecki, P. Formation of Droplets in Microfluidic Systems. In *Microfluidic Reactors for Polymer Particles*; John Wiley & Sons, Ltd: Chichester, UK, 2011; Vol. 80, pp 41–94.
- (72) Lück, S.; Schubel, R.; Rüb, J.; Hahn, D.; Mathieu, E.; Zimmermann, H.; Scharnweber, D.; Werner, C.; Pautot, S.; Jordan, R. Tailored and Biodegradable Poly(2-Oxazoline) Microbeads as 3D Matrices for Stem Cell Culture in Regenerative Therapies. *Biomaterials* **2016**, *79* (c), 1–14.
- (73) Hackelbusch, S.; Rossow, T.; Steinhilber, D.; Weitz, D. A.; Seiffert, S. Hybrid Microgels with Thermo-Tunable Elasticity for Controllable Cell Confinement. *Adv. Healthcare Mater.* **2015**, *4* (12), 1841–1848.
- (74) Rossow, T.; Bayer, S.; Albrecht, R.; Tzschucke, C. C.; Seiffert, S. Supramolecular Hydrogel Capsules Based on PEG: a Step Toward Degradable Biomaterials with Rational Design. *Macromol. Rapid Commun.* **2013**, *34* (17), 1401–1407.
- (75) Headen, D. M.; Aubry, G.; Lu, H.; García, A. J. Microfluidic-Based Generation of Size-Controlled, Biofunctionalized Synthetic Polymer Microgels for Cell Encapsulation. *Adv. Mater.* **2014**, *26* (19), 3003–3008.
- (76) Ma, Y.; Neubauer, M. P.; Thiele, J.; Fery, A.; Huck, W. T. S. Artificial Microniches for Probing Mesenchymal Stem Cell Fate in 3D. *Biomater. Sci.* **2014**, *2* (11), 1661–1671.

- (77) Shimanovich, U.; Efimov, I.; Mason, T. O.; Flagmeier, P.; Buell, A. K.; Gedanken, A.; Linse, S.; Åkerfeldt, K. S.; Dobson, C. M.; Weitz, D. A.; et al. Protein Microgels From Amyloid Fibril Networks. *ACS Nano* **2015**, *9* (1), 43–51.
- (78) Chau, M.; Abolhasani, M.; Thérien-Aubin, H.; Li, Y.; Wang, Y.; Velasco, D.; Tumarkin, E.; Ramachandran, A.; Kumacheva, E. Microfluidic Generation of Composite Biopolymer Microgels with Tunable Compositions and Mechanical Properties. *Biomacromolecules* **2014**, *15* (7), 2419–2425.
- (79) Holtze, C.; Rowat, A. C.; Agresti, J. J.; Hutchison, J. B.; Angilè, F. E.; Schmitz, C. H. J.; Köster, S.; Duan, H.; Humphry, K. J.; Scanga, R. A.; et al. Biocompatible Surfactants for Water-in-Fluorocarbon Emulsions. *Lab Chip* **2008**, *8* (10), 1632.
- (80) Clausell-Tormos, J.; Lieber, D.; Baret, J.-C.; Harrak, El, A.; Miller, O. J.; Frenz, L.; Blouwolff, J.; Humphry, K. J.; Köster, S.; Duan, H.; et al. Droplet-Based Microfluidic Platforms for the Encapsulation and Screening of Mammalian Cells and Multicellular Organisms. *Chemistry & Biology* **2008**, *15* (5), 427–437.
- (81) Rhee, M.; Burns, M. A. Drop Mixing in a Microchannel for Lab-on-a-Chip Platforms. *Langmuir* **2008**, *24* (2), 590–601.
- (82) Song, H.; Tice, J. D.; Ismagilov, R. F. A Microfluidic System for Controlling Reaction Networks in Time. *Angew. Chem. Int. Ed. Engl.* **2003**, *42* (7), 768–772.
- (83) Tice, J. D.; Song, H.; Lyon, A. D.; Ismagilov, R. F. Formation of Droplets and Mixing in Multiphase Microfluidics at Low Values of the Reynolds and the Capillary Numbers. *Langmuir* **2003**, *19* (22), 9127–9133.
- (84) Bringer, M. R.; Gerdt, C. J.; Song, H.; Tice, J. D.; Ismagilov, R. F. Microfluidic Systems for Chemical Kinetics That Rely on Chaotic Mixing in Droplets. *Phil. Trans. R. Soc. Lond. A* **2004**, *362* (1818), 1087–1104.
- (85) Stone, Z. B.; Stone, H. A. Imaging and Quantifying Mixing in a Model Droplet Micromixer. *Physics of Fluids* **2005**, *17* (6), 063103.
- (86) Liao, A.; Karnik, R.; Majumdar, A.; Cate, J. H. D. Mixing Crowded Biological Solutions in Milliseconds. *Anal. Chem.* **2005**, *77* (23), 7618–7625.
- (87) Tung, K.-Y.; Li, C.-C.; Yang, J.-T. Mixing and Hydrodynamic Analysis of a Droplet in a Planar Serpentine Micromixer. *Microfluid. Nanofluid.* **2009**, *7* (4), 545–557.
- (88) Kumachev, A.; Greener, J.; Tumarkin, E.; Eiser, E.; Zandstra, P. W.; Kumacheva, E. High-Throughput Generation of Hydrogel Microbeads with Varying Elasticity for Cell Encapsulation. *Biomaterials* **2011**, *32* (6), 1477–1483.
- (89) Theberge, A. B.; Mayot, E.; Harrak, El, A.; Kleinschmidt, F.; Huck, W. T. S.; Griffiths, A. D. Microfluidic Platform for Combinatorial Synthesis in Picolitre Droplets. *Lab Chip* **2012**, *12* (7), 1320–1326.
- (90) Thiele, J.; Ma, Y.; Foscchepoth, D.; Hansen, M. M. K.; Steffen, C.; Heus, H. A.; Huck, W. T. S. DNA-Functionalized Hydrogels for Confined Membrane-Free in Vitro Transcription/Translation. *Lab Chip* **2014**, *14* (15), 2651–2656.
- (91) Akartuna, I.; Aubrecht, D. M.; Kodger, T. E.; Weitz, D. A. Chemically Induced Coalescence in Droplet-Based Microfluidics. *Lab Chip* **2015**, *15* (4), 1140–1144.
- (92) Murray, M. J.; Snowden, M. J. The Preparation, Characterisation and Applications of Colloidal Microgels. *Adv. Colloid Interface Sci.* **1995**, *54*, 73–91.
- (93) Pich, A.; Richtering, W. Microgels by Precipitation Polymerization: Synthesis, Characterization, and Functionalization. In *Chemical Design of Responsive Microgels*; Pich, A., Richtering, W., Eds.; Advances in Polymer Science; Springer Berlin Heidelberg: Berlin, Heidelberg, 2010; Vol. 234, pp 1–37.
- (94) Lindemann, B.; Schröder, U. P.; Oppermann, W. Influence of the Cross-Linker Reactivity on the Formation of Inhomogeneities in Hydrogels. *Macromolecules* **1997**, *30* (14), 4073–4077.
- (95) Orakdogan, N.; Okay, O. Correlation Between Crosslinking Efficiency and Spatial Inhomogeneity in Poly(Acrylamide) Hydrogels. *Polym. Bull.* **2006**, *57* (5), 631–641.
- (96) Ma, S.; Natoli, M.; Liu, X.; Neubauer, M. P.; Watt, F. M.; Fery, A.; Huck, W. T. S. Monodisperse Collagen–Gelatin Beads as Potential Platforms for 3D Cell Culturing. *J. Mater. Chem. B* **2013**, *1* (38), 5128–5129.
- (97) Azagarsamy, M. A.; Anseth, K. S. Bioorthogonal Click Chemistry: an Indispensable Tool to Create Multifaceted Cell Culture Scaffolds. *ACS Macro Lett.* **2013**, *2* (1), 5–9.
- (98) Allazetta, S.; Hausherr, T. C.; Lutolf, M. P. Microfluidic Synthesis of Cell-Type-Specific Artificial Extracellular Matrix Hydrogels. *Biomacromolecules* **2013**, *14* (4), 1122–1131.

- (99) Rossow, T.; Heyman, J. A.; Ehrlicher, A. J.; Langhoff, A.; Weitz, D. A.; Haag, R.; Seiffert, S. Controlled Synthesis of Cell-Laden Microgels by Radical-Free Gelation in Droplet Microfluidics. *J. Am. Chem. Soc.* **2012**, *134* (10), 4983–4989.
- (100) Steinhilber, D.; Rossow, T.; Wedepohl, S.; Paulus, F.; Seiffert, S.; Haag, R. A Microgel Construction Kit for Bioorthogonal Encapsulation and pH-Controlled Release of Living Cells. *Angew. Chem. Int. Ed.* **2013**, *52* (51), 13538–13543.
- (101) Appel, E. A.; del Barrio, J.; Loh, X. J.; Scherman, O. A. Supramolecular Polymeric Hydrogels. *Chem. Soc. Rev.* **2012**, *41* (18), 6195–20.
- (102) Bastings, M. M. C.; Koudstaal, S.; Kieltyka, R. E.; Nakano, Y.; Pape, A. C. H.; Feyen, D. A. M.; van Slochteren, F. J.; Doevendans, P. A.; Sluijter, J. P. G.; Meijer, E. W.; et al. A Fast pH-Switchable and Self-Healing Supramolecular Hydrogel Carrier for Guided, Local Catheter Injection in the Infarcted Myocardium. *Adv. Healthcare Mater.* **2013**, *3* (1), 70–78.
- (103) Martino, C.; Lee, T. Y.; Kim, S.-H.; deMello, A. J. Microfluidic Generation of PEG-B-PLA Polymersomes Containing Alginate-Based Core Hydrogel. *Biomicrofluidics* **2015**, *9* (2), 024101–024109.
- (104) Henke, S.; Leijten, J.; Kemna, E.; Neubauer, M.; Fery, A.; van den Berg, A.; van Apeldoorn, A.; Karperien, M. Enzymatic Crosslinking of Polymer Conjugates Is Superior Over Ionic or UV Crosslinking for the on-Chip Production of Cell-Laden Microgels. *Macromolecular Bioscience* **2016**, 1–9.
- (105) Thiele, J.; Ma, Y.; Bruekers, S. M. C.; Ma, S.; Huck, W. T. S. 25th Anniversary Article: Designer Hydrogels for Cell Cultures: a Materials Selection Guide. *Adv. Mater.* **2013**, *26* (1), 125–148.
- (106) Velasco, D.; Tumarkin, E.; Kumacheva, E. Microfluidic Encapsulation of Cells in Polymer Microgels. *Small* **2012**, *8* (11), 1633–1642.
- (107) Annabi, N.; Tamayol, A.; Uquillas, J. A.; Akbari, M.; Bertassoni, L. E.; Cha, C.; Camci-Unal, G.; Dokmeci, M. R.; Peppas, N. A.; Khademhosseini, A. 25th Anniversary Article: Rational Design and Applications of Hydrogels in Regenerative Medicine. *Adv. Mater.* **2013**, *26* (1), 85–124.
- (108) Seuss, M.; Schmolke, W.; Drechsler, A.; Fery, A.; Seiffert, S. Core–Shell Microgels with Switchable Elasticity at Constant Interfacial Interaction. *ACS Appl. Mater. Interfaces* **2016**, *8* (25), 16317–16327.
- (109) Seiffert, S.; Thiele, J.; Abate, A. R.; Weitz, D. A. Smart Microgel Capsules From Macromolecular Precursors. *J. Am. Chem. Soc.* **2010**, *132* (18), 6606–6609.
- (110) Hu, Y.; Pérez-Mercader, J. Microfluidics Fabrication of Self-Oscillating Microgel Clusters with Tailored Temperature-Responsive Properties Using Polymersomes as “Microreactors.” *Langmuir* **2017**, *33* (49), 14058–14065.
- (111) Haefner, S.; Koerbitz, R.; Frank, P.; Elstner, M.; Richter, A. High Integration of Microfluidic Circuits Based on Hydrogel Valves for MEMS Control. *Adv. Mater. Technol.* **2017**, *3* (1), 1700108–1700110.
- (112) Jadhav, A. D.; Yan, B.; Luo, R.-C.; Wei, L.; Zhen, X.; Chen, C.-H.; Shi, P. Photoresponsive Microvalve for Remote Actuation and Flow Control in Microfluidic Devices. *Biomicrofluidics* **2015**, *9* (3), 034114–13.
- (113) Ma, C.; Lu, W.; Yang, X.; He, J.; Le, X.; Wang, L.; Zhang, J.; Serpe, M. J.; Huang, Y.; Chen, T. Bioinspired Anisotropic Hydrogel Actuators with on-Off Switchable and Color-Tunable Fluorescence Behaviors. *Adv. Funct. Mater.* **2017**, *28* (7), 1704568–7.
- (114) Kim, Y.; Kim, D.; Jang, G.; Kim, J.; Lee, T. S. Fluorescent, Stimuli-Responsive, Crosslinked PNIPAM-Based Microgel. *Sensors and Actuators B: Chemical* **2015**, *207*, 623–630.
- (115) Hassanzadeh, P.; Kazemzadeh-Narbat, M.; Rosenzweig, R.; Zhang, X.; Khademhosseini, A.; Annabi, N.; Rolandi, M. Ultrastrong and Flexible Hybrid Hydrogels Based on Solution Self-Assembly of Chitin Nanofibers in Gelatin Methacryloyl (GelMA). *J. Mater. Chem. B* **2016**, *4* (15), 2539–2543.
- (116) Fang, J.; Mehlich, A.; Koga, N.; Huang, J.; Koga, R.; Gao, X.; Hu, C.; Jin, C.; Rief, M.; Kast, J.; et al. Forced Protein Unfolding Leads to Highly Elastic and Tough Protein Hydrogels. *Nat. Commun.* **2013**, *4* (1), 47.
- (117) Chau, M.; De France, K. J.; Kopera, B.; Machado, V. R.; Rosenfeldt, S.; Reyes, L.; Chan, K. J. W.; Förster, S.; Cranston, E. D.; Hoare, T.; et al. Composite Hydrogels with Tunable Anisotropic Morphologies and Mechanical Properties. *Chem. Mater.* **2016**, *28* (10), 3406–3415.
- (118) Coutinho, D. F.; Sant, S. V.; Shin, H.; Oliveira, J. T.; Gomes, M. E.; Neves, N. M.; Khademhosseini, A.; Reis, R. L. Modified Gellan Gum Hydrogels with Tunable Physical and Mechanical Properties. *Biomaterials* **2010**, *31* (29), 7494–7502.

- (119) Elmalem, E.; Biedermann, F.; Scherer, M. R. J.; Koutsoubas, A.; Toprakcioglu, C.; Biffi, G.; Huck, W. T. S. Mechanically Strong, Fluorescent Hydrogels From Zwitterionic, Fully  $\Pi$ -Conjugated Polymers. *Chem. Commun.* **2014**, 50 (64), 8930–8933.
- (120) Kouwer, P. H. J.; Koepf, M.; Le Sage, V. A. A.; Jaspers, M.; van Buul, A. M.; Eksteen-Akeroyd, Z. H.; Woltinge, T.; Schwartz, E.; Kitto, H. J.; Hoogenboom, R.; et al. Responsive Biomimetic Networks From Polyisocyanopeptide Hydrogels. *Nature* **2013**, 493 (7434), 651–655.
- (121) Kirch, J.; Schneider, A.; Abou, B.; Hopf, A.; Schaefer, U. F.; Schneider, M.; Schall, C.; Wagner, C.; Lehr, C. M. Optical Tweezers Reveal Relationship Between Microstructure and Nanoparticle Penetration of Pulmonary Mucus. *PNAS* **2012**, 109 (45), 18355–18360.
- (122) Butt, H.-J.; Cappella, B.; Kappl, M. Force Measurements with the Atomic Force Microscope: Technique, Interpretation and Applications. *Surface Science Reports* **2005**, 59 (1-6), 1–152.
- (123) Meyer, E. Atomic Force Microscopy. *Progress in Surface Science* **1992**, 41 (1), 3–49.
- (124) Behrend, O. P.; Oulevey, F.; Gourdon, D.; Dupas, E.; Kulik, A. J.; Gremaud, G.; Burnham, N. A. Intermittent Contact: Tapping or Hammering? *Appl. Phys. A* **1998**, 66 (1), S219–S221.
- (125) Giessibl, F. J. Advances in Atomic Force Microscopy. *Reviews of Modern Physics* **2003**, 75 (3), 949–983.
- (126) McLean, R. S.; Sauer, B. B. Tapping-Mode AFM Studies Using Phase Detection for Resolution of Nanophases in Segmented Polyurethanes and Other Block Copolymers. *Macromolecules* **1997**, 30 (26), 8314–8317.
- (127) Nonnenmacher, M.; O'Boyle, M. P.; Wickramasinghe, H. K. Kelvin Probe Force Microscopy. *Appl. Phys. Lett.* **1991**, 58 (25), 2921–2924.
- (128) Melitz, W.; Shen, J.; Kummel, A. C.; Lee, S. Kelvin Probe Force Microscopy and Its Application. *Surface Science Reports* **2011**, 66 (1), 1–27.
- (129) Berger, R.; Butt, H.-J.; Retschke, M. B.; Weber, S. A. L. Electrical Modes in Scanning Probe Microscopy. *Macromol. Rapid Commun.* **2009**, 30 (14), 1167–1178.
- (130) Dendisová, M.; Jenišťová, A.; Parchaňská-Kokaislová, A.; Matějka, P.; Prokopec, V.; Švecová, M. The Use of Infrared Spectroscopic Techniques to Characterize Nanomaterials and Nanostructures: a Review. *Analytica Chimica Acta* **2018**, 1031, 1–14.
- (131) Munz, M. Force Calibration in Lateral Force Microscopy: a Review of the Experimental Methods. *J. Phys. D: Appl. Phys.* **2010**, 43 (6), 063001.
- (132) Hutter, J. L.; Bechhoefer, J. Calibration of Atomic-Force Microscope Tips. *Rev. Sci. Instrum.* **1993**, 64 (7), 1868.
- (133) Sader, J. E.; Chon, J. W. M.; Mulvaney, P. Calibration of Rectangular Atomic Force Microscope Cantilevers. *Rev. Sci. Instrum.* **1999**, 70 (10), 3967.
- (134) Cleveland, J. P.; Manne, S.; Bocek, D.; Hansma, P. K. A Nondestructive Method for Determining the Spring Constant of Cantilevers for Scanning Force Microscopy. *Rev. Sci. Instrum.* **1993**, 64 (2), 403.
- (135) Derjaguin, B. Untersuchungen Über Die Reibung Und Adhäsion, IV. *Kolloid Zeitschrift* **1934**, 69 (2), 155–164.
- (136) Ducker, W. A.; Senden, T. J.; Pashley, R. M. Direct Measurement of Colloidal Forces Using an Atomic Force Microscope. *Nature* **1991**, 353 (6341), 239–241.
- (137) Butt, H.-J. Measuring Electrostatic, Van Der Waals, and Hydration Forces in Electrolyte Solutions with an Atomic Force Microscope. *Biophys. J.* **1991**, 60 (6), 1438–1444.
- (138) Trefalt, G.; Palberg, T.; Borkovec, M. Forces Between Colloidal Particles in Aqueous Solutions Containing Monovalent and Multivalent Ions. *Curr. Opin. Colloid Interface Sci.* **2017**, 27, 9–17.
- (139) Borkovec, M.; Papastavrou, G. Interactions Between Solid Surfaces with Adsorbed Polyelectrolytes of Opposite Charge. *Curr. Opin. Colloid Interface Sci.* **2008**, 13 (6), 429–437.
- (140) Kuznetsov, V.; Papastavrou, G. Ion Adsorption on Modified Electrodes as Determined by Direct Force Measurements Under Potentiostatic Control. *J. Phys. Chem. C* **2014**, 118 (5), 2673–2685.
- (141) Kappl, M.; Butt, H.-J. The Colloidal Probe Technique and Its Application to Adhesion Force Measurements. *Particle & Particle Systems Characterization* **2002**, 19 (3), 129–143.
- (142) O'Shea, S. J.; Welland, M. E.; Rayment, T. An Atomic Force Microscope Study of Grafted Polymers on Mica. *Langmuir* **1993**, 9 (7), 1826–1835.
- (143) Elmahdy, M. M.; Drechsler, A.; Bittrich, E.; Uhlmann, P.; Stamm, M. Interactions Between Silica Particles and Poly(2-Vinylpyridine) Brushes in Aqueous Solutions of Monovalent and Multivalent Salts. *Colloid Polym Sci* **2014**, 292 (8), 1999–2012.

- (144) Neubauer, M. P.; Blüm, C.; Agostini, E.; Engert, J.; Scheibel, T.; Fery, A. Micromechanical Characterization of Spider Silk Particles. *Biomater. Sci.* **2013**, *1* (11), 1160–1166.
- (145) Schmidt, S.; Zeiser, M.; Hellweg, T.; Duschl, C.; Fery, A.; Möhwald, H. Adhesion and Mechanical Properties of PNIPAM Microgel Films and Their Potential Use as Switchable Cell Culture Substrates. *Adv. Funct. Mater.* **2010**, *20* (19), 3235–3243.
- (146) Pan, H. M.; Seuss, M.; Neubauer, M. P.; Trau, D. W.; Fery, A. Tuning the Mechanical Properties of Hydrogel Core-Shell Particles by Inwards Interweaving Self-Assembly. *ACS Appl. Mater. Interfaces* **2016**, *8* (2), 1493–1500.
- (147) Lai, W. M.; Rubin, D. H.; Rubin, D.; Krempel, E. *Introduction to Continuum Mechanics*; Butterworth-Heinemann, 2009.
- (148) Hertz, H. Ueber Die Berührung Fester Elastischer Körper. *J. Reine Angew. Math.* **1881**, No. 92, 156–171.
- (149) Johnson, K. L.; Kendall, K.; Roberts, A. D. Surface Energy and the Contact of Elastic Solids. *Proc. R. Soc. Lond. A* **1971**, *324* (1558), 301–313.
- (150) Derjaguin, B. V.; Muller, V. M.; Toporov, Y. P. Effect of Contact Deformations on the Adhesion of Particles. *Journal of Colloid and Interface Science* **1975**, *53* (2), 314–326.
- (151) Erath, J.; Schmidt, S.; Fery, A. Characterization of Adhesion Phenomena and Contact of Surfaces by Soft Colloidal Probe AFM. *Soft Matter* **2010**, *6* (7), 1432–1437.
- (152) Attard, P.; Parker, J. Deformation and Adhesion of Elastic Bodies in Contact. *Phys. Rev. A* **1992**, *46* (12), 7959–7971.
- (153) Maugis, D. Adhesion of Spheres: the JKR-DMT Transition Using a Dugdale Model. *Journal of Colloid and Interface Science* **1992**, *150* (1), 243–269.
- (154) Glaubitz, M.; Medvedev, N.; Pussak, D.; Hartmann, L.; Schmidt, S.; Helm, C. A.; Delcea, M. A Novel Contact Model for AFM Indentation Experiments on Soft Spherical Cell-Like Particles. *Soft Matter* **2014**, *10*, 6732–6741.
- (155) Korayem, M. H.; Taheri, M. Modeling of Various Contact Theories for the Manipulation of Different Biological Micro/Nanoparticles Based on AFM. *J Nanopart Res* **2013**, *16* (1), 408–418.
- (156) Lakowicz, J. R. Introduction to Fluorescence. In *Principles of Fluorescence Spectroscopy*; Plenum Press, 1999; pp 1–23.
- (157) Franck, J.; Dymond, E. G. Elementary Processes of Photochemical Reactions. *Transactions of the Faraday Society* **1926**, *21*, 536–542.
- (158) Condon, E. U. A Theory of Intensity Distribution in Band Systems. *Physical Review* **1926**, *28* (6), 1182–1201.
- (159) Condon, E. U. Nuclear Motions Associated with Electron Transitions in Diatomic Molecules. *Physical Review* **1928**, *32* (6), 858–872.
- (160) Clegg, R. M. Förster Resonance Energy Transfer—FRET What Is It, Why Do It, and How It's Done. In *FRET and FLIM Techniques*; Gadella, T. W. J., Ed.; Elsevier, 2009; Vol. 33, pp 1–57.
- (161) Stern, O.; Volmer, M. Über Die Abklingungszeit Der Fluoreszenz. *Physikalische Zeitschrift* **1919**, *20*, 183–188.
- (162) Lakowicz, J. R.; Weber, G. Quenching of Fluorescence by Oxygen. Probe for Structural Fluctuations in Macromolecules. *Biochemistry* **1973**, *12* (21), 4161–4170.
- (163) Webber, S. E. The Role of Time-Dependent Measurements in Elucidating Static Versus Dynamic Quenching Processes. *Photochem Photobiol* **1997**, *65* (1), 33–38.
- (164) Geddes, C. D. Optical Halide Sensing Using Fluorescence Quenching: Theory, Simulations and Applications - a Review. *Measurement Science and Technology* **2001**, *12* (9), R53.
- (165) Lin, Y.-H.; Tseng, W.-L. Ultrasensitive Sensing of Hg<sup>2+</sup> and CH<sub>3</sub>Hg<sup>+</sup> Based on the Fluorescence Quenching of Lysozyme Type VI-Stabilized Gold Nanoclusters. *Anal. Chem.* **2010**, *82* (22), 9194–9200.
- (166) Satishkumar, B. C.; Brown, L. O.; Gao, Y.; Wang, C.-C.; Wang, H.-L.; Doorn, S. K. Reversible Fluorescence Quenching in Carbon Nanotubes for Biomolecular Sensing. *Nature Nanotech* **2007**, *2* (9), 560–564.
- (167) Blakely, B. L.; Dumelin, C. E.; Trappmann, B.; McGregor, L. M.; Choi, C. K.; Anthony, P. C.; Duesterberg, V. K.; Baker, B. M.; Block, S. M.; Liu, D. R.; et al. A DNA-Based Molecular Probe for Optically Reporting Cellular Traction Forces. *Nat Methods* **2014**, *11* (12), 1229–1232.
- (168) Kim, T. W.; Park, J.-H.; Hong, J.-I. Self-Quenching Mechanism: the Influence of Quencher and Spacer on Quencher-Fluorescein Probes. *Bulletin of the Korean Chemical Society* **2007**, *28* (7), 1221–1223.

- (169) Chen, R. F.; Knutson, J. R. Mechanism of Fluorescence Concentration Quenching of Carboxyfluorescein in Liposomes - Energy-Transfer to Nonfluorescent Dimers. *Analytical Biochemistry* **1988**, *172* (1), 61–77.
- (170) Förster, T. Energiewanderung Und Fluoreszenz. *Naturwissenschaften* **1946**, *33* (6), 166–175.
- (171) Förster, T. Zwischenmolekulare Energiewanderung Und Fluoreszenz. *Annalen der Physik* **1948**, *437* (1-2), 55–75.
- (172) Perrin, J. Fluorescence Et Induction Moléculaire Par Resonance. *C. R. Hebd. Seances Acad. Sci.* **1927**, *184*, 1097–1100.
- (173) Perrin, F. Interaction Entre Atomes Normal Et Activité. Transferts D'activation. Formation D'une Molécule Activée. **1933**, *3* (3), 279–318.
- (174) Clegg, R. M. Fluorescence Resonance Energy Transfer. *Current Opinion in Biotechnology* **1995**, *6* (1), 103–110.
- (175) Stryer, L. Fluorescence Energy Transfer as a Spectroscopic Ruler. *Annual Review of Biochemistry* **1978**, *47* (1), 819–846.
- (176) Albertazzi, L.; Martinez-Veracoechea, F. J.; Leenders, C. M. A.; Voets, I. K.; Frenkel, D.; Meijer, E. W. Spatiotemporal Control and Superselectivity in Supramolecular Polymers Using Multivalency. *PNAS* **2013**, *110* (30), 12203–12208.
- (177) Kong, H. J.; Boonthekul, T.; Mooney, D. J. Quantifying the Relation Between Adhesion Ligand-Receptor Bond Formation and Cell Phenotype. *PNAS* **2006**, *103* (49), 18534–18539.
- (178) Grunwell, J. R.; Glass, J. L.; Lacoste, T. D.; Deniz, A. A.; Chemla, D. S.; Schultz, P. G. Monitoring the Conformational Fluctuations of DNA Hairpins Using Single-Pair Fluorescence Resonance Energy Transfer. *J. Am. Chem. Soc.* **2001**, *123* (18), 4295–4303.
- (179) Tsukanov, R.; Tomov, T. E.; Berger, Y.; Liber, M.; Nir, E. Conformational Dynamics of DNA Hairpins at Millisecond Resolution Obtained From Analysis of Single-Molecule FRET Histograms. *J Phys Chem B* **2013**, *117* (50), 16105–16109.
- (180) van de Laar, T.; Schuurman, H.; van der Scheer, P.; Maarten van Doorn, J.; van der Gucht, J.; Sprakel, J. Light From Within: Sensing Weak Strains and FemtoNewton Forces in Single Molecules. *Chem* **2018**, *4* (2), 269–284.
- (181) Feige, J. N.; Sage, D.; Wahli, W.; Desvergne, B.; Gelman, L. PixFRET, an ImageJ Plug-in for FRET Calculation That Can Accommodate Variations in Spectral Bleed-Throughs. *Microsc. Res. Tech.* **2005**, *68* (1), 51–58.
- (182) Jares-Erijman, E. A.; Jovin, T. M. FRET Imaging. *Nat Biotechnol* **2003**, *21* (11), 1387–1395.
- (183) *Handbook of Biological Confocal Microscopy*, 3rd Edition, 3rd ed.; Pawley, J. B., Ed.; Springer Science: New York, NY, USA, 2006.
- (184) Minsky, M. Microscopy Apparatus.
- (185) Streibl, N. Three-Dimensional Imaging by a Microscope. *J. Opt. Soc. Am. A, JOSAA* **1985**, *2* (2), 121–127.
- (186) Minsky, M. Memoir on Inventing the Confocal Scanning Microscope. *Scanning* **1988**, *10* (4), 128–138.
- (187) Radmacher, M.; Eberle, K.; Gaub, H. E. An Afm with Integrated Micro-Fluorescence Optics - Design and Performance. *Ultramicroscopy* **1992**, *42*, 968–972.
- (188) Åslund, N.; Liljeborg, A.; Forsgren, P. O.; Wahlsten, S. Three-Dimensional Digital Microscopy Using the PHOIBOSI Scanner. *Scanning* **1987**, *9* (6), 227–235.
- (189) Carl Zeiss Microscopy GmbH. Brochure LSM710 Confocal Microscope, 2009, 1–32.
- (190) Petráň, M.; Hadravský, M.; Egger, M. D.; Galambos, R. Tandem-Scanning Reflected-Light Microscope. *J. Opt. Soc. Am.* **1968**, *58* (5), 661.
- (191) Linfoot, E. H.; Wolf, E. Diffraction Images in Systems with an Annular Aperture. *Proceedings of the Physical Society. Section B* **1953**, *66* (2), 145–149.
- (192) Wilson, T.; Carlini, A. R. Size of the Detector in Confocal Imaging Systems. *Opt. Lett.* **1987**, *12* (4), 227–229.
- (193) Dickinson, M. E.; Bearman, G.; Tille, S.; Lansford, R.; Fraser, S. E. Multi-Spectral Imaging and Linear Unmixing Add a Whole New Dimension to Laser Scanning Fluorescence Microscopy. *BioTechniques* **2001**, *31* (6), 1272–1278.
- (194) *FRET and FLIM Techniques*; Gadella, T. W. J., Ed.; Elsevier, 2009.
- (195) Peter, M.; Ameer-Beg, S. M. Imaging Molecular Interactions by Multiphoton FLIM. *Biology of the Cell* **2004**, *96* (3), 231–236.
- (196) Paredes, J. M.; Giron, M. D.; Ruedas-Rama, M. J.; Orte, A.; Crovetto, L.; Talavera, E. M.; Salto, R.; Alvarez-Pez, J. M. Real-Time Phosphate Sensing in Living Cells Using Fluorescence Lifetime Imaging Microscopy (FLIM). *J Phys Chem B* **2013**, *117* (27), 8143–8149.



- (197) Gerritsen, H. C.; Sanders, R.; Draaijer, A.; Ince, C.; Levine, Y. K. Fluorescence Lifetime Imaging of Oxygen in Living Cells. *Journal of Fluorescence* **1997**, *7* (1), 11–15.
- (198) Klar, T. A.; Jakobs, S.; Dyba, M.; Egner, A.; Hell, S. W. Fluorescence Microscopy with Diffraction Resolution Barrier Broken by Stimulated Emission. *PNAS* **2000**, *97* (15), 8206–8210.
- (199) Betzig, E.; Patterson, G. H.; Sougrat, R.; Lindwasser, O. W.; Olenych, S.; Bonifacino, J. S.; Davidson, M. W.; Lippincott-Schwartz, J.; Hess, H. F. Imaging Intracellular Fluorescent Proteins at Nanometer Resolution. *Science* **2006**, *313* (5793), 1642–1645.
- (200) Wilson, T. Scanning Optical Microscopy. *Scanning* **1985**, *7* (2), 79–87.
- (201) Webb, R. H. Confocal Microscopes. *Optics & Photonics News* **1991**, *2* (7), 8–13.
- (202) Pawley, J. B. Fundamental and Practical Limits in Confocal Light Microscopy. *Scanning* **1991**, *13* (2), 184–198.
- (203) Caruso, M. M.; Davis, D. A.; Shen, Q.; Odom, S. A.; Sottos, N. R.; White, S. R.; Moore, J. S. Mechanically-Induced Chemical Changes in Polymeric Materials. *Chem. Rev.* **2009**, *109* (11), 5755–5798.
- (204) Goktas, M.; Blank, K. G. Molecular Force Sensors: From Fundamental Concepts Toward Applications in Cell Biology. *Adv. Mater. Interfaces* **2017**, *4* (1), 1600441.
- (205) Freikamp, A.; Cost, A.-L.; Grashoff, C. The Piconewton Force Awakens: Quantifying Mechanics in Cells. *Trends Cell Biol.* **2016**, *26* (11), 838–847.
- (206) Ashkin, A.; Dziedzic, J. M.; Bjorkholm, J. E.; Chu, S. Observation of a Single-Beam Gradient Force Optical Trap for Dielectric Particles. *Opt. Lett.* **1986**, *11* (5), 288–290.
- (207) Polimeno, P.; Magazzù, A.; Iati, M. A.; Patti, F.; Saija, R.; Boschi, C. D. E.; Donato, M. G.; Pietro G Gucciardi; Jones, P. H.; Volpe, G.; et al. Journal of Quantitative Spectroscopy & Radiative Transfer. *Journal of Quantitative Spectroscopy and Radiative Transfer* **2018**, *218*, 131–150.
- (208) Stabley, D. R.; Jurchenko, C.; Marshall, S. S.; Salaita, K. S. Visualizing Mechanical Tension Across Membrane Receptors with a Fluorescent Sensor. *Nat Methods* **2011**, *9* (1), 64–67.
- (209) Liu, Y.; Yehl, K.; Narui, Y.; Salaita, K. Tension Sensing Nanoparticles for Mechano-Imaging at the Living/Nonliving Interface. *J. Am. Chem. Soc.* **2013**, *135* (14), 5320–5323.
- (210) Jurchenko, C.; Chang, Y.; Narui, Y.; Zhang, Y.; Salaita, K. S. Integrin-Generated Forces Lead to Streptavidin-Biotin Unbinding in Cellular Adhesions. *Biophys. J.* **2014**, *106* (7), 1436–1446.
- (211) Chang, Y.; Liu, Z.; Zhang, Y.; Galior, K.; Yang, J.; Salaita, K. A General Approach for Generating Fluorescent Probes to Visualize Piconewton Forces at the Cell Surface. *J. Am. Chem. Soc.* **2016**, *138* (9), 2901–2904.
- (212) Tarsa, P. B.; Brau, R. R.; Barch, M.; Ferrer, J. M.; Freyzon, Y.; Matsudaira, P.; Lang, M. J. Detecting Force-Induced Molecular Transitions with Fluorescence Resonant Energy Transfer. *Angewandte Chemie* **2007**, *119* (12), 2045–2047.
- (213) Wang, X.; Rahil, Z.; Li, I. T. S.; Chowdhury, F.; Leckband, D. E.; Chemla, Y. R.; Ha, T. Constructing Modular and Universal Single Molecule Tension Sensor Using Protein G to Study Mechano- Sensitive Receptors. *Sci Rep* **2016**, 1–10.
- (214) Nickels, P. C.; Wunsch, B.; Holzmeister, P.; Bae, W.; Kneer, L. M.; Grohmann, D.; Tinnefeld, P.; Liedl, T. Molecular Force Spectroscopy with a DNA Origami–Based Nanoscopic Force Clamp. *Science* **2016**, *354* (6310), 305–307.
- (215) Kim, T.-J.; Zheng, S.; Sun, J.; Muhamed, I.; Wu, J.; Lei, L.; Kong, X.; Leckband, D. E.; Wang, Y. Dynamic Visualization of A-Catenin Reveals Rapid, Reversible Conformation Switching Between Tension States. *Current Biology* **2015**, *25* (2), 218–224.
- (216) Kisley, L.; Serrano, K. A.; Guin, D.; Kong, X.; Gruebele, M.; Leckband, D. E. Direct Imaging of Protein Stability and Folding Kinetics in Hydrogels. *ACS Appl. Mater. Interfaces* **2017**, *9* (26), 21606–21617.
- (217) Carpick, R. W.; Sasaki, D. Y.; Burns, A. R. First Observation of Mechanochromism at the Nanometer Scale. *Langmuir* **2000**, *16* (3), 1270–1278.
- (218) Chance, R. R. Chromism in Polydiacetylene Solutions and Crystals. *Macromolecules* **1980**, *13* (2), 396–398.
- (219) Suhina, T.; Weber, B.; Carpentier, C. E.; Lorincz, K.; Schall, P.; Bonn, D.; Brouwer, A. M. Fluorescence Microscopy Visualization of Contacts Between Objects. *Angew. Chem. Int. Ed.* **2015**, *54* (12), 3688–3691.
- (220) Davis, D. A.; Hamilton, A.; Yang, J.; Cremer, L. D.; Van Gough, D.; Potisek, S. L.; Ong, M. T.; Braun, P. V.; Martínez, T. J.; White, S. R.; et al. Force-Induced Activation of Covalent Bonds in Mechanoresponsive Polymeric Materials. *Nature* **2009**, *459* (7243), 68–72.

- (221) Beiermann, B. A.; Davis, D. A.; Kramer, S. L. B.; Moore, J. S.; Sottos, N. R.; White, S. R. Environmental Effects on Mechanochemical Activation of Spiropyran in Linear PMMA. *J. Mater. Chem.* **2011**, *21* (23), 8443–8445.
- (222) Kingsbury, C. M.; May, P. A.; Davis, D. A.; White, S. R.; Moore, J. S.; Sottos, N. R. Shear Activation of Mechanophore-Crosslinked Polymers. *J. Mater. Chem.* **2011**, *21* (23), 8381.
- (223) Gossweiler, G. R.; Kouznetsova, T. B.; Craig, S. L. Force-Rate Characterization of Two Spiropyran-Based Molecular Force Probes. *J. Am. Chem. Soc.* **2015**, *137* (19), 6148–6151.
- (224) Chen, Y.; Spiering, A. J. H.; Karthikeyan, S.; Peters, G. W. M.; Meijer, E. W.; Sijbesma, R. P. Mechanically Induced Chemiluminescence From Polymers Incorporating a 1,2-Dioxetane Unit in the Main Chain. *Nat. Chem.* **2012**, *4* (7), 559–562.
- (225) Cho, S.-Y.; Kim, J.-G.; Chung, C.-M. A Fluorescent Crack Sensor Based on Cyclobutane-Containing Crosslinked Polymers of Tricinnamates. *Sensors and Actuators B: Chemical* **2008**, *134* (2), 822–825.
- (226) Göstl, R.; Sijbesma, R. P.  $\Pi$ -Extended Anthracenes as Sensitive Probes for Mechanical Stress. *Chem. Sci.* **2015**, *7*, 370–375.
- (227) Cingil, H. E.; Storm, I. M.; Yorulmaz, Y.; Brake, D. W.; de Vries, R.; Cohen Stuart, M. A.; Sprakel, J. Monitoring Protein Capsid Assembly with a Conjugated Polymer Strain Sensor. *J. Am. Chem. Soc.* **2015**, *137* (31), 9800–9803.
- (228) Fernandes, P. A. L.; Delcea, M.; Skirtach, A. G.; Möhwald, H.; Fery, A. Quantification of Release From Microcapsules Upon Mechanical Deformation with AFM. *Soft Matter* **2010**, *6* (9), 1879–1883.
- (229) Mertz, D.; Vogt, C.; Hemmerlé, J.; Mutterer, J.; Ball, V.; Voegel, J.-C.; Schaaf, P.; Lavalle, P. Mechanotransductive Surfaces for Reversible Biocatalysis Activation. *Nat. Mater.* **2009**, *8* (9), 731–735.
- (230) Fitch, K. R.; Goodwin, A. P. Mechanochemical Reaction Cascade for Sensitive Detection of Covalent Bond Breakage in Hydrogels. *Chem. Mater.* **2014**, *26* (23), 6771–6776.
- (231) Akamatsu, N.; Hisano, K.; Tatsumi, R.; Aizawa, M.; Barrett, C. J.; Shishido, A. Thermo-, Photo-, and Mechano-Responsive Liquid Crystal Networks Enable Tunable Photonic Crystals. *Soft Matter* **2017**, *13* (41), 7486–7491.
- (232) Ishijima, Y.; Imai, H.; Oaki, Y. Tunable Mechano-Responsive Color-Change Properties of Organic Layered Material by Intercalation. *Chem* **2017**, *3* (3), 509–521.
- (233) Kim, P.; Hu, Y.; Alvarenga, J.; Kolle, M.; Suo, Z.; Aizenberg, J. Rational Design of Mechano-Responsive Optical Materials by Fine Tuning the Evolution of Strain-Dependent Wrinkling Patterns. *Advanced Optical Materials* **2013**, *1* (5), 381–388.
- (234) Fu, F.; Shang, L.; Chen, Z.; Yu, Y.; Zhao, Y. Bioinspired Living Structural Color Hydrogels. *Science Robotics* **2018**, *3* (16), eaar8580.
- (235) Wang, X.-Q.; Hong, R.; Wang, C.-F.; Tan, P.-F.; Ji, W.-Q.; Chen, S. Ultrafast Mechano-Responsive Photonic Hydrogel Towards Multicolor Displays via the Pressure Sensation. *Materials Letters* **2017**, *189*, 321–324.
- (236) Zhang, J.; He, S.; Liu, L.; Guan, G.; Lu, X.; Sun, X.; Peng, H. The Continuous Fabrication of Mechanochromic Fibers. *J. Mater. Chem. C* **2016**, *4* (11), 2127–2133.
- (237) Steiner, A. M.; Mayer, M.; Seuss, M.; Nikolov, S.; Harris, K. D.; Alexeev, A.; Kuttner, C.; König, T. A. F.; Fery, A. Macroscopic Strain-Induced Transition From Quasi-Infinite Gold Nanoparticle Chains to Defined Plasmonic Oligomers. *ACS Nano* **2017**, *11* (9), 8871–8880.
- (238) Weng, G.; Thanneeru, S.; He, J. Dynamic Coordination of Eu-Iminodiacetate to Control Fluorochromic Response of Polymer Hydrogels to Multistimuli. *Adv. Mater.* **2018**, *30* (11), 1706526–1706527.
- (239) Caruso, F.; Donath, E.; Möhwald, H.; Georgieva, R. Fluorescence Studies of the Binding of Anionic Derivatives of Pyrene and Fluorescein to Cationic Polyelectrolytes in Aqueous Solution. *Macromolecules* **1998**, *31* (21), 7365–7377.
- (240) Merindol, R.; Delechiave, G.; Heinen, L.; Catalani, L. H.; Walther, A. Modular Design of Programmable Mechano-fluorescent DNA Hydrogels. *Nat. Commun.* **2019**, 1–10.
- (241) Arzt, E.; Gorb, S.; Spolenak, R. From Micro to Nano Contacts in Biological Attachment Devices. *PNAS* **2003**, *100* (19), 10603–10606.
- (242) Gorb, E. V.; Gorb, S. N. Attachment Ability of the Beetle *Chrysolina fastuosa* on Various Plant Surfaces. *Entomologia Experimentalis et Applicata* **2002**, *105* (1), 13–28.
- (243) del Campo, A.; Greiner, C.; Álvarez, I.; Arzt, E. Patterned Surfaces with Pillars with Controlled 3D Tip Geometry Mimicking Bioattachment Devices. *Adv. Mater.* **2007**, *19* (15), 1973–1977.
- (244) Murphy, M. P.; Kim, S.; Sitti, M. Enhanced Adhesion by Gecko-Inspired Hierarchical Fibrillar Adhesives. *ACS Appl. Mater. Interfaces* **2009**, *1* (4), 849–855.

- (245) Hu, H.; Tian, H.; Li, X.; Shao, J.; Ding, Y.; Liu, H.; An, N. Biomimetic Mushroom-Shaped Microfibers for Dry Adhesives by Electrically Induced Polymer Deformation. *ACS Appl. Mater. Interfaces* **2014**, *6* (16), 14167–14173.
- (246) Afferrante, L.; Carbone, G. Biomimetic Surfaces with Controlled Direction-Dependent Adhesion. *J. R. Soc. Interface* **2012**, *9* (77), 3359–3365.
- (247) Wang, Z.; Gu, P.; Wu, X. A Gecko-Inspired Double-Sided Adhesive. *Phys. Chem. Chem. Phys.* **2013**, *15* (47), 20764–20770.
- (248) Yi, H.; Hwang, I.; Sung, M.; Lee, D.; Kim, J.-H.; Kang, S. M.; Bae, W.-G.; Jeong, H. E. Bio-Inspired Adhesive Systems for Next-Generation Green Manufacturing. *Int. J. Precis. Eng. Man.-Green Technol.* **2014**, *1* (4), 347–351.
- (249) Gorb, S.; Varenberg, M.; Peressadko, A.; Tuma, J. Biomimetic Mushroom-Shaped Fibrillar Adhesive Microstructure. *J. R. Soc. Interface* **2007**, *4* (13), 271–275.
- (250) Xue, L.; Kovalev, A.; Eichler-Volf, A.; Steinhart, M.; Gorb, S. N. Humidity-Enhanced Wet Adhesion on Insect-Inspired Fibrillar Adhesive Pads. *Nat. Commun.* **2015**, *6*, 6621.
- (251) Glassmaker, N. J.; Jagota, A.; Hui, C.-Y.; Noderer, W. L.; Chaudhury, M. K. Biologically Inspired Crack Trapping for Enhanced Adhesion. *Proc. Natl. Acad. Sci. U.S.A.* **2007**, *104* (26), 10786–10791.
- (252) Paretkar, D.; Kamperman, M.; Martina, D.; Zhao, J.; Creton, C.; Lindner, A.; Jagota, A.; McMeeking, R.; Arzt, E. Preload-Responsive Adhesion: Effects of Aspect Ratio, Tip Shape and Alignment. *J. R. Soc. Interface* **2013**, *10* (83), 20130171.
- (253) Bartlett, M. D.; Croll, A. B.; King, D. R.; Paret, B. M.; Irschick, D. J.; Crosby, A. J. Looking Beyond Fibrillar Features to Scale Gecko-Like Adhesion. *Adv. Mater.* **2012**, *24* (8), 1078–1083.
- (254) Spolenak, R.; Gorb, S.; Arzt, E. Adhesion Design Maps for Bio-Inspired Attachment Systems. *Acta Biomater.* **2005**, *1* (1), 5–13.
- (255) Boesel, L. F.; Greiner, C.; Arzt, E.; del Campo, A. Gecko-Inspired Surfaces: a Path to Strong and Reversible Dry Adhesives. *Adv. Mater.* **2010**, *22* (19), 2125–2137.
- (256) Ohler, A. Digital Pad Morphology in Torrent-Living Ranid Frogs. *Asiatic Herpetological Research* **1995**, *6*, 85–96.
- (257) Federle, W.; Barnes, W. J. P.; Baumgartner, W.; Drechsler, P.; Smith, J. M. Wet but Not Slippery: Boundary Friction in Tree Frog Adhesive Toe Pads. *J. R. Soc. Interface* **2006**, *3* (10), 689–697.
- (258) Drotlef, D.-M.; Stepien, L.; Kappl, M.; Barnes, W. J. P.; Butt, H.-J.; del Campo, A. Insights Into the Adhesive Mechanisms of Tree Frogs Using Artificial Mimics. *Adv. Funct. Mater.* **2013**, *23* (9), 1137–1146.
- (259) Iturri, J.; Xue, L.; Kappl, M.; García Fernández, L.; Barnes, W. J. P.; Butt, H.-J.; del Campo, A. Torrent Frog-Inspired Adhesives: Attachment to Flooded Surfaces. *Adv. Funct. Mater.* **2015**, *25* (10), 1499–1505.
- (260) Autumn, K.; Sitti, M.; Liang, Y. A.; Peattie, A. M.; Hansen, W. R.; Sponberg, S.; Kenny, T. W.; Fearing, R.; Israelachvili, J. N.; Full, R. J. Evidence for Van Der Waals Adhesion in Gecko Setae. *PNAS* **2002**, *99* (19), 12252–12256.
- (261) Huber, G.; Gorb, S. N.; Spolenak, R.; Arzt, E. Resolving the Nanoscale Adhesion of Individual Gecko Spatulae by Atomic Force Microscopy. *Biol. Lett.* **2005**, *1* (1), 2–4.
- (262) Varenberg, M.; Gorb, S. A Beetle-Inspired Solution for Underwater Adhesion. *J. R. Soc. Interface* **2008**, *5* (20), 383–385.
- (263) Greiner, C.; del Campo, A.; Arzt, E. Adhesion of Bioinspired Micropatterned Surfaces: Effects of Pillar Radius, Aspect Ratio, and Preload. *Langmuir* **2007**, *23* (7), 3495–3502.
- (264) Xue, L.; Iturri, J.; Kappl, M.; Butt, H.-J.; del Campo, A. Bioinspired Orientation-Dependent Friction. *Langmuir* **2014**, *30* (37), 11175–11182.
- (265) Heepe, L.; Gorb, S. N. Biologically Inspired Mushroom-Shaped Adhesive Microstructures. *Annu. Rev. Mater. Res.* **2014**, *44* (1), 173–203.
- (266) Aksak, B.; Murphy, M. P.; Sitti, M. Adhesion of Biologically Inspired Vertical and Angled Polymer Microfiber Arrays. *Langmuir* **2007**, *23* (6), 3322–3332.
- (267) Purtov, J.; Frensemeier, M.; Kroner, E. Switchable Adhesion in Vacuum Using Bio-Inspired Dry Adhesives. *ACS Appl. Mater. Interfaces* **2015**, *7* (43), 24127–24135.
- (268) Murphy, M. P.; Aksak, B.; Sitti, M. Gecko-Inspired Directional and Controllable Adhesion. *Small* **2009**, *5* (2), 170–175.
- (269) del Campo, A.; Greiner, C.; Arzt, E. Contact Shape Controls Adhesion of Bioinspired Fibrillar Surfaces. *Langmuir* **2007**, *23* (20), 10235–10243.
- (270) Hossfeld, C. K.; Schneider, A. S.; Arzt, E.; Frick, C. P. Detachment Behavior of Mushroom-Shaped Fibrillar Adhesive Surfaces in Peel Testing. *Langmuir* **2013**, *29* (49), 15394–15404.

- (271) Varenberg, M.; Gorb, S. Close-Up of Mushroom-Shaped Fibrillar Adhesive Microstructure: Contact Element Behaviour. *J. R. Soc. Interface* **2008**, *5* (24), 785–789.
- (272) Heepe, L.; Kovalev, A. E.; Filippov, A. E.; Gorb, S. N. Adhesion Failure at 180 000 Frames Per Second: Direct Observation of the Detachment Process of a Mushroom-Shaped Adhesive. *Phys. Rev. Lett.* **2013**, *111* (10), 104301.
- (273) Heepe, L.; Kovalev, A. E.; Gorb, S. N. Direct Observation of Microcavitation in Underwater Adhesion of Mushroom-Shaped Adhesive Microstructure. *Beilstein J. Nanotechnol.* **2014**, *5*, 903–909.
- (274) Paretkar, D.; Schneider, A. S.; Kroner, E.; Arzt, E. In Situ Observation of Contact Mechanisms in Bioinspired Adhesives at High Magnification. *MRC* **2011**, *1* (01), 53–56.
- (275) Creton, C.; Lakrout, H. Micromechanics of Flat-Probe Adhesion Tests of Soft Viscoelastic Polymer Films. *J. Polym. Sci. B Polym. Phys.* **2000**, *38* (7), 965–979.
- (276) Carbone, G.; Pierro, E.; Gorb, S. N. Origin of the Superior Adhesive Performance of Mushroom-Shaped Microstructured Surfaces. *Soft Matter* **2011**, *7* (12), 5545–5552.
- (277) Carbone, G.; Pierro, E. Sticky Bio-Inspired Micropillars: Finding the Best Shape. *Small* **2012**, *8* (9), 1449–1454.
- (278) Aksak, B.; Hui, C.-Y.; Sitti, M. The Effect of Aspect Ratio on Adhesion and Stiffness for Soft Elastic Fibres. *J. R. Soc. Interface* **2011**, *8* (61), 1166–1175.
- (279) Aksak, B.; Sahin, K.; Sitti, M. The Optimal Shape of Elastomer Mushroom-Like Fibers for High and Robust Adhesion. *Beilstein J. Nanotechnol.* **2014**, *5*, 630–638.
- (280) Spuskanyuk, A. V.; McMeeking, R. M.; Deshpande, V. S.; Arzt, E. The Effect of Shape on the Adhesion of Fibrillar Surfaces. *Acta Biomater.* **2008**, *4* (6), 1669–1676.
- (281) Khaderi, S. N.; Fleck, N. A.; Arzt, E.; McMeeking, R. M. Detachment of an Adhered Micropillar From a Dissimilar Substrate. *J. Mech. Phys. Solids* **2015**, *75* (C), 159–183.
- (282) Balijepalli, R. G.; Begley, M. R.; Fleck, N. A.; McMeeking, R. M.; Arzt, E. Numerical Simulation of the Edge Stress Singularity and the Adhesion Strength for Compliant Mushroom Fibrils Adhered to Rigid Substrates. *Int. J. Solids Struct.* **2016**, *85–86* (C), 160–171.
- (283) Neubauer, J. W. Structural Properties and Interactions of Mechano-Responsive Polyelectrolyte Brushes, Master Thesis: University of Bayreuth, Bayreuth, Germany, 2014.
- (284) Carbone, G.; Pierro, E. Effect of Interfacial Air Entrapment on the Adhesion of Bio-Inspired Mushroom-Shaped Micro-Pillars. *Soft Matter* **2012**, *8* (30), 7904–7906.
- (285) Papadopoulos, P.; Deng, X.; Mammen, L.; Drotlef, D.-M.; Battagliarin, G.; Li, C.; Müllen, K.; Landfester, K.; del Campo, A.; Butt, H.-J.; et al. Wetting on the Microscale: Shape of a Liquid Drop on a Microstructured Surface at Different Length Scales. *Langmuir* **2012**, *28* (22), 8392–8398.
- (286) Hensel, R.; Helbig, R.; Aland, S.; Braun, H.-G.; Voigt, A.; Neinhuis, C.; Werner, C. Wetting Resistance at Its Topographical Limit: the Benefit of Mushroom and Serif T Structures. *Langmuir* **2013**, *29* (4), 1100–1112.
- (287) Lee, H.; Lee, B. P.; Messersmith, P. B. A Reversible Wet/Dry Adhesive Inspired by Mussels and Geckos. *Nature* **2007**, *448* (7151), 338–341.
- (288) Heepe, L.; Varenberg, M.; Itovich, Y.; Gorb, S. N. Suction Component in Adhesion of Mushroom-Shaped Microstructure. *J. R. Soc. Interface* **2011**, *8* (57), 585–589.
- (289) La Spina, R.; Tomlinson, M. R.; Ruiz-Pérez, L.; Chiche, A.; Langridge, S.; Geoghegan, M. Controlling Network–Brush Interactions to Achieve Switchable Adhesion. *Angew. Chem. Int. Ed.* **2007**, *46* (34), 6460–6463.
- (290) Sudre, G.; Olanier, L.; Tran, Y.; Hourdet, D.; Creton, C. Reversible Adhesion Between a Hydrogel and a Polymer Brush. *Soft Matter* **2012**, *8* (31), 8184–8193.
- (291) Yuk, H.; Zhang, T.; Lin, S.; Parada, G. A.; Zhao, X. Tough Bonding of Hydrogels to Diverse Non-Porous Surfaces. *Nat. Mater.* **2015**, *15* (2), 190–196.
- (292) Phelps, E. A.; Enemchukwu, N. O.; Fiore, V. F.; Sy, J. C.; Murthy, N.; Sulchek, T. A.; Barker, T. H.; García, A. J. Maleimide Cross-Linked Bioactive PEG Hydrogel Exhibits Improved Reaction Kinetics and Cross-Linking for Cell Encapsulation and in Situ Delivery. *Adv. Mater.* **2012**, *24* (1), 64–70.
- (293) Nair, D. P.; Podgórski, M.; Chatani, S.; Gong, T.; Xi, W.; Fenoli, C. R.; Bowman, C. N. The Thiol-Michael Addition Click Reaction: a Powerful and Widely Used Tool in Materials Chemistry. *Chem. Mater.* **2014**, *26* (1), 724–744.
- (294) Girardo, S.; Träber, N.; Wagner, K.; Cojoc, G.; Herold, C.; Goswami, R.; Schlübler, R.; Abuhattum, S.; Taubenberger, A.; Reichel, F.; et al. Standardized Microgel Beads as Elastic Cell Mechanical Probes. *J. Mater. Chem. B* **2018**, *6* (39), 6245–6261.

- (295) Johnston, K. P.; Harrison, K. L.; Clarke, M. J.; Howdle, S. M.; Heitz, M. P.; Bright, F. V.; Carlier, C.; Randolph, T. W. Water-in-Carbon Dioxide Microemulsions: an Environment for Hydrophiles Including Proteins. *Science* **1996**, *271* (5249), 624–626.
- (296) Shi, X. D.; Brenner, M. P.; Nagel, S. R. A Cascade of Structure in a Drop Falling From a Faucet. *Science* **1994**, *265* (5169), 219–222.
- (297) Atcher, J.; Alfonso, I. The Effect of DMSO in the Aqueous Thiol–Disulphide Dynamic Covalent Chemistry of Model Pseudo-peptides. *RSC Adv.* **2013**, *3* (48), 25605–25608.
- (298) Kang, M. K.; Huang, R. A Variational Approach and Finite Element Implementation for Swelling of Polymeric Hydrogels Under Geometric Constraints. *J. Appl. Mech.* **2010**, *77* (6), 061004.
- (299) *CRC Handbook of Chemistry and Physics*; Lide, D. R., Ed.; CRC Press: Boca Raton, FL, 2005.
- (300) Thermo Fisher Scientific. Manufacturer Data of Alexa Fluor 488 and Alexa Fluor 555.
- (301) Oesterhelt, F.; Rief, M.; Gaub, H. E. Single Molecule Force Spectroscopy by AFM Indicates Helical Structure of Poly(Ethylene-Glycol) in Water. *New J. Phys.* **1999**, *1*, 6–6.
- (302) Feindt, M.; Kerzel, U. Statistische Grundlagen. In *Prognosen bewerten*; Springer Berlin Heidelberg: Berlin, Heidelberg, 2015; pp 7–26.
- (303) Toh, W.; Ng, T. Y.; Hu, J.; Liu, Z. Mechanics of Inhomogeneous Large Deformation of Photo-Thermal Sensitive Hydrogels. *Int. J. Solids Struct.* **2014**, *51* (25-26), 4440–4451.
- (304) Hong, W.; Zhao, X.; Zhou, J.; Suo, Z. A Theory of Coupled Diffusion and Large Deformation in Polymeric Gels. *J. Mech. Phys. Solids* **2008**, *56* (5), 1779–1793.
- (305) Gaiduk, A.; Kühnemuth, R.; Antonik, M.; Seidel, C. A. M. Optical Characteristics of Atomic Force Microscopy Tips for Single-Molecule Fluorescence Applications. *ChemPhysChem* **2005**, *6* (5), 976–983.
- (306) Seuss, M.; Fery, A. AFM Force Curve Analyzer for IgorPRO **2018**. DOI: 10.5281/zenodo.1208549
- (307) Campàs, O.; Mammoto, T.; Hasso, S.; Sperling, R. A.; O'Connell, D.; Bischof, A. G.; Maas, R.; Weitz, D. A.; Mahadevan, L.; Ingber, D. E. Quantifying Cell-Generated Mechanical Forces Within Living Embryonic Tissues. *Nat Methods* **2014**, *11* (2), 183–189.
- (308) Mohagheghian, E.; Luo, J.; Chen, J.; Chaudhary, G.; Chen, J.; Sun, J.; Ewoldt, R. H.; Wang, N. Quantifying Compressive Forces Between Living Cell Layers and Within Tissues Using Elastic Round Microgels. *Nat. Commun.* **2018**, 1–14.
- (309) Jungst, T.; Smolan, W.; Schacht, K.; Scheibel, T.; Groll, J. Strategies and Molecular Design Criteria for 3D Printable Hydrogels. *Chem. Rev.* **2016**, *116* (3), 1496–1539.
- (310) Blaeser, A.; Duarte Campos, D. F.; Puster, U.; Richtering, W.; Stevens, M. M.; Fischer, H. Controlling Shear Stress in 3D Bioprinting Is a Key Factor to Balance Printing Resolution and Stem Cell Integrity. *Adv. Healthcare Mater.* **2016**, *5* (3), 326–333.
- (311) Lin, Y.-Y.; Chen, H.-Y. Effect of Large Deformation and Material Nonlinearity on the JKR (Johnson–Kendall–Roberts) Test of Soft Elastic Materials. *J. Polym. Sci. B Polym. Phys.* **2006**, *44* (19), 2912–2922.
- (312) Pan, Y.; Zhan, Y.; Ji, H.; Niu, X.; Zhong, Z. Can Hyperelastic Material Parameters Be Uniquely Determined From Indentation Experiments? *RSC Adv.* **2016**, *6* (85), 81958–81964.
- (313) Valero, C.; Navarro, B.; Navajas, D.; García-Aznar, J. M. Finite Element Simulation for the Mechanical Characterization of Soft Biological Materials by Atomic Force Microscopy. *Journal of the Mechanical Behavior of Biomedical Materials* **2016**, *62*, 222–235.
- (314) Traeber, N.; Uhlmann, K.; Girardo, S.; Kesavan, G.; Wagner, K.; Friedrichs, J.; Goswami, R.; Bai, K.; Brand, M.; Werner, C.; et al. Polyacrylamide Bead Sensors for in vivo Quantification of Cell-Scale Stress in Zebrafish Development. *bioRxiv* **2018**, 420844.
- (315) Böhl, M.; Möhle, R. B.; Haesner, M.; Neu, T. R.; Horn, H.; Krull, R. 3D Finite Element Model of Biofilm Detachment Using Real Biofilm Structures From CLSM Data. *Biotechnol. Bioeng.* **2009**, *103* (1), 177–186.
- (316) Wenzl, J.; Seto, R.; Roth, M.; Butt, H.-J.; Auernhammer, G. K. Measurement of Rotation of Individual Spherical Particles in Cohesive Granulates. *Granular Matter* **2012**, *15* (4), 391–400.

---

# Danksagung

Zuallererst danke ich meinem Doktorvater Prof. Dr. Andreas Fery. Als Doktorand fühlt man sich wie ein Zwerg auf den Schultern eines Riesen, wie in dem eingangs zitierten Gleichnis. Anfangs scheint man vielleicht sogar ein wenig überfordert von den ungeahnten, neuen Perspektiven, die sich ergeben. Doch mit der Zeit lernt man von den Sichtweisen des Riesen und entdeckt mit ihm neue Horizonte. Andreas, darum Danke für Deine großartige Unterstützung, für das Entdecken neuer Sichtweisen und für das Teilhabenlassen an Deiner Weitsicht!

Eine Promotion hat viele Parallelen zu *Bohemian Rhapsody* – kunterbunt geht es zu, mal schnell, mal langsam, mal laut, mal leise, mal passiert vieles gleichzeitig, mal fokussiert sich alles auf eines. So durfte ich während meiner Promotion an vielen Schauplätzen mitspielen und danke allen, die mich begleitet haben:

Danke an den Lehrstuhl PCII an der Universität Bayreuth – ich denke immer gerne an die Zeit zurück! Danke an die AG Fery und die AG König – ich habe unseren Teamspirit sehr genossen! Danke an das Leibniz-Institut für Polymerforschung, insbesondere an das Team H118 und die gesamte Abteilung PG – Ihr habt mir den Anfang in Dresden leichter gemacht! Danke an Dr. Julian Thiele mit seiner Arbeitsgruppe – ich hatte nie das Gefühl, dass ich eigentlich nur Gast bei Euch war! Danke an Dr. Rico Tabor und sein SMaC-Lab – ich hatte einen interessanten und unglaublich kurzweiligen Forschungsaufenthalt bei Euch! Danke an alle meine Bürokollegen – es waren einige (ich hatte sechs verschiedene Schreibtische in der Zeit)!

Weiterhin danke ich dem Leibniz-Institut für Polymerforschung Dresden e.V., dem DFG SPP1420, dem DAAD im Rahmen des Bayreuth/Melbourne Colloid/Polymer Network und dem Elitenetzwerk Bayern für finanzielle und ideelle Unterstützung.

Ein weiterer besonderer Dank geht an Dr. Christian Kuttner und Dr. Johann Erath für spannende Diskussionen zu wissenschaftlichen Themen und Zerstreuung bei anderen Themen, sowie an die „Dresdner Force-keteers“ Maximilian Seuß und Inga Melnyk als meine engsten Mitstreiter im (Labor-)Alltag und für das Korrekturlesen dieser Arbeit.

*Last but not least*, herzlichsten Dank meiner Familie für Eure Unterstützung, besonders meiner Vanessa!





# Versicherung und Erklärung

Hiermit versichere ich, dass ich die vorliegende Arbeit ohne unzulässige Hilfe Dritter und ohne Benutzung anderer als der angegebenen Hilfsmittel angefertigt habe; die aus fremden Quellen direkt oder indirekt übernommenen Gedanken sind als solche kenntlich gemacht. Die Arbeit wurde bisher weder im Inland noch im Ausland in gleicher oder ähnlicher Form einer anderen Prüfungsbehörde vorgelegt.

Die vorliegende Arbeit wurde von Oktober 2014 bis Februar 2020 unter wissenschaftlicher Betreuung von Prof. Dr. Andreas Fery angefertigt; die experimentellen Arbeiten hierzu wurden von Oktober 2014 bis August 2015 an der Universität Bayreuth und von September 2015 bis August 2018 am Leibniz-Institut für Polymerforschung Dresden e.V. durchgeführt.

Februar 2020, Jens W. Neubauer